AUTOMATED MICROFLUIDIC PLATFORM WITH SYRINGE PUMPS

by

İsmail Terkeşli

B.S., Electrical and Electronics Engineering, Boğaziçi University, 2010

M.S., Electrical and Electronics Engineering, Boğaziçi University, 2013

Submitted to the Institute for Graduate Studies in
Science and Engineering in partial fulfillment of
the requirements for the degree of
Doctor of Philosophy

Graduate Program in Electrical and Electronics Engineering

Boğaziçi University

2024

ACKNOWLEDGEMENTS

First and foremost, I want to express my deepest appreciation to my thesis supervisor, Şenol Mutlu, for his unwavering guidance, mentorship, and invaluable insights throughout this journey. Your support has been instrumental in shaping the course of my research.

I would like to express my deepest gratitude to Faik Başkaya and Amitav Sanyal for their invaluable guidance, support, and expertise throughout my thesis progress. Furthermore, I am grateful to my labmates, Baha Erim Uzunoğlu, Mustafa Büke, and Ahmet Burak Yiğit, for their support and contributions to my research.

I express my heartfelt gratitude to my colleagues, including Canberk Demircan, Selçuk Yavuz, Timur Altınsoy, and the entire Smart Sensors team at Eliar Elektronik. Their collective efforts and the collaborative atmosphere within our team have been instrumental in generating innovative ideas and advancing our work. Special thanks to Mehmet Taygun and Eliar Elektronik for their belief and support in the academic-industry partnership, which has been a cornerstone of our success.

To my beloved family, I owe a debt of gratitude. To my mother, father, and sisters Dilara and Esra, your unwavering support, encouragement, and belief in me have been a constant source of motivation.

My heartfelt thanks go to my wife, Müge, and my son, Ali Batu, for their patience, understanding, and continuous support throughout the ups and downs of this academic journey.

This thesis would not have been possible without the collective support and encouragement of all those mentioned above.

ABSTRACT

AUTOMATED MICROFLUIDIC PLATFORM WITH SYRINGE PUMPS

This dissertation introduces a novel approach in differential colorimetric pH measurement by integrating microfluidic technology within an automated platform. This innovation signifies a considerable advancement for continuous liquid analysis of industrial applications. A novel sample injection method with precision syringe pump, is proposed to guarantee consistent flow rates and precise mixing ratios that is critical for the system's overall functionality.

A crucial part of this research involves the design, construction, and evaluation of a passive micromixer. This phase of the study is enhanced by the confirmation of 3D Computational Fluid Dynamics (CFD) simulations. Following this, the development and arrangement of a specialized optical sensing system enables the customization of the automated microfluidic system for specific use in pH analysis.

To analyze, improve, and validate the dynamic performance of the overall system, the research employs an electrical circuit analogy. This analogy is thoroughly explored through both SPICE simulations and experimental trials. The outcomes of these investigations confirm the system's ability to maintain fluctuation-free flow, leading to accurate and reliable pH measurements.

ÖZET

ŞIRINGA POMPALI OTOMATİK MİKROAKIŞKAN PLATFORMU

Bu tez, otomatik kontrol edilen bir platform içine mikroakışkan teknolojisini entegre ederek diferansiyel kolorimetrik pH ölçümünde yenilikçi bir yaklaşım sunmaktadır. Bu yenilik, endüstriyel uygulamalardaki sürekli sıvı analizi için önemli bir ilerleme anlamına gelmektedir. Sistemin genel işlevselliği için hayati önem taşıyan tutarlı akış hızları ve kesin karışım oranlarını garanti eden, şırınga pompasına dayalı yeni bir enjeksiyon yöntemi önerilmektedir.

Bu araştırmanın temel bir bileşeni, pasif bir mikserin tasarımı, üretimi ve karakterizasyonudur. Çalışmanın bu aşaması, 3B Hesaplamalı Akışkanlar Dinamiği (CFD) simülasyonlarının doğrulanması ile güçlendirilmiştir. Otomatik mikroakışkan sisteminin pH analizi yapabilmesi için özel bir optik algılama sistemi de entegre edilmiştir.

Sistemin dinamik performansını analiz etmek, geliştirmek ve doğrulamak için elektrik devre analojisinden yararlanılmıştır. Bu analoji, hem SPICE simülasyonları hem de deneyler aracılığıyla kapsamlı bir şekilde karşılaştırılmış ve doğrulanmıştır. Bu incelemelerin sonucunda, dalgalanma içermeyen bir sıvı akışı oluşturulmuş ve güvenilir ve tekrarlanabilir pH ölçümleri yapılmıştır.

TABLE OF CONTENTS

ACKNOWLEDGEMENTS . . . iii
ABSTRACT . . . iv
ÖZET . . . v
LIST OF FIGURES . . . viii
LIST OF TABLES . . . xiv
LIST OF SYMBOLS . . . xv
LIST OF ACRONYMS/ABBREVIATIONS . . . xvii
1. INTRODUCTION . . . 1
2. AUTOMATED MICROFLUIDIC PLATFORM . . . 10
2.1. Injection Methods on Microfluidic Systems . . . 10
2.2. Syringe Pumps . . . 11
2.2.1. Design and Fabrication . . . 11
2.2.2. Control and Characterization . . . 13
2.3. Fabrication Methods of Microfluidic Chips . . . 18
2.3.1. Laser Ablation . . . 19
2.3.2. Micro-milling . . . 21
3. DROPLET MICROFLUIDICS . . . 24
3.1. Overview of Droplet Microfluidics . . . 24
3.2. Experiments with Commercially Available Microfluidic Chip . . . 25
3.2.1. Droplet Generation . . . 29
3.2.2. Droplet Manipulation . . . 31
3.3. Experiments with In-house Fabricated Microfluidic Chip . . . 34
3.4. Discussion . . . 37
4. ANALYSIS AND OPTIMIZATION USING ELECTRICAL ANALOGY . . . 39
4.1. Novel Sample Injection Method . . . 39
4.2. Verification Using Y-channel Microfluidic Chip . . . 43
4.3. Electric Circuit Analogy . . . 45
4.3.1. Electrical Analogue . . . 45

4.3.2. Spice Simulations and Verification 49
4.3.3. Improvement of Injection Setup 53
5. DIFFERENTIAL COLORIMETRIC pH MEASUREMENT 55
5.1. Proposed Setup 55
5.2. Theoretical Background 56
5.3. Experimental Methodology 60
5.4. Preliminary Off-chip Experiments 63
5.5. Development and Validation of the Microfluidic Mixer 67
5.5.1. Design and Simulation 67
5.5.2. Experimental Verification 73
5.6. pH Measurement of Transparent Liquids 74
5.6.1. Phenol Red 75
5.6.2. Universal Indicator 77
5.7. Fabrication of the Automated Platform 78
5.7.1. Optical Sensing Setup 78
5.7.2. Revision of Syringe Pump Design for Push-Pull Operation . . . 79
5.7.3. Modification of Microfluidic Mixer Chip 80
5.7.4. Optical Analysis of Mixer Performance 80
5.8. pH Measurement of Colored Liquids 84
6. CONCLUSION AND FUTURE WORK 87
6.1. Future Work 88
REFERENCES 89
APPENDIX A: PERMISSIONS 105
A.1. Papers 105

LIST OF FIGURES

Figure 2.1. Mechanical design of syringe pump operating bidirectionally. . . . 13

Figure 2.2. Syringe pumps produced in laboratory with (a) PMMA bottom plate (b) aluminum bottom plate. 14

Figure 2.3. Schematic diagram of automated platform. 15

Figure 2.4. Fabricated syringe pumps. 16

Figure 2.5. Graphical user interface to control and operate syringe pumps. . . 17

Figure 2.6. The flow diagram of microfluidic chip fabrication process by laser-ablation and micro-milling. 21

Figure 2.7. Micromachining process during fabrication of the microchannels. . 22

Figure 2.8. Different sections of microfluidic chip fabricated by micro-milling. 23

Figure 3.1. Passive droplet generation methods of (a) co-flowing, (b) cross-flowing in T-shaped junction, (c) flow-focusing [89]. 26

Figure 3.2. The layout of the microfluidic chip used for droplet production. . . 27

Figure 3.3. The connections for microfluidic chip. 28

Figure 3.4. The experimental setup for droplet generation and manipulation. . 28

Figure 3.5. (a) Laminar flow (b) droplet generation. 30

Figure 3.6. Different coloured droplets. 32

Figure 3.7. The array of droplets with different concentrations of dyes. 33

Figure 3.8. The diameter size of droplets for water fraction of 0.35, 0.45 and 0.55, respectively. 33

Figure 3.9. The chip designs to generate droplets with (a) flow-focusing method, (b) T-junction method. 34

Figure 3.10. Microfluidic channels zoomed to show flow and generated droplets. 35

Figure 3.11. The microscope image showing oil droplets with different coloured background in flow-focusing method. 36

Figure 3.12. The microscope image showing oil droplets with different coloured background in T-junction method. 37

Figure 4.1. Two common methods to introduce liquids with desired volumetric ratios for mixing (a) with closed-loop feedback (b) single syringe pump withdrawing liquids from the outlet port. 40

Figure 4.2. Examples of push-pull syringe systems (a) with single syringe pump [63] (b) with two syringe pumps [64]. 41

Figure 4.3. Proposed injection method with a single syringe pump. 42

Figure 4.4. Captured images of blue and red dyed liquids inside a microfluidic channel while different sizes of pulling syringes are connected with diameters of (a) 12.4, (b) 15.5 (c) 18.5 and, (d) 28.8 mm. 44

Figure 4.5. The measurement results of the width ratios of the experiment agree with the cross-sectional area ratios of the syringes. 44

Figure 4.6. Electrical circuit representation of the experimental setup. 49

Figure 4.7. Flow oscillations at inlet boundary with low flow rate of 15 µL/min without damping effect of syringe. 51

Figure 4.8. Large fluctuations at the inlet boundary with (a) image capture and (b) simulated results using 4-cm long inlet and 20-cm long outlet tubing. 52

Figure 4.9. Smaller fluctuations at the inlet boundary with (a) image capture and (b) simulated results using both 20-cm long inlet and outlet tubing. 53

Figure 4.10. Integration of a gearbox with a 100:1 ratio. 54

Figure 4.11. Fluctuation-free flow at the inlet boundary with after integrating gearbox (a) image capture and (b) simulated results using both 20-cm long inlet and outlet tubing. 54

Figure 5.1. Schematic for differential colorimetric pH measurement setup. . . 55

Figure 5.2. Typical spectral response of a pH indicator under pH environments of acidic, intermediate, and basic. 57

Figure 5.3. Electronic boards designed and used in data acquisition. 62

Figure 5.4. Graphical user interface designed for observing actual data. 63

Figure 5.5. Samples prepared at varying mixing ratios, ranging from 1:10 to 5:10 (indicator to overall volume), within a pH range of 6 to 8. . . 64

Figure 5.6. Spectral response of buffer solutions with phenol red at a 40:1 mixing ratio for pH 6 and pH 8, conducted in 10 mm cuvettes. 65

Figure 5.7. Absorbance measurements of buffer solutions at 560 nm with phenol red at a 40:1 mixing ratio for pH 6 and pH 8, conducted in 10 mm cuvettes. 65

Figure 5.8. Design of the microfluidic chip featuring a micro-mixer with numbered passages and elbows, alongside the cutlines indicated for simulation purposes. 69

Figure 5.9. Concentration distribution in microfluidic mixer at Cutline 1, illustrating the effects of varying channel depth for inlet flow rate of 1 mL/h. 70

Figure 5.10. Concentration distribution in microfluidic mixer at Cutline 2, illustrating the effects of varying channel depth for inlet flow rate of 1 mL/h. 70

Figure 5.11. Concentration map inside the microfluidic mixer for the inlet flow rate of 1 mL/h. 71

Figure 5.12. Concentration map inside the microfluidic mixer for the inlet flow rate of 20 mL/h. 71

Figure 5.13. Concentration distribution in microfluidic mixer at Cutline 1 that illustrates the effects of varying inlet flow rates at 1 mL/h and 20 mL/h. 72

Figure 5.14. Concentration distribution in microfluidic mixer at Cutline 2, illustrating complete mixing despite varying inlet flow rates at 1 mL/h and 20 mL/h. 73

Figure 5.15. Mixing efficiency for varying inlet flow rates. 74

Figure 5.16. Optical pH measurement using a microfluidic channel with a modified syringe pump (a) whole experimental setup (b) microfluidic chip. 75

Figure 5.17. Absorbance measurements of the phenol red pH indicator between pH 6 and pH 8 in steps of 0.25. 76

Figure 5.18. Logarithm of the absorbance ratios at wavelengths of 550 and 450 nm versus input pH values. 76

Figure 5.19. Experimental results of the optical pH measurement with universal indicator consisting of thymol blue, methyl red, bromothymol blue and phenolphthalein. 77

Figure 5.20. Exploded view of optical measurement setup in detail. 78

Figure 5.21. White LEDs coupled across the observation windows of the chip. . 79

Figure 5.22. Custom-designed syringe pump and syringe assembly. 79

Figure 5.23. The microfluidic chip fabricated for optical pH measurements in colored liquids. 80

Figure 5.24. Concentration map inside the microfluidic mixer for the inlet flow rate of 1 mL/h. 81

Figure 5.25. Experimental setup for differential colorimetric pH measurement using a microfluidic channel. 81

Figure 5.26. Optical sensors aligned with the chip's measurement windows. . . 82

Figure 5.27. Evaluation of mixing efficiency using (a) captured image (b) absorbance readings of red dye solution and its mixture with DI water at 450 nm. 83

Figure 5.28. Evaluation of differential colorimetric method for pH measurement using (a) captured image (b) ratio of absorbance values at 450 nm and 550 nm. 85

Figure 5.29. Compensated absorbance ratio for three different blue dye concentrations. 86

Figure A.1. Permission letter [63]. 105

Figure A.2. Permission letter [64]. 106

Figure A.3. Permission letter [89]. 107

LIST OF TABLES

Table 2.1. Syringe pump displacement for duration of 600 seconds in varying speeds. 17

Table 4.1. The physical analogy between microfluidics and electronics. 46

Table 4.2. Equivalent circuit parameters used in electrical simulations. 50

Table 5.1. Off-chip optical pH measurement of colored liquids for various food dyes. 66

LIST OF SYMBOLS

A	Absorbance
A_i	Absorbance of each solute in the mixed solution
A_i^0	Initial absorbance of each solute before mixing
A_{ind}	Cross-sectional area of indicator syringe
A_{mix}	Cross-sectional area of mixed output syringe
C	Capacitance
C_{chip}	Hydrodynamic capacitance of microfluidic chip
C_{inlet1}	Hydrodynamic capacitance of indicator inlet tubing
C_{inlet2}	Hydrodynamic capacitance of sample inlet tubing
C_{outlet}	Hydrodynamic capacitance of outlet tubing
C_{pump1}	Hydrodynamic capacitance of pushing syringe
C_{pump2}	Hydrodynamic capacitance of pulling syringe
C_c	Hydrodynamic capacitance of cylindrical tubing
C_h	Hydrodynamic capacitance
C_t	Hydrodynamic capacitance of rectangular microchannel
Ca	Capillary number
E	Young's modulus
I	Electrical current
I_0	Incident intensity
I_t	Transmitted intensity
K_a	Acid dissociation constant
L	Channel length
M	Moles per liter
P	Pressure
P_{s}	Sample pressure
Q	Volumetric flow rate
Q_{ind}	Indicator flow rate
Q_{mix}	Mixed output flow rate

Q_{s}	Sample flow rate
R	Resistance
R_{chip}	Hydrodynamic resistance of microfluidic chip
R_{inlet1}	Hydrodynamic resistance of indicator inlet tubing
R_{inlet2}	Hydrodynamic resistance of sample inlet tubing
R_{outlet}	Hydrodynamic resistance of outlet tubing
R_{pump1}	Hydrodynamic resistance of pushing syringe
R_{pump2}	Hydrodynamic resistance of pulling syringe
R_c	Hydrodynamic resistance of rectangular microchannel
R_h	Hydrodynamic resistance
R_t	Hydrodynamic resistance of cylindrical tubing
Re	Reynolds number
X	Distance traversed
a_H	Activity of hydrogen
b	Path length
h	Channel height
r_i	Internal radius
r_o	Outer radius
w	Channel width
α	Mixing ratio
α_i	Mixing ratio of each solute
λ	Wavelength
λ_1	Wavelength of maximum absorbance of acidic form
λ_2	Wavelength of maximum absorbance of basic form
ν	Poisson's ratio
ε	Molar absorptivity
ε_{HIn}	Molar absorptivity of acidic form
ε_{In^-}	Molar absorptivity of basic form
η	Dynamic viscosity

LIST OF ACRONYMS/ABBREVIATIONS

2D	Two-Dimensional
3D	Three-Dimensional
CAD	Computer-Aided Design
CAM	Computer-Aided Manufacturing
CCT	Color Correlation Temperature
CFD	Computational Fluid Dynamics
CNC	Computer Numerical Control
COP	Cyclo-Olefin Polymer
CRI	Color Rendering Index
DEP	Dielectrophoresis
DI	Deionized
DNA	Deoxyribonucleic Acid
EWOD	Electrowetting on Dielectric
FDM	Fused Deposition Modeling
FET	Field-Effect Transistor
GUI	Graphical User Interface
ISFET	Ion-Sensitive Field-Effect Transistor
KCL	Kirchhoff's Current Law
KVL	Kirchhoff's Voltage Law
LCD	Liquid Crystal Display
LED	Light Emitting Diode
LOC	Lab-on-Chip
PCB	Printed Circuit Board
PDMS	Polydimethylsiloxane
PEEK	Polyetheretherketone
PMMA	Polymethyl Methacrylate
POC	Point-of-care
PS	Polystyrene

PWM	Pulse Width Modulation
RTOS	Real-Time Operating System
SLA	Stereo Lithography
SPI	Serial Peripheral Interface
SPICE	Simulation Program with Integrated Circuit Emphasis
TFT	Thin-Film Transistor
UART	Universal Asynchronous Receiver-Transmitter
UV	Ultraviolet

1. INTRODUCTION

Microfluidic systems, renowned for their ability to transport, mix, and characterize raw samples using a single device, have become increasingly prominent in various scientific and medical fields [1]. These systems are very important in clinical biology, chemistry, genetic analysis, capillary electrophoresis, DNA amplification, proteomics, cellular analysis, point-of-care diagnostics, drug discovery, and in the synthesis of molecules and materials [2]. Their growing popularity can be attributed to their advantages of low cost, rapid analysis, compact size, and the ability to precisely control liquid handling and biochemical reactions and analysis [3]. Poly(dimethylsiloxane) (PDMS) and soft lithography-based microfluidics are now commonly used in many laboratories for exploratory research because it is low-cost, easy to use and can form integrated pneumatic valves. Microfluidic chips made out of thermoplastics such as poly(methyl methacrylate) (PMMA), polystyrene (PS) and cyclo-olefin polymer (COP) were investigated for commercial deployment exploiting their mass production capabilities [4–6]. Glass microfluidic chips were also studied due to their better chemical and temperature resistances [7]. However, with such advantageous features of microfluidic systems and three decades of intensive research, microfluidic products have still limited usage in clinical laboratories or industry, which are mainly dominated by bench-top analytical instrumentation.

Lab-on-a-chip devices, including blood analysis and point-of-care (POC) devices, droplet dispensers for chemistry and biology, and inkjet dispenser heads represent commercially available products in the field of microfluidics [8, 9]. The healthcare and life sciences sectors are primary markets for these microfluidic systems. However, there is also huge potential in areas like industrial instrumentation, environmental monitoring, and the fields of chemical analysis and synthesis [10]. The integration potential of microfluidic devices highlight their importance across many scientific and industrial domains.

The textile industry, especially the dyeing sector, exerts a considerable environmental footprint due to its extensive wet processing techniques. So, it is urgently needed to decrease the consumption of power, chemicals, and water [11, 12]. Many studies have concentrated on improving both dyes and dyeing machinery to optimize the dyeing process while minimizing its environmental impact [13, 14]. Despite these improvements, the textile dyeing industry continues to face challenges such as lack of batch-to-batch repeatability and unoptimized amounts of water and chemicals [15]. Achieving 'right first time' dyeing success is significantly dependent on the compatibility between different dye classes from various manufacturers, as well as the compatibility between dyes and auxiliary chemicals [16]. Conventionally, the preparation of dye baths for testing various recipes on a laboratory scale is carried out either manually by laboratory personnel or using large, automated pipetting machines. These methods typically have the disadvantages of limited sample preparation capabilities or complex procedures like mixing, stirring, and rinsing, respectively.

The introduction of microfluidic technology presents a promising solution for improving dye bath recipe development. This technology enables efficient parallel analysis. So, it may significantly reduce the amount of materials used. It also offers the capability to experiment with a variety of dye types and concentration combinations. In addition, microfluidic systems can provide more precise control and measurement of critical parameters like pH and conductivity, which are very important in successful dyeing results. The integration of microfluidics could lead to more sustainable practices in the textile dyeing industry by enhancing efficiency and minimizing waste.

Monitoring pH is another critical parameter of textile dyeing processes. Wool as a protein-based fiber is notably sensitive to changes in pH levels. The ideal pH range for dyeing wool with acid dyes is slightly acidic. It is between 4.5 and 5.5 for milling acid dyes and 5.5 and 6.5 for neutral-dyeing acid dyes. Acidity levels outside of this range can lead to heavy quality issues. For instance, more acidic dye bath (with a very low pH) can weaken the wool fibers, resulting to diminished strength or poor texture. On the other hand, an excessively alkaline environment (high pH) can cause

uneven dyeing, marked by poor color absorption and reduced color fastness [17, 18]. Additionally, the stability and efficacy of the dyes themselves are largely dependent on keeping an optimal pH value. Some dyes deteriorate or change color if the pH goes outside their stable range.

Traditionally, pH monitoring in textile dyeing was carried out with test strips by halting the process at predetermined stages. While these strips are easy to use, they have very limited precision. With the advent of automation and increasing awareness of its benefits, more sophisticated instrumentation is being integrated into the machines for continuous monitoring of the pH. Glass pH electrodes offer greater accuracy but come with problems. They need for regular calibration resulting to high reagent consumption. They have inherently shorter lifetime. This evolution from basic test strips to advanced instrumentation underscores the ongoing needs for more dependable and efficient pH monitoring methods in industries where precise pH control is vital to maintaining product quality and color consistency.

The challenges and limitations in automating dye recipe optimization and current pH measurement techniques have the high potential for significant improvements utilizing the microfluidic systems. These advancements may transform industry practices by real-time monitoring of process parameters and reduced maintenance resulting in optimizing the quality of dyeing processes in industries like textile dyeing.

Industrial usage is not only limited to the textile industry. The measurement of pH, a critical indicator of acidity or alkalinity, is important for various scientific and industrial applications. In broader industrial processes, particularly in chemical manufacturing and water treatment, pH control is essential for operational efficiency and the quality of the products [19–21]. In chemistry and biology, pH control is essential for driving bacterial interactions and the functionality of molecules like enzymes, impacting cellular and systemic health [22]. In environmental science, pH levels are monitored to follow ecosystem health since the deviations can signal pollution. Agriculture benefits from pH monitoring, as soil acidity or alkalinity significantly influences

carbon cycling processes, phosphorus availability, and plant health [23, 24]. The food industry uses pH to control flavor, texture, preservation, and fermentation processes, ensuring product quality and safety [25].

The pH value is one of the most commonly measured parameters. It can be measured using electrochemical and optical techniques. Between them, electrochemical pH measurement is the most widely used technique. It is done by a potentiometric transmitter and a glass membrane electrode. These electrodes generate a potential difference between a working and a reference electrode in response to the hydrogen ion activity in the solution. Then, the pH meter measures this potential and converts it into a pH value. This method is highly accurate, reliable, cost-effective. It is suitable for a wide range of applications, from laboratory research to industrial processes. They have wide pH operating range and relatively quick response time. However, the glass pH electrode's bulkiness, fragility, and susceptibility to electromagnetic interference are the main disadvantages.

In addition to glass membrane electrodes, other electrochemical methods for pH measurement include metal/metal oxide electrodes, liquid membrane electrodes, and hydrogen-sensitive pH field-effect transistors based on ion-selective field-effect transistors (ISFETs) [26]. In sectors like the food and beverage industry, where fragility is a major concern, there is a shift towards using ion-sensitive field effect transistors [27]. These transistors operate on the principle of electric field alteration within the conduction channel, triggered by hydrogen ions [28, 29]. Each of these methods have their own benefits in terms of sensitivity, selectivity, and application suitability.

Optical methods are especially useful in where electrochemical methods are not operatable, such as in environments with high ionic strength or where the presence of an electrode is undesirable or feasible. They emerged as another possible alternative due to the advantages of using color-changing reagents responsive to pH changes. The main optical characteristics evaluated are absorption, fluorescence intensity, and decay time, while additional parameters like reflectance, refractive index and light scattering

are also employed for analysis [30]. The evolution of these techniques has led to the development of optical pH sensors that are non-invasive and well-suited for microfluidic systems where conventional electrochemical sensors might be impractical. These are the applications requiring continuous, real-time pH monitoring, such as in sensitive biochemical assays and medical diagnostics, where only minimal sample and reagent volumes are available.

Measurements obtained from optical sensors and standard industrial electrochemical probes are closely parallel. It has been shown that they align within 0.05 pH units 60% of the time and within 0.1 pH units 99% of the time [31]. Although the problems related to varying ionic strength and temperature may limit accuracy to approximately ± 0.05 pH units, these sensors are sufficient for various applications [32].

One of the oldest ways of measuring pH value of liquids is to use pH indicators. These indicators are low-cost small molecules that can be mass produced easily, e.g., red cabbage or most of the plants in nature [33,34]. Absorptiometry and reflectometry, along with luminescence-based methods, are widely utilized for optical pH measurement. These techniques typically rely on light absorption at specific wavelengths or the fluorescence of certain molecular structures. However, absorption and reflection-based methods have the drawback of being affected by ambient and background light [32]. Additionally, absorption-based sensors require optical transparency in the setup to allow light passage. In contrast, fluorescence-based pH indicators offer higher sensitivity and require significantly lower concentrations of the indicator. Despite these advantages, fluorescent pH indicators often have limited response ranges and may exhibit low solubility in aqueous solutions restricting their application scope [35]. Optical pH measurement methods that leverage changes in refractive index and surface plasmon resonance, utilizing swellable materials, have also been demonstrated [36–38]. Recent advancements in nanotechnology have led to the exploration of various nanomaterials like silica nanoparticles, semiconductor quantum dots, carbon materials, and polymer nanoparticles. They are grouped into those modified with pH-sensitive fluorescent dyes and those with pH-responsive morphological features [39–41].

Optical pH measurement detection generally include the use of conventional spectrophotometers, photodetectors, infrared and Raman spectroscopy, and image processing techniques [42–46]. Continuous pH measurement using commonly used paper-based pH indicators, where small molecules are immobilized inside paper fabric, is not versatile since it requires either manual manipulations or robotic motions. Also, they have low accuracy, generally limited to ± 1 pH units. Spectrophotometric, precise, and accurate seawater pH measurements inside a flow cell over an extended period were achieved through automated instruments utilizing multiple pumps and valves, demonstrating consistency with reference pH sensors and stability during a 59-day sea deployment [47]. Besides, smartphone cameras are used to estimate pH of commercially available pH strips inside the mini light box [48].

There are many recent studies in the field of microfluidics focusing on optical pH measurement [49–53]. The optical determination of sweat pH through colorimetric changes was presented, leveraging a pH-sensitive dye immobilized within the microfluidic cloth-based analytical devices [54]. An optical fiber sensor with fluorescent dye affixed to its end measures pH by detecting changes in fluorescence intensity, and its effectiveness was assessed directly within a microfluidic channel [55].

Recently, automated sampling and considerations for long-term operation have been successfully integrated into microfluidic systems by enhancing their functionality and application scope. One example is a thermoplastic microfluidic chip, equipped with syringe pumps, multiple valves, and the pH indicator thymol blue, enabling continuous colorimetric measurements of ocean water pH in oceanic studies with a precision of 0.001 pH and an accuracy within 0.004 pH units [56]. Similarly, a low-cost detection system employing a light-emitting diode as a light source and a photodiode as a detector, coupled with an autonomous reagent-based microfluidic pH sensor platform, demonstrated high reproducibility and stability over 8 months. By blending different pH-sensitive dyes and fine-tuning their proportions, the range for detecting pH was successfully broadened to encompass values from 4 to 9. [57]. Additionally, a cost-effective lab-on-a-chip device for marine pH quantification utilized a PDMS microfluidic system

and an integrated optical-electronic system with LEDs as light sources and photodiodes as detectors, achieving a resolution of 0.002 pH units for the seawater pH range of 7.500–8.200 [58]. A four-layer borosilicate glass chip, controlled by multiple syringe pumps, enabled maintenance-free continuous photometric pH measurements of swimming pools, including active and total chlorine concentrations, with only 60 μL reagent consumption per measurement over 3 months and favorable comparisons to commercial products [59].

Across these studies, it is observed that sensor performance may be compromised in samples that are not transparent, specifically those with distinct coloration and absorbance characteristics. Therefore, there is an urgent need for improving sensor technology to cover a wider range of samples. Additionally, the conventional use of commercially available pumps, at least two pumps, for sample injection and spectrophotometers for detection in optical pH sensing setups is not practical for various applications. Although these components are widely used, they are characterized by their bulkiness and high cost limiting their usage.

Most of the industrial and medical systems require continuous and automated sampling and analysis of liquids. Getting samples continuously from sources of liquids with unknown volume, pressure or flow rates is challenging. The sources can be diverse such as swimming pools, industrial processing tanks, water pipes, different water levels of lakes, seas or oceans, and bodily fluids. Sampling methods are also diverse. The liquids may be dropped on the inlet ports or drawn to syringes and then applied. The microfluidic chip can be embedded into a water tank or pipe. Automating the sample injection into the chip becomes very popular [60].

In most of the applications, samples must be introduced continuously, and they must be mixed at fixed rates independent of the pressure values of the samples. Generally, syringe pumps are used to inject samples and reagents. Syringe pumps are usually operated in an open-loop manner, where flow rates and mixing ratios are influenced by the characteristics of the pump, channel, and input pressure of the sample [61]. Even

the same type of syringe pumps from the same manufacturer can result in different flow characteristics on a microfluidic system [62]. The push-pull system involves simultaneous infusion and withdrawal of the same reagents using two syringes coupled to the same mechanical motion, ensuring pulse-free, highly accurate, and precise flow in bioreactor systems [63, 64].

To succeed a reliable and repeatable automated platform, it is prerequisite to thoroughly analyze the injection system, microfluidic chip, and their connections. This examination is critical to achieve stable and consistent flow rates while minimizing fluctuations.

This thesis study addresses existing difficulties in the adaptation of microfluidic technology and presents practical solutions and methods across various aspects of this field. By this mean, an automated microfluidic platform to control, manipulate, sense and measure fluids is constituted. The outline includes:

Chapter 2 details the design and fabrication of an injection system utilizing syringe pumps for an automated microfluidic platform. It is completed with mechanical and electrical control mechanisms. It also delves into microfluidic fabrication methods, particularly focusing on the development and application of laser ablation and micromilling techniques.

In Chapter 3, the study explores droplet microfluidics, specifically the generation and manipulation of droplets, by controlling the flow rate of three different dyes within commercially available chips and in-house fabricated chips.

Chapter 4, along with the introduction of a novel sampling injection method, presents an analysis of its electrical analogy for removing flow fluctuations and optimizing the setup. The detailed electrical analogy of the complete system, including the microfluidic chip, injection system, and tubing connections, is worked on to optimize performance and prevent any flow inconsistencies.

In Chapter 5, a novel sensor design is introduced, featuring automated sampling and simple injection to address the limitations of current methods. This design is based on absorption-based pH measurement. Utilizing a microfluidic chip with an integrated passive micromixer, it ensures effective mixing of the sample solution with a pH indicator. 3D Computational Flow Dynamics (CFD) simulations and experimental work are also included to verify the efficiency of the mixer. Finally, both pH measurement of transparent liquids and differential colorimetric pH measurement of colored liquid using a microfluidic chip is presented.

2. AUTOMATED MICROFLUIDIC PLATFORM

In this chapter, the components of an automated microfluidic platform are explored, including injection tools, control systems and microfluidic chips. The chapter starts by examining existing injection methods with a specific focus on design, fabrication and characterization of syringe pumps. Subsequently, the discussion shifts to various microfluidic chip fabrication techniques, notably fabrication steps of laser ablation and micro-milling in the creation of chips used in the thesis.

2.1. Injection Methods on Microfluidic Systems

Intense research on liquid pumping, flow control and mixing at fixed and stable ratios in microfluidic systems resulted in many passive and active pumping methods. In passive injection methods, fluids are manipulated without external actuators or power sources. They rely on phenomena such as capillary action, osmosis, surface tension, and gravity-driven flow [65]. They are mostly for single use applications and typically are not aimed for continuous months-long industrial operations.

A pumping system is generally necessary to achieve consistent and stable long-term fluid delivery in a microfluidic channel network [66]. Peristaltic pumps, which are positive displacement pumps operating at low pressure, find widespread use in both scientific and industrial applications. These pumps function by compressing a flexible tube using a set of rollers that travel along its length, thereby creating fluid flow [67]. These pumps have closed-loop operation and recirculation benefits. However, they exhibit significant flow pulsations. To minimize pulsations, three distinct peristaltic attenuators were compared and utilized [68]. However, these pumps are less favored in microfluidic applications today.

Two common methods for controlling microfluidic flow are flow control and pressure control. Pressure control involves pressurizing a sample container, allowing for

smooth injection into the microfluidic chip. This method offers benefits such as rapid equilibration, stable flow, and versatility in fluid dispensing. However, maintaining pressure balance is essential to prevent backflows, and it requires pressurized air. Pressure-driven systems deliver high performance, pulseless flows, and fast responses but can be costly and necessitate an external pressure source.

Flow control method bases on usage of syringe pumps. Syringe pumps are the most commonly used devices in microfluidic systems to generate constant flow rates. They may handle very small volumes down to nanoliters. They are composed of step motors, ball screws, and gears. They are low-cost and easy to use. However, syringe pumps are typically operated in open-loop which makes the flow rates and mixing ratios depend on pump's and channel's characteristics and the sample's input pressure. Even same type of syringe pumps from the same manufacturer can result in different flow characteristics on a microfluidic system [61].

Throughout the thesis study, syringe pumps were utilized as the injection tool. They are thoroughly examined for both mechanical rigidity and electrical characteristics. Their design, fabrication, and subsequent characterization are detailed in the following section.

2.2. Syringe Pumps

2.2.1. Design and Fabrication

Syringe pumps employ a stepper motor for precise linear motion, controlling piston speed to eject or draw in liquid. Their technical specifications depend on the specific application's accuracy and flow precision requirements. Syringe pumps are flexible by changing syringe diameter to adapt the working range. Motor step size may lead to oscillations at low flow rates. It can be prevented by using smaller syringe diameters. Elasticity and hydrodynamic resistance of components in microfluidic systems also influence flow stability.

Several factors influence the rate of liquid displacement in the microfluidic channel, including channel surface area, syringe and lead screw rod diameters, and the micro-step size of the motor. The threaded rod, crucial in transforming the motor's rotational movement into vertical motion, moves the plunger. With a typical stepper motor functioning at 200 steps per revolution and a 1/32 micro-stepping driver capability, for an 8 mm diameter lead screw rod, each step instruction corresponds to a 1.25 µm movement of the plunger. A smaller plunger displacement can be achieved using a screw rod with a smaller diameter although this reduces the applied torque. The syringe's inner cross-sectional area then dictates the volume displaced into the microfluidic channel, with a smaller syringe diameter resulting in less liquid being ejected per micro-step. Moreover, factors such as the material of the syringe, mechanical rigidity, and inadequate sealing also impact the consistency of the automated system. The material of the syringe is critical as the system's response is contingent upon the pressure the syringe can endure. Given that the syringe pump consists of various mechanically interconnected parts, ensuring mechanical rigidity is essential to guarantee that every movement of the stepper motor is effectively transferred to the plunger with sufficient torque.

The mechanical design of the syringe pump, adaptable to various syringe sizes, was developed using Autodesk Inventor 3D CAD software. As illustrated in Figure 2.1, the design shows fundamental components like ball bearings for radial loads, linear bearings, 8 mm chrome linear rods, and an 8 mm lead screw rod. NEMA 14 bipolar stepper motors with 200 steps/revolution and dimensions of 35×28 mm were selected for syringe pumps. They were coupled with threaded rods using couplers. They ensure smooth linear motion of the moving parts through the support of double linear bearings. To prevent any sliding of the syringes during operation, plunger flanges were placed both vertically and horizontally. Non-standard parts such as the support and moving bodies were custom fabricated using a MakerBot Replicator 3D printer. For the experiments, various volumes of PMMA syringes with Luer lock fittings, including but not limited to those from Kruuse brand, were utilized.

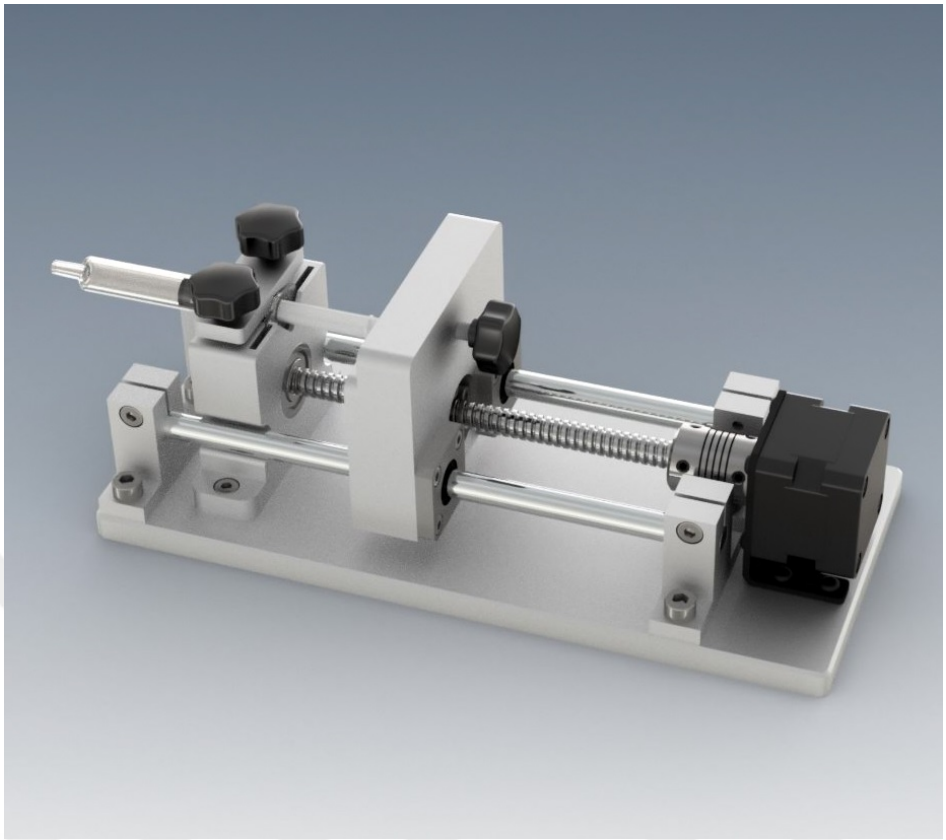

Figure 2.1. Mechanical design of syringe pump operating bidirectionally.

The completed and assembled syringe pump, featuring a bottom tray made from a PMMA bottom plate, is visible in Figure 2.2(a). Post-testing, it was determined that for enhanced accuracy and robustness, the connection holes should be drilled using a computer numerical control (CNC) router. Furthermore, to effectively dissipate the heat generated by the stepper motor across the bottom tray, an aluminum bottom plate, as shown in Figure 2.2(b), was employed. In a similar way, a total of four syringe pumps were produced and assembled.

2.2.2. Control and Characterization

The automated platform, assembled with syringe pumps produced in the laboratory, comprises an operating monitor for controlling software and four syringe pumps. The electronic schematic of this automated platform is comprehensively detailed in Figure 2.3.

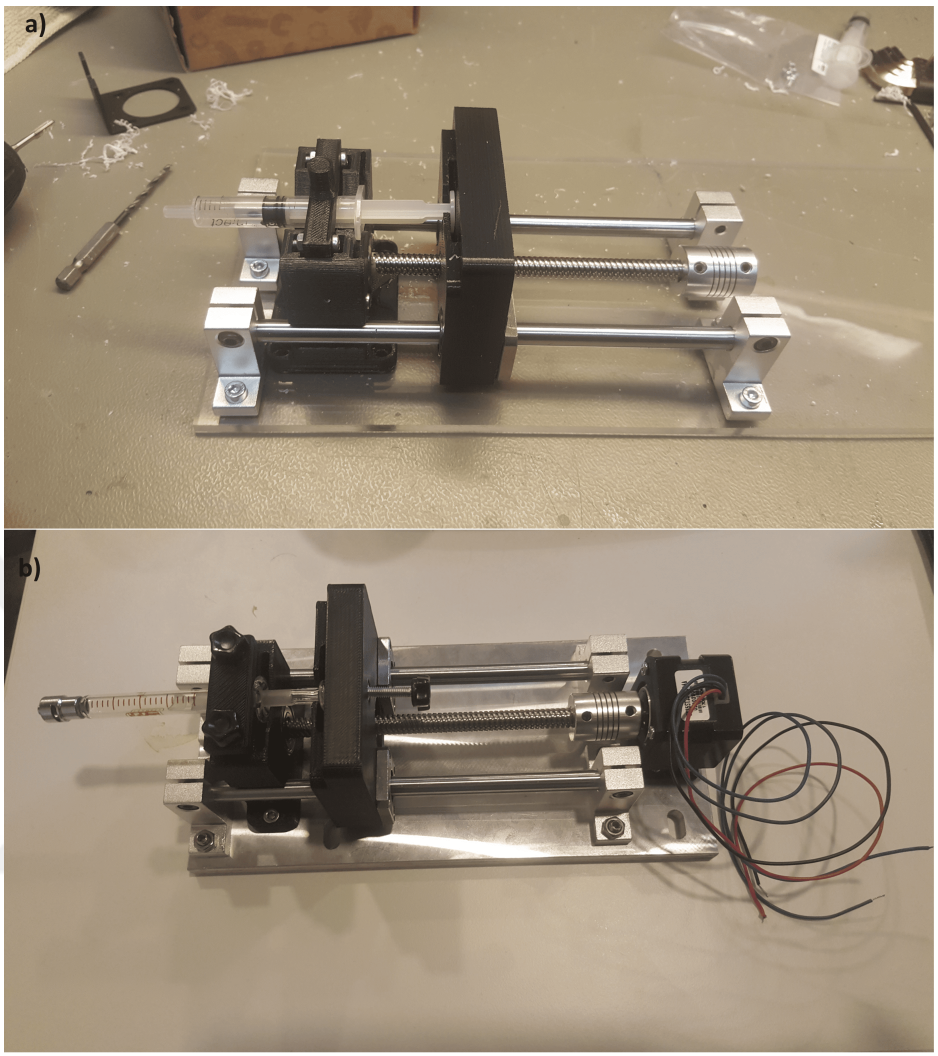

Figure 2.2. Syringe pumps produced in laboratory with (a) PMMA bottom plate (b) aluminum bottom plate.

For rapid prototyping purposes, a Raspberry Pi 3, an ARM-based computer running Linux, serves as the microprocessor. It regulates the pumping rates of the syringe pumps by controlling the stepper motor driver, as these pumps are equipped with stepper motors driven directly by this driver. The NEMA 14 bipolar stepper motors in the system operate at 10 V and 0.5 A per phase. The DRV8825 micro-stepping bipolar stepper motor driver, developed by Texas Instruments, incorporates features such as adjustable current limiting, high-resolution micro-step modes up to 1/32 of a step, and safeguards against over-current and over-temperature. The current control of the step motor is made adjustable through a potentiometer. For the NEMA

14 motors, which are rated at 0.5 A, the current limit is fine-tuned to 0.5 A by setting the reference voltage to 0.25 V.

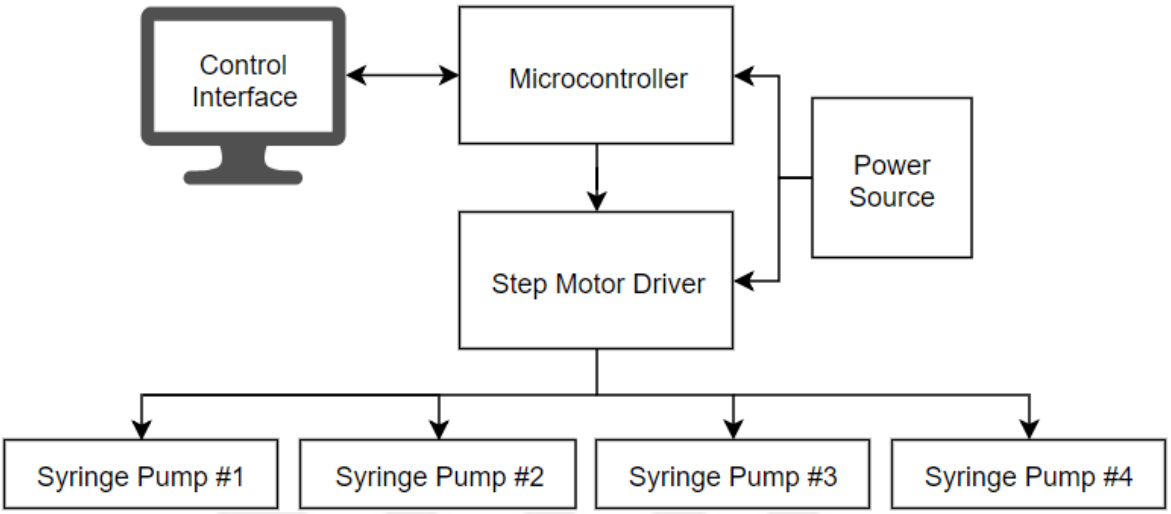

Figure 2.3. Schematic diagram of automated platform.

Each pulse sent to the STEP pin of the driver corresponds to one step of the motor, with the direction determined by the state of the DIR pin. An external voltage source was connected to the VMOT pin of the drivers, and the motors were linked to the driver's coil pins, following the coil connection information provided in the motor's datasheet. The step and direction pins of the driver were connected to the Raspberry Pi's GPIO pins, which are necessary for program-controlled motor action. Lastly, to reference a common ground, the ground pins were interconnected. The complete system, after assembly, is showcased in Figure 2.4.

The primary benefit of syringe pumps lies in their versatility. The working range of these instruments can be easily adjusted by swapping out the syringe for one with a different diameter. This feature allows for the customization of fluid volumes and flow rates. Additionally, individual syringe pump modules are designed to be interconnected, enabling the assembly of complex dosing systems or comprehensive microreaction systems.

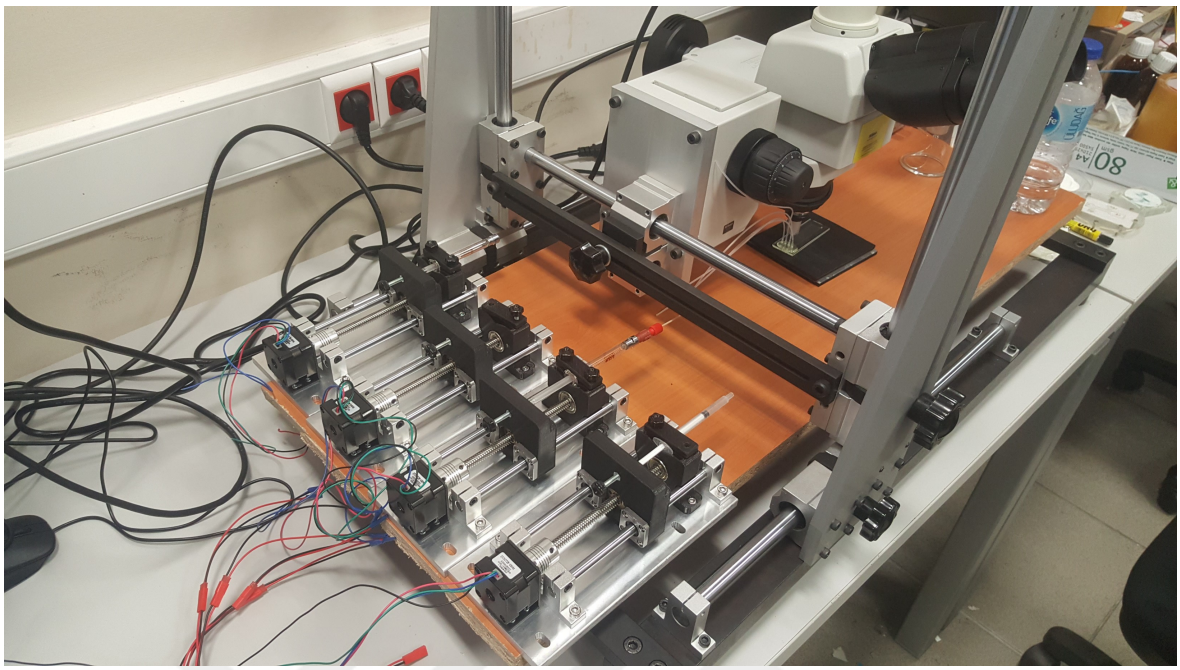

Figure 2.4. Fabricated syringe pumps.

For precise control of each syringe pump, including varying flow rates and directions, a Graphical User Interface (GUI) has been developed using the Integrated Development Environment of Qt. This interface allows for intuitive and detailed management of the syringe pumps' operations. A screenshot of this user interface is displayed in Figure 2.5. Furthermore, the GUI leverages PyQt5 which are Python bindings for Qt5. It eases the design of the control interface through Python programming. This integration enhances the flexibility and functionality of the system, allowing for a wide range of manipulations in the automated platform.

In a detailed study designed to assess syringe pump performance, a series of tests were carried out using a 1/32 microstep setting to measure the pump's displacement over a period of 600 seconds at various step frequencies. The summarized results presented in Table 2.1 offer essential insights into the step frequency's impact on pump displacement. The table details start and stop points in millimeters, along with the corresponding speeds in micrometers per second. It encompasses a range of step frequencies from 0.5 Hz to 8 Hz.

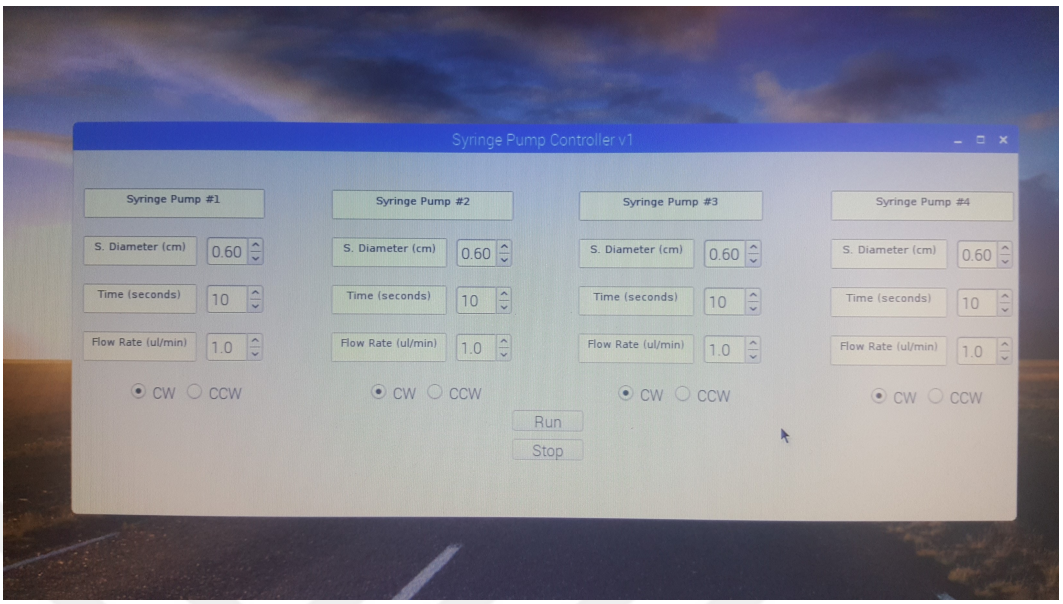

Figure 2.5. Graphical user interface to control and operate syringe pumps.

The data shows a clear trend of increasing displacement and speed with higher step frequencies, suggesting a linear relationship between step frequency and displacement rate. Additionally, this linear trend, achieved under the precision of a 1/32 microstep setting, underscores the pump's mechanical rigidity, indicating its ability to maintain consistent performance and precise operation under various mechanical conditions.

Table 2.1. Syringe pump displacement for duration of 600 seconds in varying speeds.

Step frequency (Hz)	**Start (mm)**	**Stop (mm)**	**Speed (µm/s)**
0.5	52.97	52.65	0.53
1	52.65	51.96	1.15
2	51.96	50.59	2.28
4	50.59	47.62	4.95
8	47.62	41.61	10.02

2.3. Fabrication Methods of Microfluidic Chips

Microfluidics are characterized by their use of extremely small volumes, typically in the nanoliter to microliter range. They have channel dimensions spanning from 1 to 1000 micrometers in width or height. Microfluidic chips that are made from materials like glass, silicon, metals, polymers, and ceramics, commonly utilize polymers such as PDMS, PMMA, fluoropolymers, COP, and thiol-ene polymers [69]. The production of these chips has evolved from initial silicon/glass-based micromachining, involving photolithography, etching, and photoresist removal, to polymer-based molding and now to 3D printing. Original microfluidic chips that were crafted on silicon/glass substrates, required processes like thermal fusion or adhesive methods using high temperature and pressure for enclosing microchannels. Despite their thermal stability, chemical resistance, and optical transparency, high cost and extensive clean-room fabrication of these chips have led researchers to consider polymer-based molding as a more cost-effective and accessible option [7].

The prevalent method for microfluidic chip fabrication uses PDMS, an elastomeric material, to replicate microstructures from a master mold. The master mold is created through photolithography, transferring a CAD(computer-aided design)-generated pattern to a photoresist layer on a mask. PDMS prepolymer is poured onto the mold, then solidified and bonded to a glass substrate through the application of oxygen-plasma treatment [70]. While this method is cost-effective and efficient, it has drawbacks such as chemical absorption, low durability under high pressure, and waste of time in iterative design optimization. Additionally, it can create entry barriers for research groups new to the field of microfluidics by limiting accessibility and innovation.

Evolution in additive manufacturing by 3D printing have simplified microfluidic chip fabrication. Stereo lithography (SLA) makes use of ultraviolet (UV) laser exposure to polymerize resin layers, providing high resolution and surface finish. The introduction of UV liquid-crystal display (LCD) screens enables quicker production in SLA by projecting layer images onto resin for selective curing. Thus, it becomes a

potential choice for 3D printing microfluidic chips on a large scale. However, the use of resin in this process presents problems in terms of biochemical compatibility [71]. On the other hand, fused deposition modeling (FDM) melts thermoplastic filament layer by layer with cost-effectiveness. It has the disadvantages of lower accuracy and limited material options. These 3D printing techniques have opened up new possibilities in microfluidic chip production. SLA excels in precision and surface quality, while FDM provides affordability and accessibility, despite some limitation of high accuracy and limited range of transparent materials [72]. Additionally, both methods may face challenges in achieving the same level of chemical compatibility and durability as silicon or glass-based chips.

Throughout the thesis, PMMA was selected for microfluidic chip fabrication because of its superior optical clarity, allowing light to pass with little distortion or absorption. It is essential for monitoring and analyzing interactions in the microfluidic chip. Two distinct fabrication methods, laser ablation and micro-milling, are investigated creating microfluidic channels within the PMMA substrate.

2.3.1. Laser Ablation

Laser micromachining stands out as a highly versatile and cost-efficient method for fabricating microfluidic devices. Commercially available benchtop laser cutters facilitate the creation of a wide range of microfluidic designs without the need for specialized moulds or equipment, thus streamlining rapid prototyping and the iterative design process [73]. In this process, a suitably powered laser traverses the PMMA surface, vaporizing minute volumes of material to form microfluidic channels, rather than cutting entirely through the material. The precise adjustment of laser characteristics, including power, speed, focal distance, and the choice between a focused or unfocused beam, is essential. These parameters greatly impact the accuracy of the channel's depth, width, and overall shape [74–76]. The primary drawback of laser ablation is the diminished optical quality of the micromachined surfaces, forming bulges or humps attributed to melting, thermal stress, and material ejection caused by laser

irradiation [77]. These result in pore formation and residue deposition with high surface roughness, which can limit the usage of laser cutter devices. Furthermore, this technique often entails increased surface roughness in channels and variability between devices due to deformation in the heat-induced sealing process [7].

This technique was utilized to fabricate microfluidic chips used in droplet generation experiments. Figure 2.6 describes the flow diagram to produce microfluidic chip. PMMA (Product code: 10-0671-0349-1.0-01) polymer substrates with 1 mm thickness were purchased from Microfluidic ChipShop Company (Germany). The design of the microfluidic channels was initially drafted in AutoCAD, and then these designs were adapted into laser cutting trajectories using the integrated software of the laser cutter.

The configuration of laser parameters was adjusted using the dedicated software. It was focused on laser power, speed, and distance-to-focus, the latter being the distance between the stage and the laser's focal point. Microchannels were engraved under varied settings, experimenting with laser power (5%, 7%, and 10% of maximum power) and speed (2%, 5%, 7%, and 10% of maximum speed). The optimal parameters for microchannel fabrication were finalized at 10% power and 7% speed. Inlet and outlet ports were configured at 10% power and 2% speed, whereas connection ports underwent ablation in three passes.

After laser-ablating microchannels with the desired geometry, the PMMA chips were cleaned with baby shampoo and deionized (DI) water to remove polymer residue. They were then rinsed in DI water and dried with N_2 gas. To seal the microchannels, PMMA slides were aligned between two glass slides and wrapped by aluminum foil. The hydraulic press machine employed for this purpose, specifically the Carver 3851 CE-0 from the USA, was set to apply 16 bar pressure and maintain a temperature of 80 °C across the entire block for a duration of 40 minutes to ensure uniform heating. The press machine's lower and upper plates were set to the same temperature during the bonding process. Afterward, the substrates naturally cooled down to room temperature before being removed from the press.

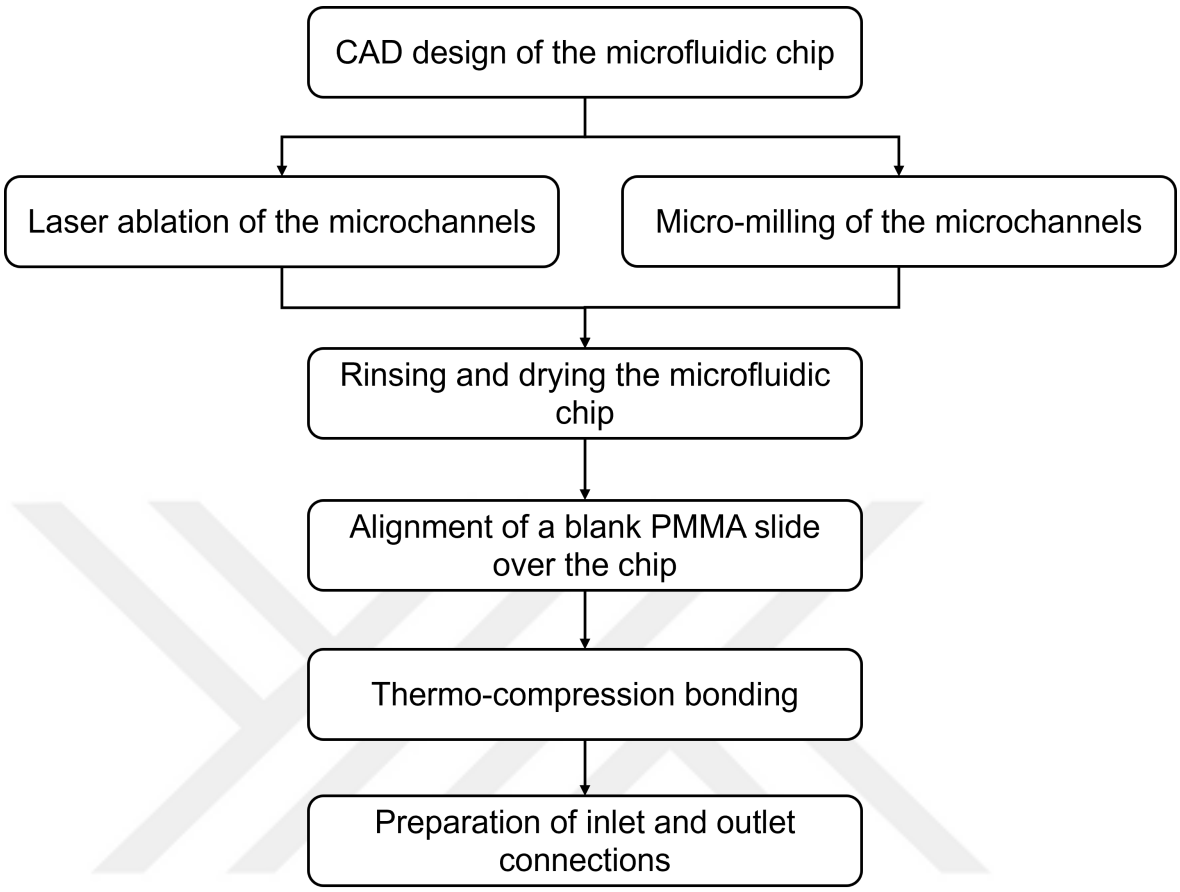

Figure 2.6. The flow diagram of microfluidic chip fabrication process by laser-ablation and micro-milling.

2.3.2. Micro-milling

In micro-milling, computer numerical control systems are commonly used to control tool speed and position. These systems receive instructions from a computer, often using files from CAD or CAM (computer-aided manufacturing) software. By this technique, channels, through holes, and chambers may be fabricated. Unlike traditional methods, micro-milling experiences less thermal expansion due to the higher surface-to-volume ratio at the micro-scale, aiding in cooling [78].

The characteristics of groove edges in micro-milling are influenced by spindle speed, feed rate, and depth of cut [79]. To enhance machining outcomes, it is suggested to keep the processing temperature below 70 °C for improved bottom surface

and edge shape [80]. The photo depicted in Figure 2.7 captures a moment from the micromachining procedure.

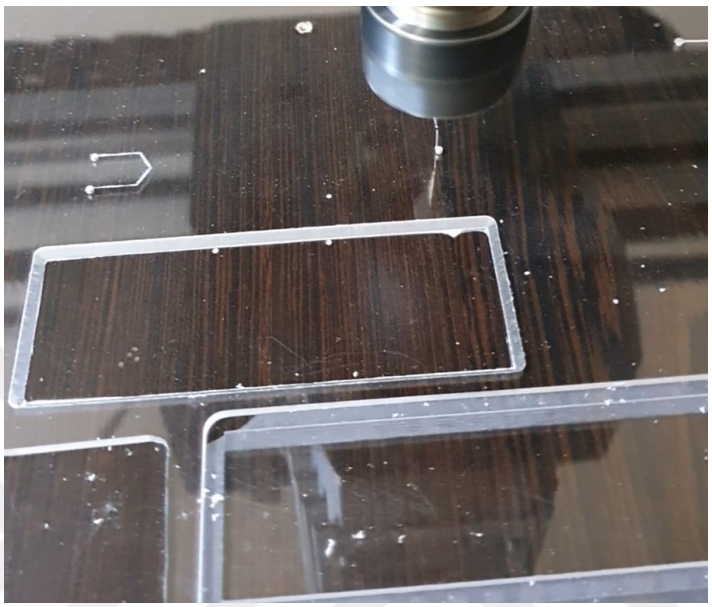

Figure 2.7. Micromachining process during fabrication of the microchannels.

The fabrication sequence is largely analogous to that used in laser ablation, with the primary variation being the substitution of the microchannel fabrication method and some adjustments to specific parameters. The construction material employed for the microfluidic substrates was PMMA (product code: 10-0677-0347-2.0-01), bought from Microfluidic ChipShop Company in Jena, Germany, with a standard thickness of 2 mm. Microchannels embodying the specified geometries were precision-machined by milling using a desktop CNC router. Following the formation of microchannels, a thorough rinsing with deionized water was conducted to eliminate any residual polymer. It was succeeded by a drying process utilizing clean nitrogen gas. Subsequently, the microchannels were immersed in a solution comprising a 1:4 ratio of chloroform to ethanol. To finalize the microchannel sealing process, PMMA slides were aligned and positioned between two glass slides. The bonding process for the microfluidic chip was similar to laser ablation, with slight adjustments: a pressure of 16 bar and a temperature of 85 °C for 60 minutes. Figure 2.8 provides an example of a microfluidic chip fabricated using the micro-milling technique.

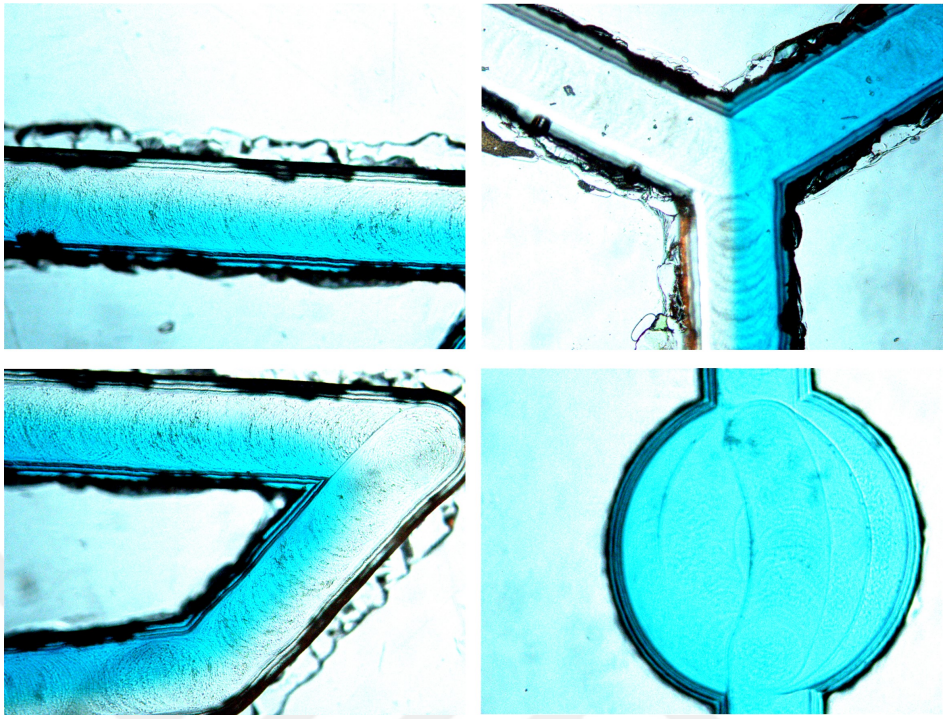

Figure 2.8. Different sections of microfluidic chip fabricated by micro-milling.

3. DROPLET MICROFLUIDICS

Continuous flow microfluidics maintains a steady flow of liquid through microchannels, while droplet microfluidics focuses on creating and manipulating discrete droplets within microchannels [81, 82]. This chapter introduces droplet microfluidics, highlighting the generation and manipulation of droplets with distinct colors within automated microfluidic platform.

3.1. Overview of Droplet Microfluidics

Laminar flow, where viscous forces are dominant and characterized by smooth, constant fluid motion, is maintained for Reynolds numbers (Re) under 2300 [83]. In contrast, turbulent flow occurs at higher Reynolds numbers and is dominated by inertial forces. This leads to eddies, vortices, and other flow instabilities [84]. Unlike continuous flow microfluidics, droplet microfluidics enables very efficient handling of solutions by providing volume reduction. Since processes, such as heating and diffusion, take less time for small volumes, it enhances speed of biological and chemical assays. Moreover, mixing solutions in a confined space within a microfluidic chip is efficient, and multiple liquid droplets can be moved simultaneously by regulating pressure at the chip's ends [85]. In the literature, different applications have been demonstrated like synthesis of nanoparticles, DNA analysis, analysis of chemical and biological reactions [86]. With a specialized algorithm, integrated with a microfluidic reactor, reaction conditions were autonomously adjusted using historical data to produce nanocrystals with specified optical characteristics by determining the best sampling points for attaining a desired emission peak wavelength [87].

Droplets may be formed passively or actively using two different phases (like oil and water) interchangeably as dispersed and continuous phases. Active methods in droplet microfluidics involve technologies like dielectrophoresis (DEP) and electrowetting on dielectric (EWOD) that enable the integration of electrodes into microdevices.

These technologies provide precise electrical control over droplet formation, offering new opportunities for manipulating fluids on a microscale [88].

Co-flowing, cross-flowing and flow-focusing are three passive methods that utilize channel geometry to control the generation of droplets as shown in Figure 3.1 [89]. Co-flowing method utilizes two coaxial microchannels where inner channel introduces the dispersed fluid phase while continuous phase flows through the outer channel in the same direction. As to cross-flowing method, the channels containing the dispersed phase and continuous phase intersects, generally perpendicular to each other. The two phases form an interface at the junction, and as continuous phase flows, the dispersed phase entering the main channel generates droplets. Finally, in the flow-focusing, the dispersed and continuous phases flow coaxially and they are forced through a narrowed barrier leading to uniform droplet generation. For all the methods, the droplet size is affected by continuous and dispersed phase flow rates, viscosity of the phases and channel geometry.

3.2. Experiments with Commercially Available Microfluidic Chip

The layout of the microfluidic chip used for droplet production is given in Figure 3.2. The microfluidic chip, identified as "Fluidic 488" with a product code of "10000511", was purchased from microfluidic ChipShop. It is structured in the size of a microscope slide, measuring 75.5 mm x 25.5 mm x 1.5 mm, and includes multiple aqueous channels that converge before intersecting with an oil channel. The chip has five inlet ports: two for the continuous phase and three for dyes. An interesting aspect of the design is the management of the oil flow, crucial for the continuous phase. The oil is pushed by a single syringe pump into a tube that splits into two, connecting to two pinheads on the chip. However, this setup presents a challenge in ensuring equal distribution of the oil flow, as the flow rate can vary due to differences in bending of the external tubing. This detail highlights the complexity and precision required in microfluidic system design, especially when dealing with multiple fluid inputs and the need for consistent flow rates.

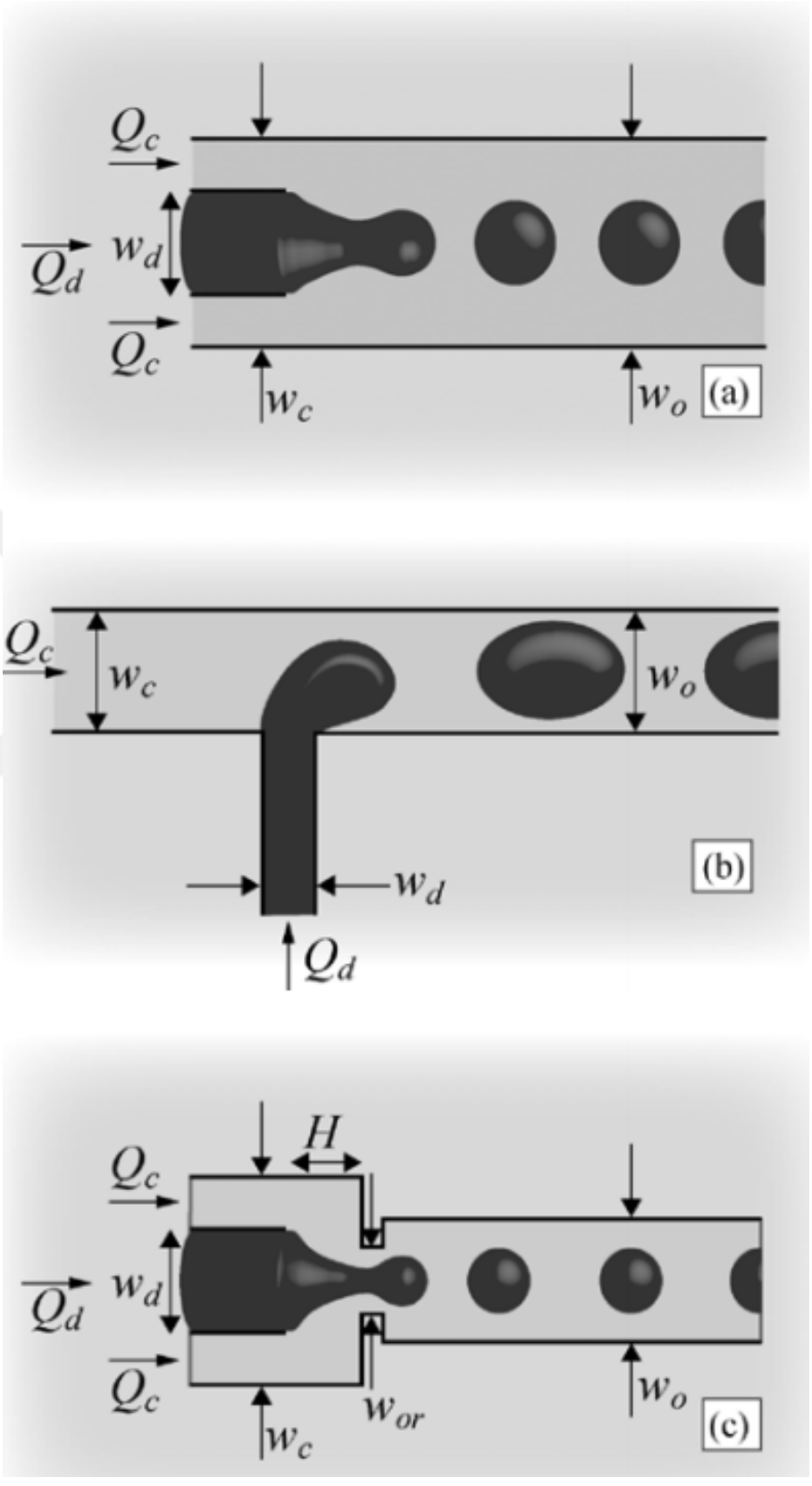

Figure 3.1. Passive droplet generation methods of (a) co-flowing, (b) cross-flowing in T-shaped junction, (c) flow-focusing [89].

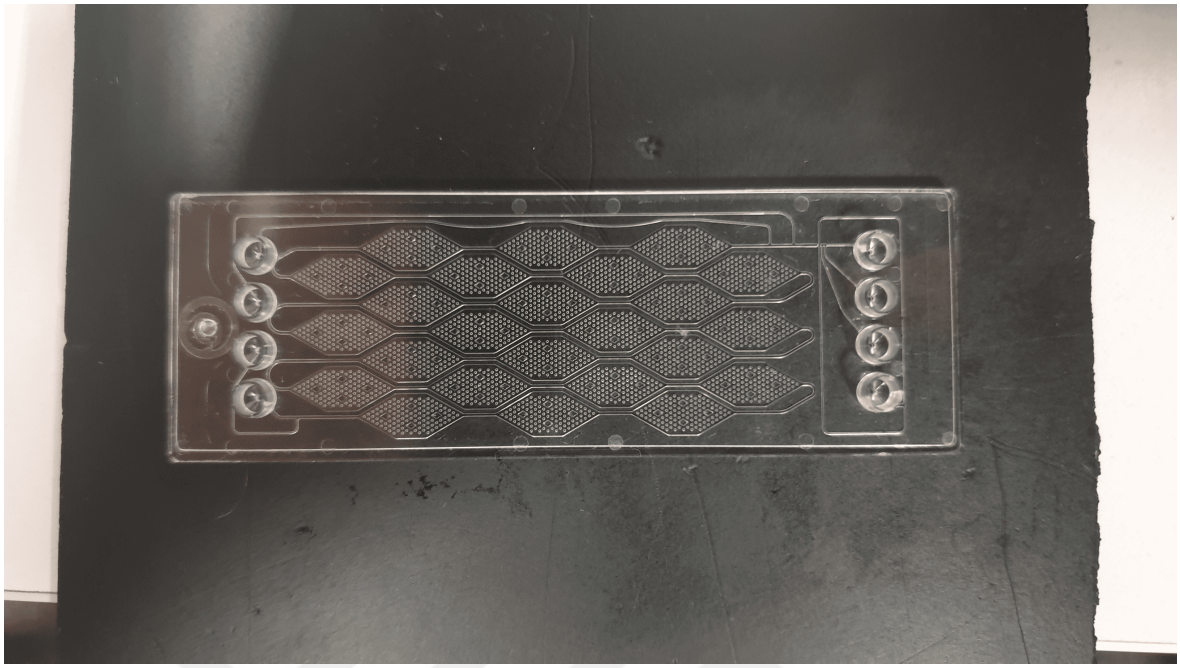

Figure 3.2. The layout of the microfluidic chip used for droplet production.

In the process of establishing a leak-proof connection to the microfluidic chip, several approaches were attempted. Initially, plastic pinheads were used to connect polyetheretherketone (PEEK) tubes to the chip's inlet ports, but this method failed to prevent leakage.

The second approach involved pouring hot silicon over the plastic pinheads and inlet ports to create a more rigid connection. However, this method also proved ineffective as the strain exerted by the PEEK tubes on the silicon before it hardened made the microfluidic chip unusable. The final and successful method involved reshaping syringe needles and using connectors to attach them to the plastic pinheads, as illustrated in Figure 3.3. This solution achieved stable, leak-proof connections without damaging the microchip inlets.

In Figure 3.4, the complete experimental setup for droplet generation and manipulation is shown. Each syringe pump was strategically positioned within a stable environment, supported by an aluminum cubic frame structure for enhanced stability and precision.

Figure 3.3. The connections for microfluidic chip.

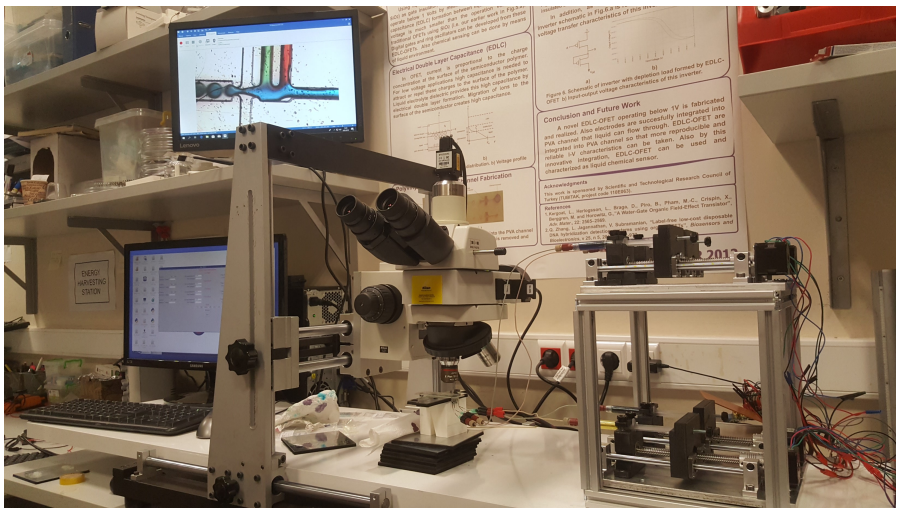

Figure 3.4. The experimental setup for droplet generation and manipulation.

3.2.1. Droplet Generation

The formation of droplets is also characterized by capillary number (Ca) which is directly proportional to the velocity of the fluid flow and the viscosity of the fluid and inversely proportional to the surface tension at the water/oil interface. A low value of capillary number means that interfacial tension stress is stronger than viscous stress. That results the droplets to decrease their surface areas by forming spherical shapes. In summary, the interaction between shear stress and surface tension in a system where an aqueous phase is dispersed within an immiscible continuous phase leads to the destabilization of the aqueous phase. This destabilization ultimately results in the formation of spherical droplets.

To maintain the droplet's shape within a lengthy microfluidic channel, surfactants are introduced to stabilize the interface between the oil and water phases [90]. To facilitate the generation of droplets, a lower capillary number is essential. Consequently, the continuous phase is deliberately chosen to be more viscous, aiding in the droplet formation process.

For the formation of water-in-oil droplets within hydrophobic channels, or oil-in-water droplets, hydrophilic channels are required. Within uniformly hydrophobic channels, an oil/water fluid pair will flow as a sequence of water droplets carried within the continuous oil phase. This behavior relies on the channels maintaining consistent hydrophobic properties spatially and temporally [91].

Slight changes in driving conditions can cause rapid shifts between droplet production and laminar flow. One important driving parameter is the flow rate fraction that is defined as the ratio between the total flow rate of the coloured dyes and the combined flow rate of the oil and coloured dyes. At high flow rate fraction, resulted from relatively lower flow rate of continuous phase than the total flow rate of the dispersed phases, laminar flow is induced. In Figure 3.5(a), an image of the laminar flow without generating droplets can be seen.

Surfactants align perpendicular to the surface and compose of a compact polar head and a long hydrophobic tail. They are attracted to the interface separating the droplet and the carrier fluid surfactant layers on two adjacent drops interact together to retard the merging by applying electro-static repulsion between the interfaces or slowing down the hydrodynamic flow along the interface.

In initial experiments conducted without surfactants, observations revealed that droplets were unable to maintain their stability. Therefore, the surfactant was added to the coloured dyes with the relative volume value of 0.5-1%. After the addition of the surfactant, stable droplets were generated as in Figure 3.5(b).

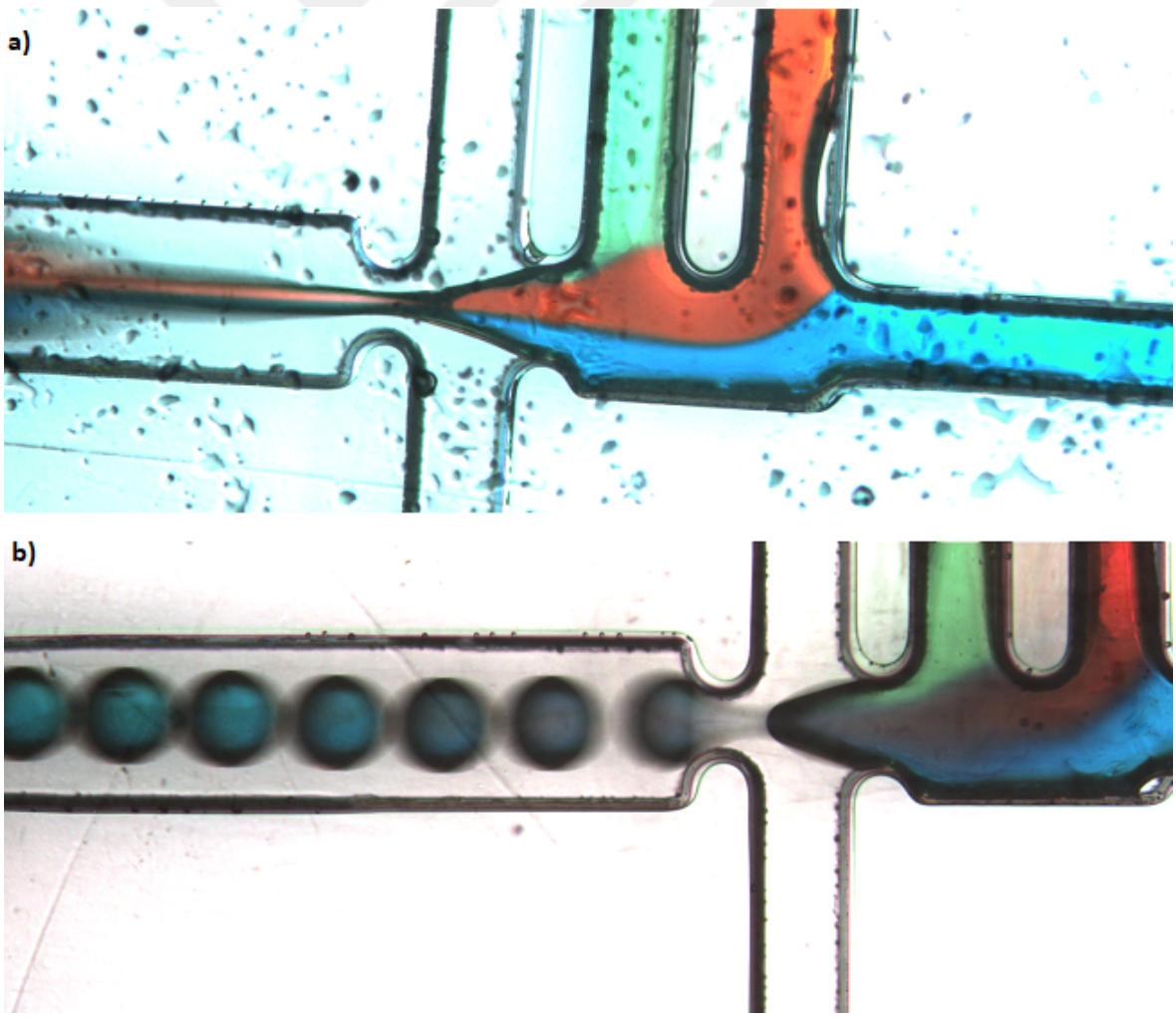

Figure 3.5. (a) Laminar flow (b) droplet generation.

3.2.2. Droplet Manipulation

After being able to generate droplets, experiments were carried out to manipulate droplet size and droplet colour by controlling the syringe pumps. The colour of the droplets can be controlled by varying the flow rate of related syringe pump. After the red, blue and green dyes are combined in the junction, continuous phase shears off to form droplets.

For a total constant flow rate of each individual dye, each colour can be generated by dominating the total flow rate. The concentration of dyes in each droplet is directly related to its flow rate. The different coloured droplets from green to blue in Figure 3.6 were generated sequentially. To form each colour, related syringe pump was kept at flow rate of 0.5 µL/min while the flow rate of continuous phase is 1.5 µL/min.

The microscope image showing the array of droplets with different concentrations of dyes is given in Figure 3.7. As shown in the figure, different tones of droplets can be generated consecutively. However, syringe pumps have slow settling times that limit repeatability and responsiveness to generate monodisperse droplets sequentially from multiple flows. With some passive techniques on the microfluidic chip such as droplet splitting with T-junction, dummy droplets can be removed from the array to obtain the desired composition of droplets.

The microfluidic system allows for the adjustment of droplet size by varying the flow rate fraction. In Figure 3.8, microscope images were captured within a microfluidic chip while maintaining constant total flow rates for colored dyes, and simultaneously altering the continuous phase flow rate. As the flow fraction rate increased from 0.35 to 0.55 (continuous phase flow rate decreased), droplet diameter increased from 105 µm to 145 µm. This illustrates the direct relationship between flow rate fraction and droplet size, providing a valuable parameter for fine-tuning the system for specific applications and requirements.

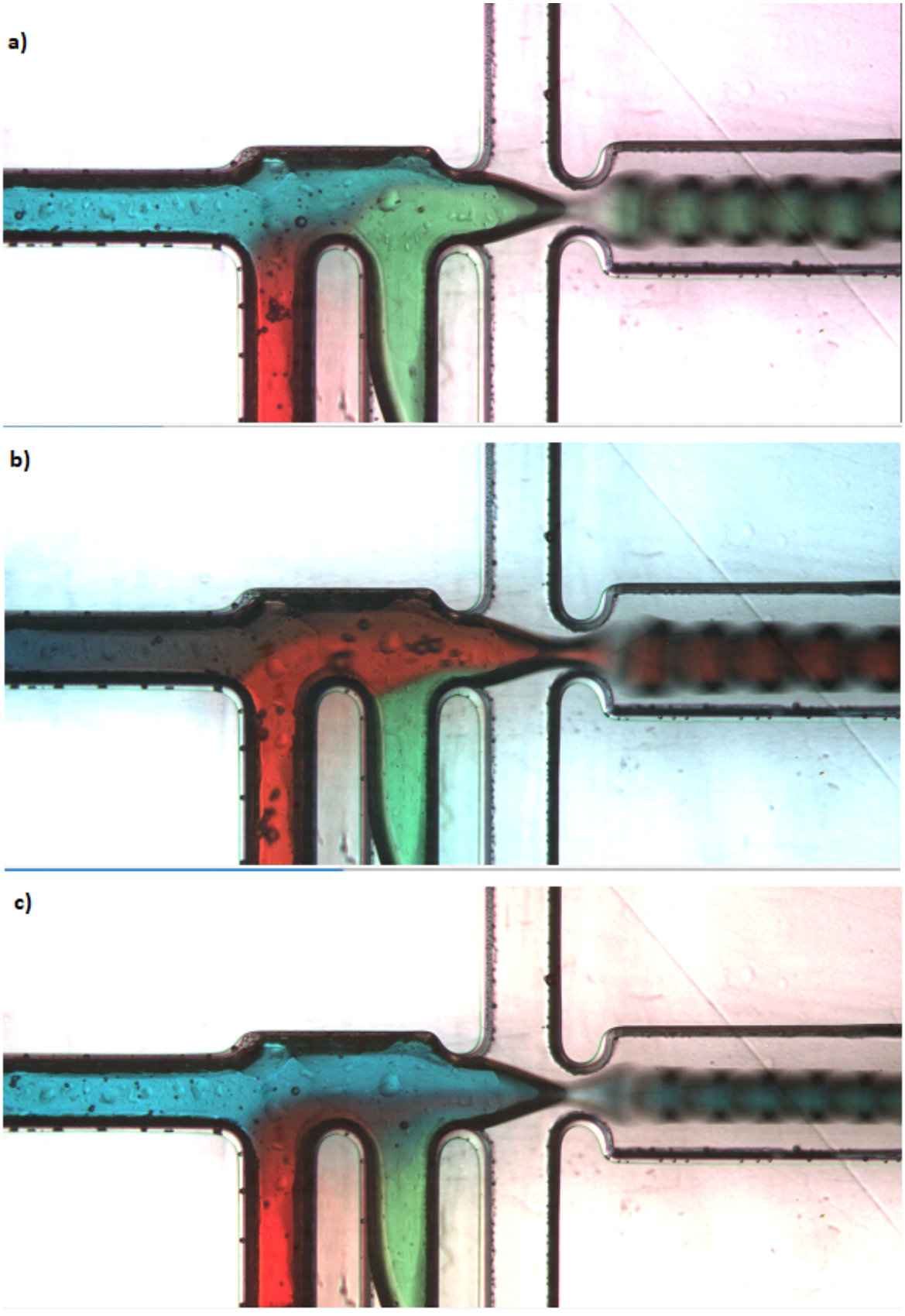

Figure 3.6. Different coloured droplets.

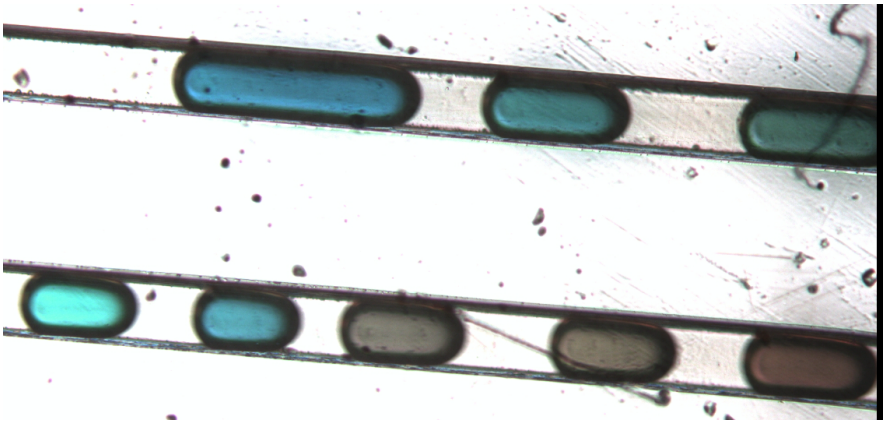

Figure 3.7. The array of droplets with different concentrations of dyes.

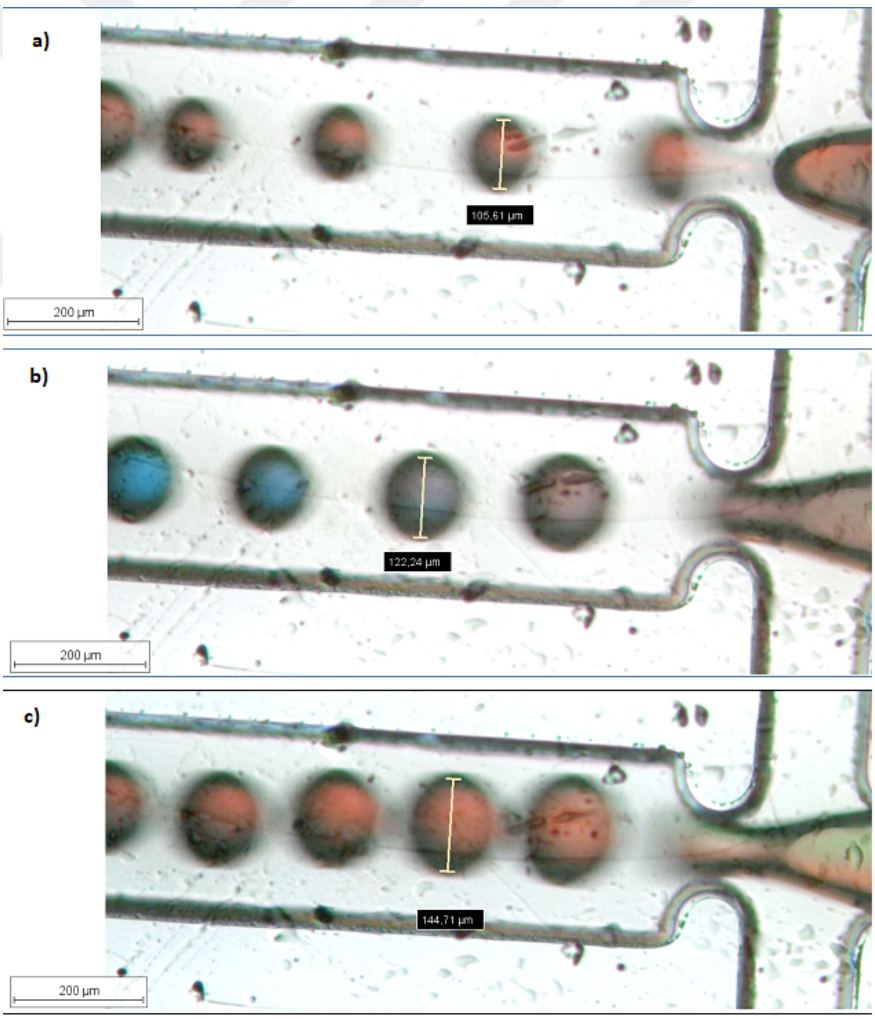

Figure 3.8. The diameter size of droplets for water fraction of 0.35, 0.45 and 0.55, respectively.

3.3. Experiments with In-house Fabricated Microfluidic Chip

After droplet generation and manipulation with commercially available chips were succeeded, it was aimed to repeat the experiments with in-house fabricated chips. To carry out this objective, two different geometries for passive droplet generation within a long folded microfluidic channel were designed in AutoCAD. The first design Figure 3.9(a) depends on the flow-focusing method. The dispersed phase is squeezed by two symmetrical continuous phase channels forcing drops to detach. It has the advantages of having more flexibility in terms of droplet size and droplet frequency due to the symmetric design.

The second one is the T-junction Figure 3.9(b), in which the dispersed phase is pumped into the continuous phase orthogonally. As the dispersed phase enters the main flow channel, shear forces elongate the head of the dispersed phase until a segment eventually separates and relaxes into a sphere or plug shape due to the interfacial tension.

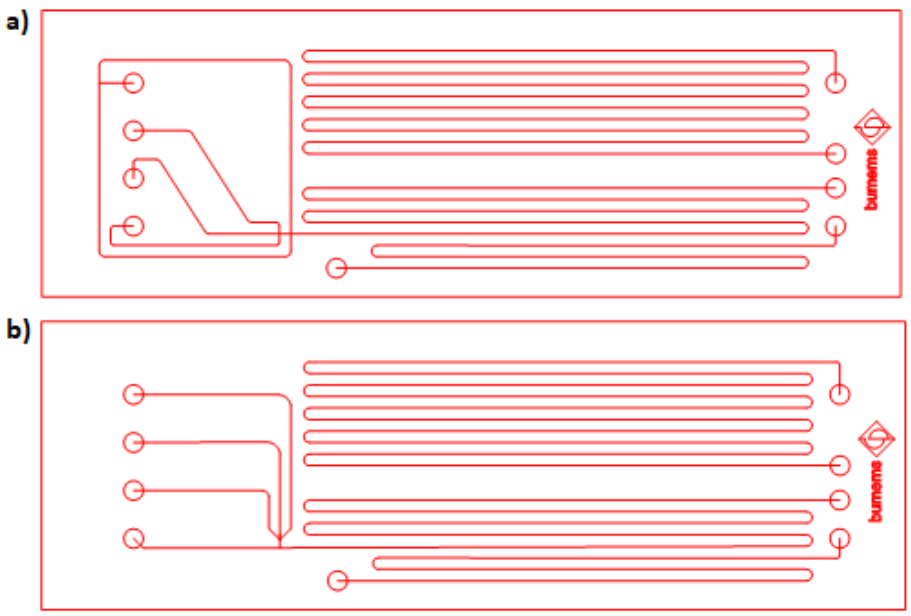

Figure 3.9. The chip designs to generate droplets with (a) flow-focusing method, (b) T-junction method.

Following the fabrication of microfluidic chips through the laser-ablation method, they were integrated into the automated microfluidic platform to test both efficiency of the system and microfluidic chip itself as shown in Figure 3.10. The connections to the microfluidic device were established using customized sterile pipette tips, a PMMA block featuring a 90-degree inlet port, PDMS serving as a sealing agent, and PEEK tubing. Subsequent to testing, various optimizations were implemented in the software and mechanical components based on the obtained results.

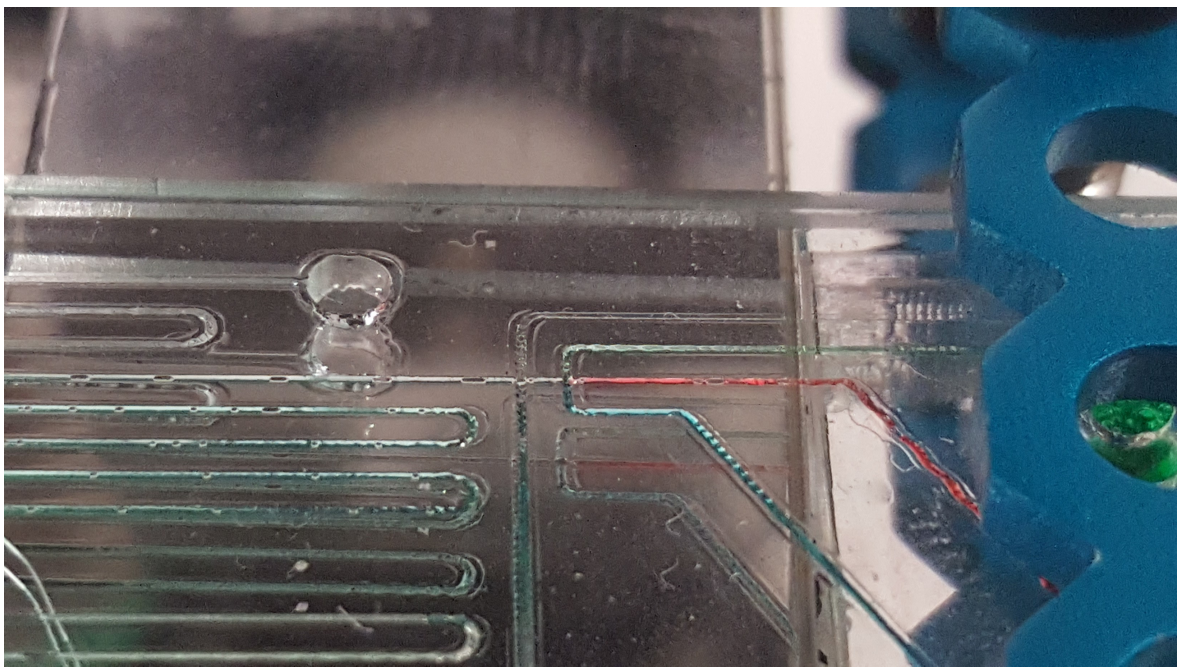

Figure 3.10. Microfluidic channels zoomed to show flow and generated droplets.

In Figure 3.11 and Figure 3.12, the microscope images display the formation of oil droplets against various colored backgrounds in the flow-focusing and T-junction methods, respectively. These figures provide a clear visualization of the only generation of oil droplets in each method. While the size and frequency of these droplets can be adjusted by altering flow rates, the production of water droplets within the oil phase was not successfully achieved in these microfluidic chips.

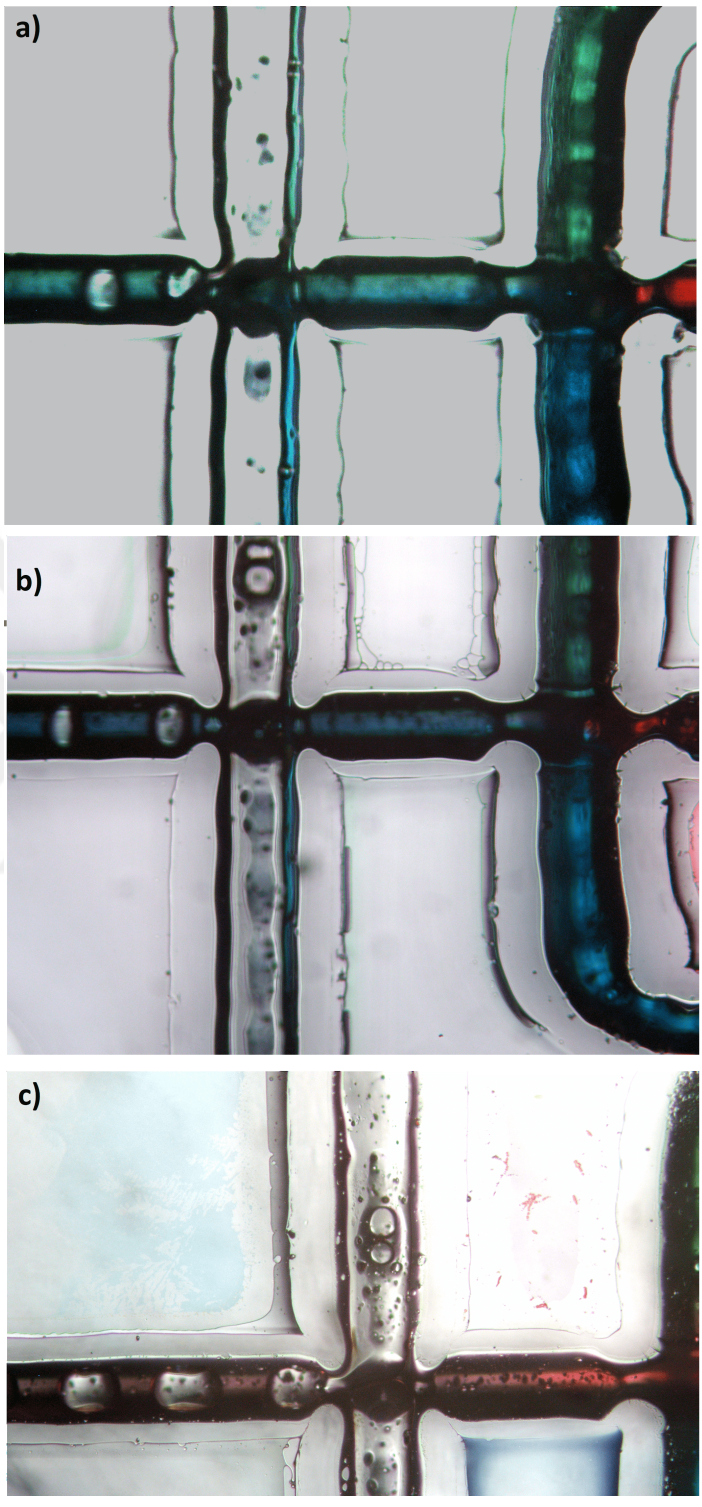

Figure 3.11. The microscope image showing oil droplets with different coloured background in flow-focusing method.

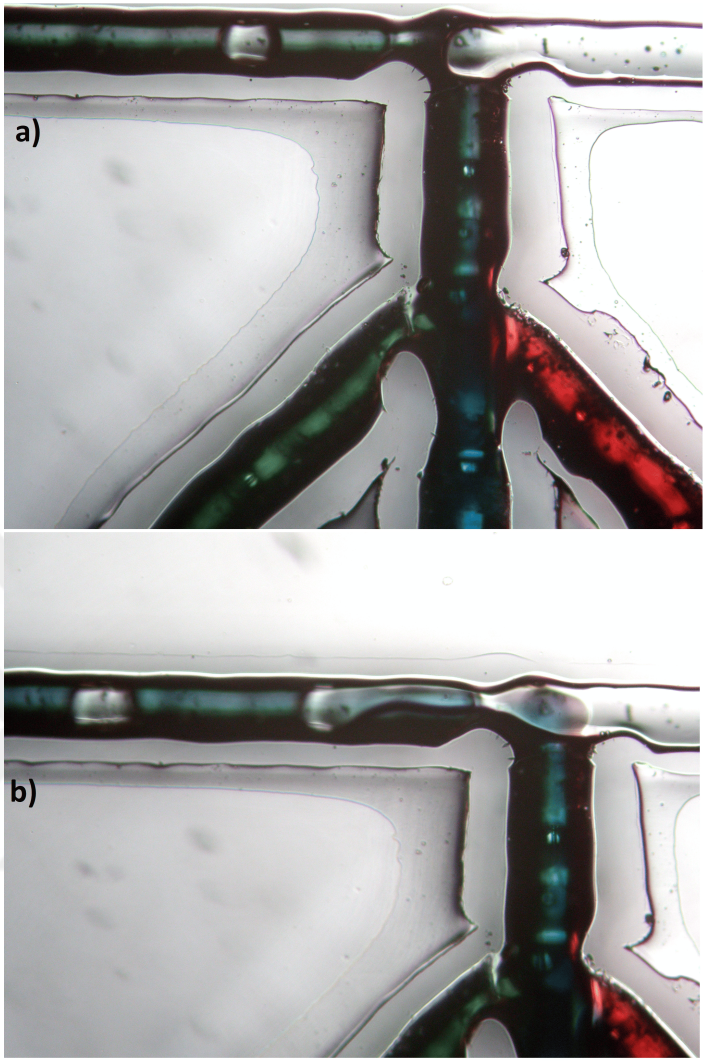

Figure 3.12. The microscope image showing oil droplets with different coloured background in T-junction method.

3.4. Discussion

The syringe pump lacks a feedback loop, making precise flow rate control difficult and resulting in slow response times ranging from minutes to hours. It faces reliability issues in generating droplets due to step size frequency and mechanical factors that cause vibrations, especially at low flow rates [62]. On the other hand, raising the flow rate introduces challenges in dynamically adjusting droplet size and concentrations. Rubber syringes, while cost-effective, exhibit non-linearities due to their elasticity, and glass or stainless-steel syringes, although less prone to non-linear behavior, are more

expensive. The system's elasticity promotes a more consistent flow rate and improves stability, but at the cost of reduced responsiveness.

As to the in-house fabricated PMMA chips with laser ablation, it is concluded that laser ablation can significantly influence droplet formation. The process creates rough surfaces and V-shaped channels, possibly altering the material's inherent hydrophobic nature. The increased surface roughness enhances hydrophilicity, favoring the formation of oil-in-water droplets, contrary to the usual water-in-oil expectation in. Additionally, V-shape cross-section of the laser ablated chip impacts fluid dynamics, potentially leading to a preferential encapsulation of oil by water resulting water phase to flow through the floor of the channel while oil phase flows over the water. This highlights the critical role of fabrication techniques in dictating the behavior and properties of microfluidic devices, especially in droplet generation applications.

The repeatability and responsiveness of the microfluidic system is influenced by several factors, encompassing the characteristics of the microfluidic chip, the syringe pump, the syringe, and the type and length of tubing. Addressing and comprehensively analyzing each of these parameters is imperative to eliminate sources of unreproducible results. The upcoming chapter will undertake a detailed exploration by employing an electrical analogy and utilizing electrical simulations to optimize the responsiveness of the microfluidic system while ensuring flow stability.

4. ANALYSIS AND OPTIMIZATION USING ELECTRICAL ANALOGY

This chapter discusses a novel sample injection method in microfluidics, comparing different approaches. The chapter highlights the use of electrical analogy to understand and analyze the complete microfluidic system. It presents a detailed electrical circuit representation of the experimental setup and discusses the impact of damping elements on flow stability. The chapter concludes by emphasizing the importance of finding a balance between damping and responsiveness in optimizing the dynamic performance of the system.

4.1. Novel Sample Injection Method

Exact and sustainable mixing ratios can be achieved using syringe pumps in closed-loop feedback control by incorporating multiple flow-rate sensors and a controller as shown in Figure 4.1(a). While this approach ensures accuracy, it makes the overall system expensive, complex and large. Alternatively, a vacuum source in the form of a single syringe pump withdrawing liquids from the outlet port, can be used to introduce the sample and reference liquids into the mixer of the microfluidic chip as shown in Figure 4.1(b). In this case, their mixing ratios change with the liquids input pressure and hydraulic resistance differences [61].

Alternative methods, such as push-pull or infusion-withdrawal syringe pumps, are also prevalent in similar applications. These methods employ a simultaneous infusion and withdrawal mechanism, executed through two distinct syringes. In this setup, while one syringe infuses the fluid, the other concurrently withdraws it from the outlet, thereby creating a continuous and controlled flow system. This approach ensures a balanced and precise fluid handling that is useful for various applications requiring meticulous volume control.

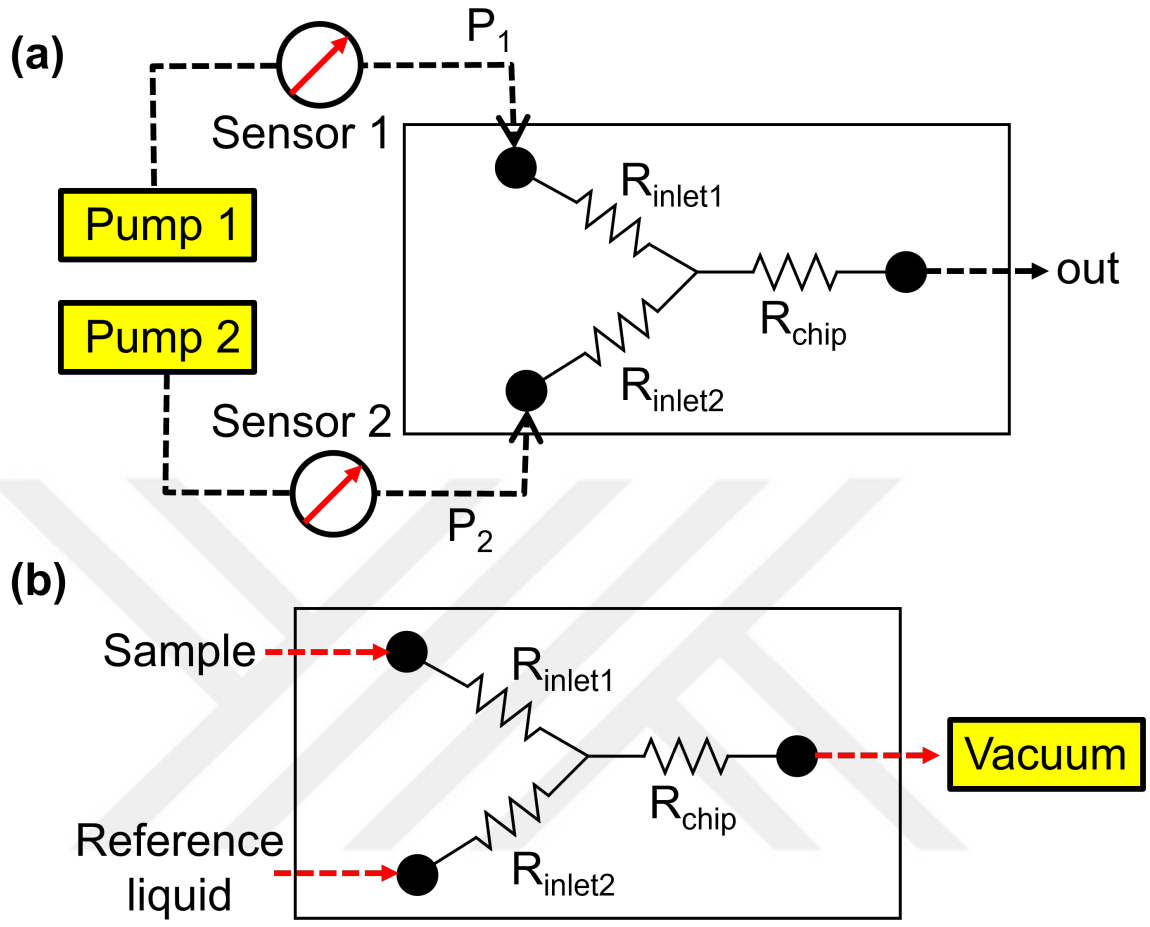

Figure 4.1. Two common methods to introduce liquids with desired volumetric ratios for mixing (a) with closed-loop feedback (b) single syringe pump withdrawing liquids from the outlet port.

Two syringes are mechanically coupled to operate in balance, as illustrated in Figure 4.2(a) [63]. The push-pull syringe system was employed in which one syringe was connected to the channel or tissue inlet, pushing liquid into it, while another syringe connected to the outlet was pulled to extract the solution directly from the channel or tissue [63]. This type of push-pull system provides pulse free, high accuracy and high precision flow to bioreactor systems.

In Figure 4.2(b), two distinct syringe pumps were employed in a push-pull configuration to enhance flow stability [64]. This arrangement ensures a more stable flow within the channels.

The application of push-pull systems has been widespread, particularly in scenarios involving the injection of solutions into living tissues, such as brain tissue [92]. A balance between injected volume and displaced volume was sought by collecting the displaced liquid from the outlet as the input liquid is injected to the inlet at the same time. It was also used to seed cells with continuous perfusion of cell-loaded solution through scaffold [93].

A sample introduction method for microfluidic systems utilized pressure-induced push-pull flow with a switch valve, enhancing precision and control of sample plug injections in various channel structures maintaining consistent performance across different chip geometries [94]. In another study, the push-pull system was employed in an affordable, disposable laboratory cartridge for nucleic acids-based disease diagnosis, where reagent transportation was accomplished using a combination of push and pull forces connected to pneumatic inlets at the cartridge's base, controlled two syringe pumps [95].

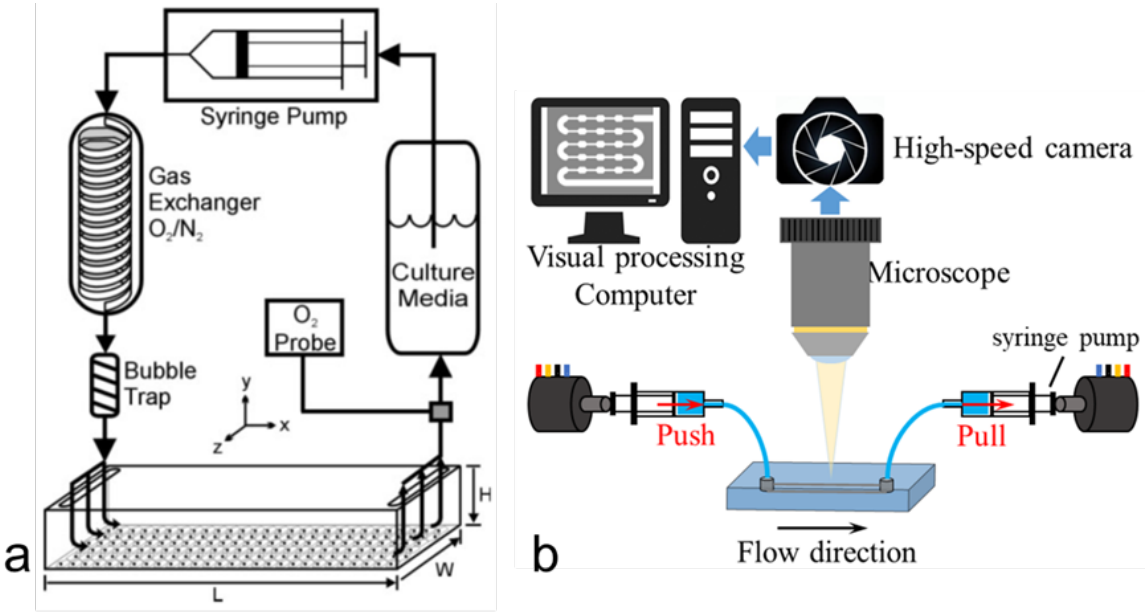

Figure 4.2. Examples of push-pull syringe systems (a) with single syringe pump [63] (b) with two syringe pumps [64].

A practical solution to the mentioned problems is presented in Figure 4.3. A single pump's mechanical motion is linked to two syringes with varying cross-sectional areas (A_{ind} and A_{mix}), where the smaller syringe pushes a reference liquid into the microfluidic system at a fixed flow rate (Q_{ind}), and the larger syringe pulls liquids (mixture of both inlets) from the outlet port at a fixed flow rate (Q_{mix}). The other inlet of the microfluidic system remains unconnected to any syringe pump. It provides flexibility for various input sources such as immersion in a water tank, connection to a sample via a microfluidic tube, or direct sample dropping. By adjusting the cross-sectional areas, volumetric mixing ratios of indicator ($Q_{\text{ind}}/Q_{\text{mix}}$) and sample ($Q_{\text{s}}/Q_{\text{mix}}$) can be modified. This method ensures that the mixing ratio remains constant despite potential changes in the syringe pump's mechanical motion or microfluidic path resistances. As an additional advantage, the output solution is stored inside the pulling syringe without spilling or contamination.

Assuming the validity of laminar flow and the absence of diffusion between inlet flows, the widths of these flows in Y-channel or T-channel configurations are proportional to their flow rates. This proportionality enables easy adjustment of flow width by simply changing the syringe. Employing the correlation between the width of the hydrodynamically focused stream and the volumetric flow rates of the inlet channels enabled continuous particle separation [96]. In a separate investigation, the dimensions and placement of the nanowire arrays were adjusted tuning the inlet flow rates [97].

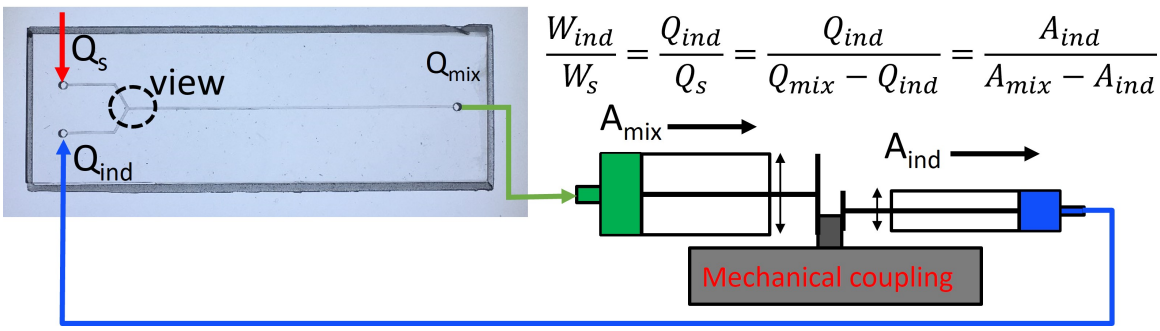

Figure 4.3. Proposed injection method with a single syringe pump.

4.2. Verification Using Y-channel Microfluidic Chip

In exploring the dynamics of the boundary interactions where two laminar flows converge, a Y-shaped junction served as the experimental setup. It is driven by a single syringe pressure pump. The microfluidic chip was constructed following the previously outlined micro-milling protocol, and external connections were established, as depicted in Figure 4.3.

During the experiments, the syringe pushing blue dye was consistently maintained at 2.5 mL with a diameter of 8.8 mm, and its flow rate was set at 1 mL/hour. To contrast, various sizes of pulling syringes filled with red dye were mechanically integrated into the system. These included syringes with diameters of 28.8 mm (50 mL), 18.5 mm (20 mL), 15.5 mm (10 mL), and 12.4 mm (5 mL), offering a range of volume capacities for experimentation.

In the Y-shaped microfluidic channel's laminar flow conditions, the distinct liquids (red and blue) remained separate at the junction by creating distinct laminar flow segments with varying widths. These widths are directly proportional to their flow rates. By optically measuring these widths within the channels, the flow ratios of the two introduced liquids can be approximately determined. Figure 4.4 presents optical microscope images (Nikon, 20x objective) showing the laminar flows of the blue and red dyes.

The corresponding measurement results of the width ratios by post-processing the captured images are presented in Figure 4.5. The observed results align closely with theoretical expectations that were calculated from the ratio of syringe diameters, with any discrepancies attributed to the measurement errors of boundary widths and syringe diameters and leakage. Despite these minor variations, the overall agreement between the observed and theoretical results confirms the efficacy of the novel method in maintaining precise mixing ratios.

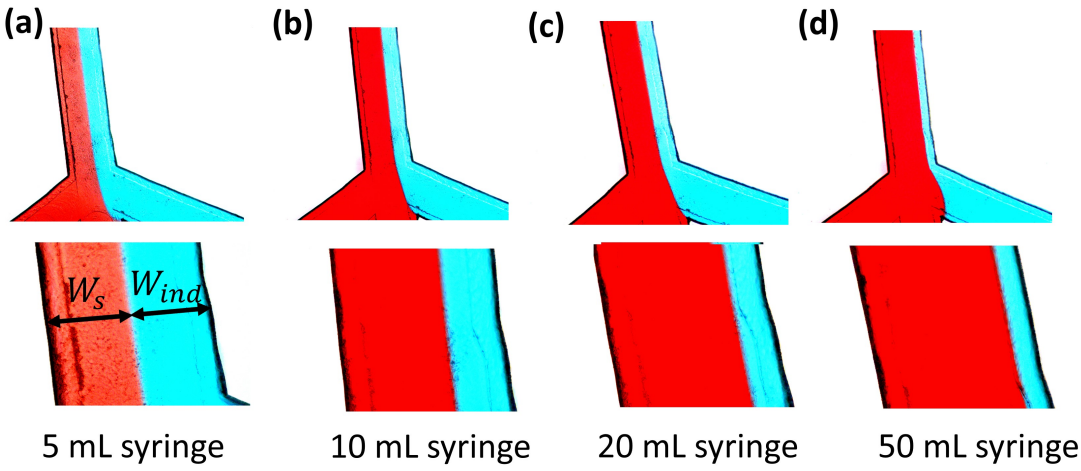

Figure 4.4. Captured images of blue and red dyed liquids inside a microfluidic channel while different sizes of pulling syringes are connected with diameters of (a) 12.4, (b) 15.5 (c) 18.5 and, (d) 28.8 mm.

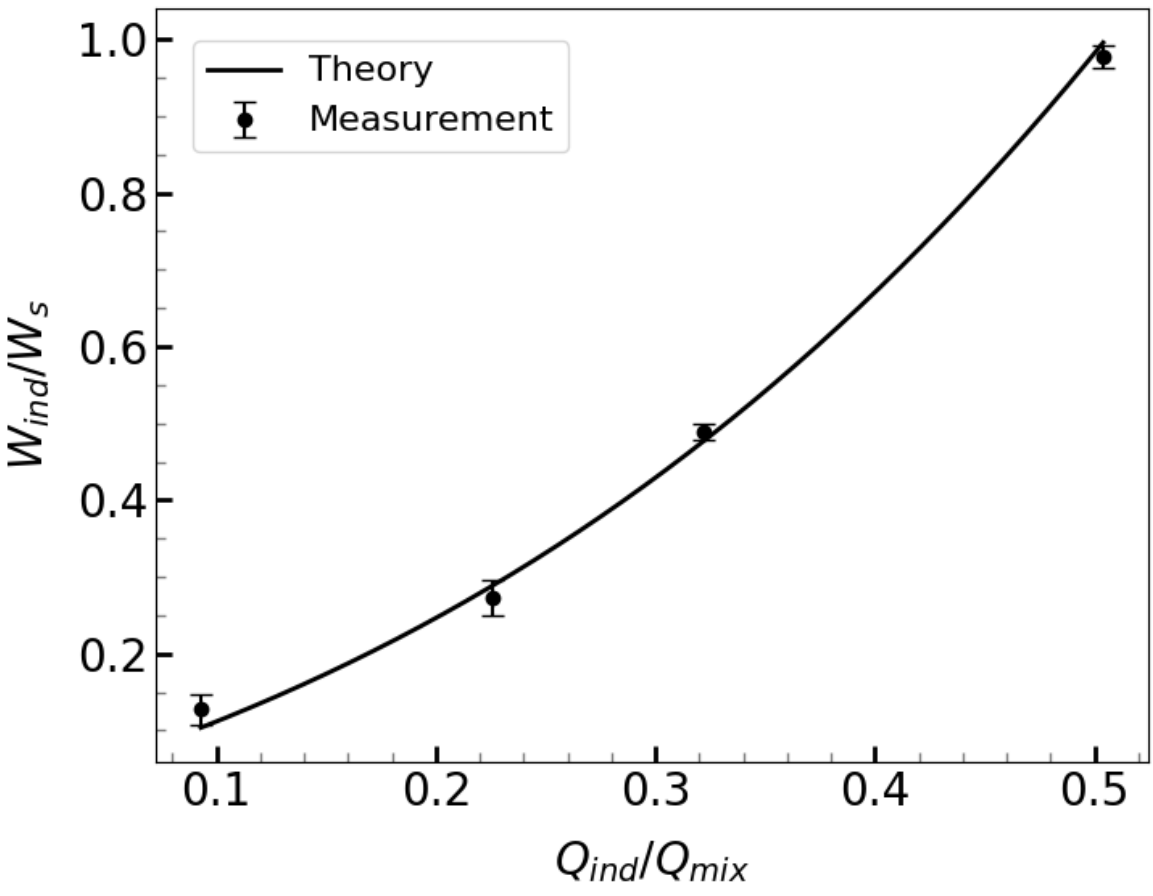

Figure 4.5. The measurement results of the width ratios of the experiment agree with the cross-sectional area ratios of the syringes.

4.3. Electric Circuit Analogy

4.3.1. Electrical Analogue

There exists a physical analogy between microfluidics and electronics as summarized in Table 4.1. In microfluidics, pressure, flow rate, and hydraulic resistance are analogous to electrical voltage, current, and resistance, respectively [98]. This analogy extends to mechanics, encompassing force, mechanical velocity, and damping [99].

The Hagen-Poiseuille law, which applies to the laminar flow of a non-compressible fluid maintained at a constant flow rate through a specific geometry, is defined as follows

$$\Delta P = R_h Q, \tag{4.1}$$

where ΔP denotes the pressure difference, R_h stands for hydrodynamic resistance, and Q represents the volumetric flow rate within the channel. Similarly, Ohm's law defines the relation between voltage difference (ΔV) and current (I) as

$$\Delta V = IR, \tag{4.2}$$

where R is electrical resistance.

In electronics, electrical capacitance represents the capacity to store an electric charge in response to a voltage change. The hydraulic compliance (capacitance) is a concept that describes the storage capacity of a microfluidic system changing its volume (V) with respect to pressure change (P) and expressed as

$$C_h = \frac{dV}{dP}. \tag{4.3}$$

The function of a flow-controlled source in microfluidics, such as syringe pumps, is analogous to that of an independent current source in electronics. In this context, the pressure drop (voltage drop) across the flow source depends on the configuration of the remaining circuit, while the flow rate (electrical current) remains constant. Conversely, a pressure-controlled source in a microfluidic system maintains a constant pressure, similar to how an independent voltage source operates in electronics. Inlet and outlet

ports that are open to atmospheric pressure in a microfluidic system can be analogously treated as a reference or 'ground' in electrical terms, similar to a zero-voltage reference point [100].

Kirchhoff's current law (KCL), which states that the total current entering any node is zero, finds an analogous counterpart in fluidic systems known as the principle of mass conservation. In fluidic mechanics, this principle dictates that the sum of flows at any node must be equal to zero. Similarly, Kirchhoff's voltage law (KVL), which asserts that the sum of voltages around a closed path is zero, can be likened to the law of energy conservation in fluid dynamics. This energy conservation law requires that the sum of pressure drops within a closed path also equals zero [101].

Table 4.1. The physical analogy between microfluidics and electronics.

Microfluidics	**Electronics**
Hagen-Poiseuille law	Ohm's law
Pressure	Voltage
Volumetric flow rate	Electrical current
Hydraulic resistance	Electrical resistance
Hydraulic compliance	Electrical capacitance
Flow-controlled source	Independent current source
Pressure-controlled source	Independent voltage source
Atmospheric pressure	Earth ground
Law of mass conservation	Kirchhoff's current law
Law of energy conservation	Kirchhoff's voltage law

These parallels between electrical and microfluidic principles serve as valuable foundations for understanding and analyzing both electrical and microfluidic systems, since it bridges the gap between these two domains of science and engineering. Electrical circuit analysis is a valuable tool for predicting flow behavior in microchannels and planning microfluidic network designs before fabrication [101].

Several studies have demonstrated the feasibility of precisely controlling volumetric flow rates within microchannel networks by adjusting the hydrodynamic resistance of these channels. The flow of the cell suspension was uniformly distributed among six channels, then subdivided into 10 branches all leading to microwells, with each channel maintaining the same flow rate due to their identical resistances [102]. Although effectiveness of electrical analysis is proven, for the detailed design of microfluidic networks, particularly in evaluating the performance of passive on-chip mixers, CFD-supported analysis may be essential [103].

Prior to developing the electrical model of the setup, it is necessary to initially establish the hydrodynamic resistance and capacitances, specifically accounting for cylindrical geometries (as in the case of tubing and syringes) and rectangular cross-sections (typical of microfluidic channels). The expression for R_t in a cylindrical tubing is [101]

$$R_t = \frac{8\eta L}{\pi r_i^4}, \tag{4.4}$$

with η symbolizing the fluid's dynamic viscosity, L the length of the pipe, and r_i the pipe's internal radius. When dealing with a rectangular microchannel, where the width w is greater than the height h, the hydrodynamic resistance is calculated by the following equation [104]

$$R_c = \frac{12\eta L}{wh^3\left(1 - 0.63\frac{h}{w}\right)}, \tag{4.5}$$

where w is the channel width, h is the channel height.

For a thin-walled cylindrical tube, the hydrodynamic capacitance can be expressed as [105]

$$C_t = \frac{2\pi r_i^2 L[(1+\nu)r_o^2 - (1-2\nu)r_i^2]}{E(r_o^2 - r_i^2)}, \tag{4.6}$$

where r_i and r_o is the inner and outer radius of the cylindrical tubing, respectively, L the length of the tube, ν is the Poisson's ratio and E is the Young modulus of the tubing material.

For a rectangular microchannel, the hydrodynamic capacitance is given by [106]

$$C_c = \frac{\alpha w h L(1+\nu)}{E}, \tag{4.7}$$

where α is a constant depending on aspect ratio and the other parameters have been previously defined.

The proposed setup can be analyzed through its electrical analogue as depicted in Figure 4.6. Syringe operations that involve pumping and withdrawing, with respective flow rates denoted as Q_{ind} and Q_{mix}, are effectively modeled by constant current sources. Ideally, the internal resistance of current sources in a syringe pump should be infinite to allow constant flow into a microfluidic chip. However, practical limitations arise due to the pump's diminished flow rate maintenance capacity under high pressures and potential clogging. These scenarios are modeled with parallel resistances R_{pump1}, R_{pump2}. Additionally, the model incorporates syringe pump capacitances, denoted as $C_{\text{pump1}}(L-X)$ and $C_{\text{pump2}}(X)$, where L represents the initial length of the filled pushing syringe, and X signifies the distance traversed during the experiments. The capacitance of the syringe is affected by the silicone o-ring surrounding the plunger and the liquid-filled cylindrical volume. The silicone o-ring, known for its flexibility, has a considerably lower Young's modulus of 1.9 MPa and a higher Poisson's ratio of 0.48. This means that the syringe's equivalent hydrodynamic capacitance is primarily influenced by the mechanical compliance of the o-ring, which changes in a linear manner with the cross-sectional area [107]. The sample reservoir in this system is analogized as a voltage source, which, given its exposure to atmospheric pressure in this application, is directly grounded. Notably, functionality of the model is maintained irrespective of the sample input pressure P_s, as the step motor suffices to withstand pressure variations.

Inlet and outlet tubings are modeled by their hydrodynamic resistances R_{inlet1}, R_{inlet2}, R_{outlet} and capacitances C_{inlet1}, C_{inlet2}, C_{outlet}. In cases of long tubes, the model adapts by halving the resistor and positioning the capacitor at the midpoint since the volume change is associated with the midpoint pressure [108]. The microfluidic chip is similarly characterized by R_{chip} and C_{chip}.

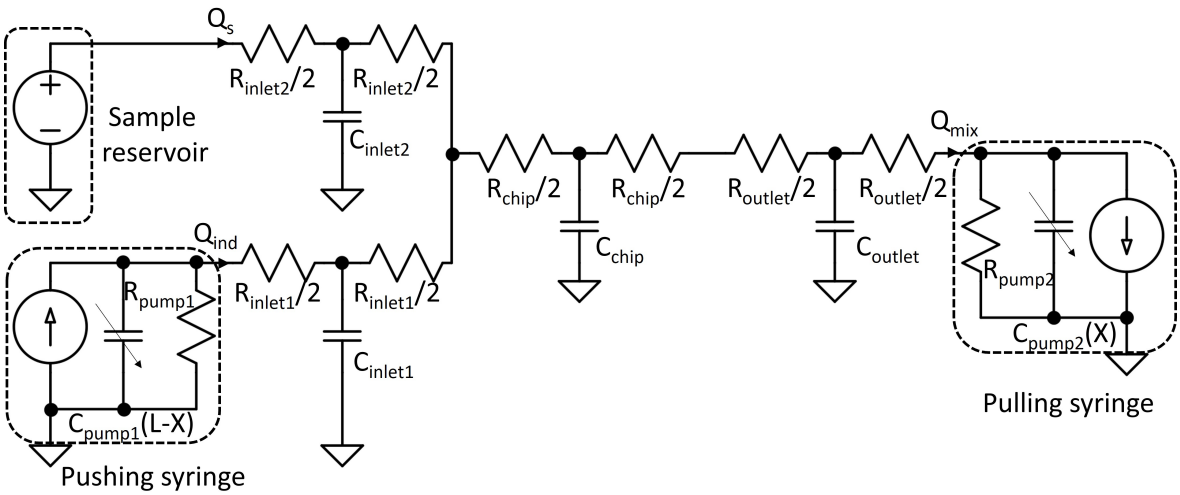

Figure 4.6. Electrical circuit representation of the experimental setup.

4.3.2. Spice Simulations and Verification

The actual dimensions of microfluidic chip is given in Section 5.7.3. The microfluidic chip, composed of PMMA, features moderate deformation characteristics with a Poisson's ratio of 0.35 and a rigidity denoted by a Young's modulus of 3 GPa. Inlet and outlet connections were established using PEEK tubes with an outer diameter of 1.59 mm and an inner diameter of 0.18 mm and 1.02 mm, respectively. To minimize dead volume and reduce potential dispersion, the size of the experimental setup was adjusted to maintain a fixed sample tubing length of 4 cm to enhance the accuracy of observations at the sample window. The use of inlet tubing in varying lengths, from 4 cm to 20 cm, facilitated the investigation of the damping effect on flow fluctuations, aiming for consistent and stable fluid flow dynamics.

The PEEK tubing connections, known for their strength and thermal stability, have a slightly higher Poisson's ratio of 0.38 and a Young's modulus of 4 GPa, indicating greater stiffness. The silicone O-ring in the syringe plunger, characterized by its flexibility, has a higher Poisson's ratio of 0.48 and a lower Young's modulus of 1.9 MPa, reflecting its extensive elasticity and adaptability in flexible applications. Lastly, dynamic viscosity of the water is used as 8.9×10^{-4} Pa s.

The stepping action of the syringe pump is emulated through the pulse width modulation (PWM) frequency of the flow signal. Specifically, for an indicator inlet flow rate of 15 µL/min using a 10 mL syringe, the advancement is calculated to be 94.3 µm/min. Consequently, this translates to the step motor advancing at a rate of 18.8 steps/min. This corresponds to the PWM frequency, when it is configured to a 1/8 microstep setting. Since the focusing point is investigating the effect of step frequency, duty cycle becomes less critical and is therefore set to half of the period.

Calculations for the hydrodynamic resistances and capacitances of the inlet, sample, and outlet tubing, as well as the syringe, were performed utilizing Equation (4.4) for resistance and Equation (4.6) for capacitance. Conversely, the hydrodynamic resistances and capacitances of the microchannel were determined using Equation (4.5) for resistance and Equation (4.7) for capacitance. Since syringe inner diameter is so large and syringe resistances are low that they may be neglected. Final equivalent circuit parameters used in the electrical simulations are given in Table 4.2. These parameters are then applied in electrical simulations. The electronic circuit simulator software LTspice (Analog Devices) is employed to analyze this electrical model.

Table 4.2. Equivalent circuit parameters used in electrical simulations.

Parameter	**Hydrodynamic resistance (Pa s/m^3)**	**Hydrodynamic capacitance (m^3/Pa)**
R_{inlet1}, C_{inlet1}	7.35×10^{12}	3.46×10^{-18}
R_{inlet2}, C_{inlet2}	1.47×10^{12}	6.92×10^{-19}
R_{outlet}, C_{outlet}	7.33×10^{9}	1.67×10^{-16}
R_{chip}, C_{chip}	2.49×10^{11}	4.11×10^{-17}
R_{pump1}, C_{pump1}	$> 10^{15}$	2×10^{-12}
R_{pump2}, C_{pump2}	$> 10^{15}$	5×10^{-12}

The effectiveness of this experimental setup is extensively demonstrated by a series of images obtained from practical experiments, complemented by corresponding

simulations. To begin with, Figure 4.7 provides insight into the impact of flow rate when no additional damping components are integrated into the system, including the syringes. At a flow rate of 15 µL/min, the flow exhibits significant oscillations. It indicates instability within the system. This clearly underscores the vital role of damping components in preventing oscillations and ensuring smoother fluid dynamics within the experimental setup.

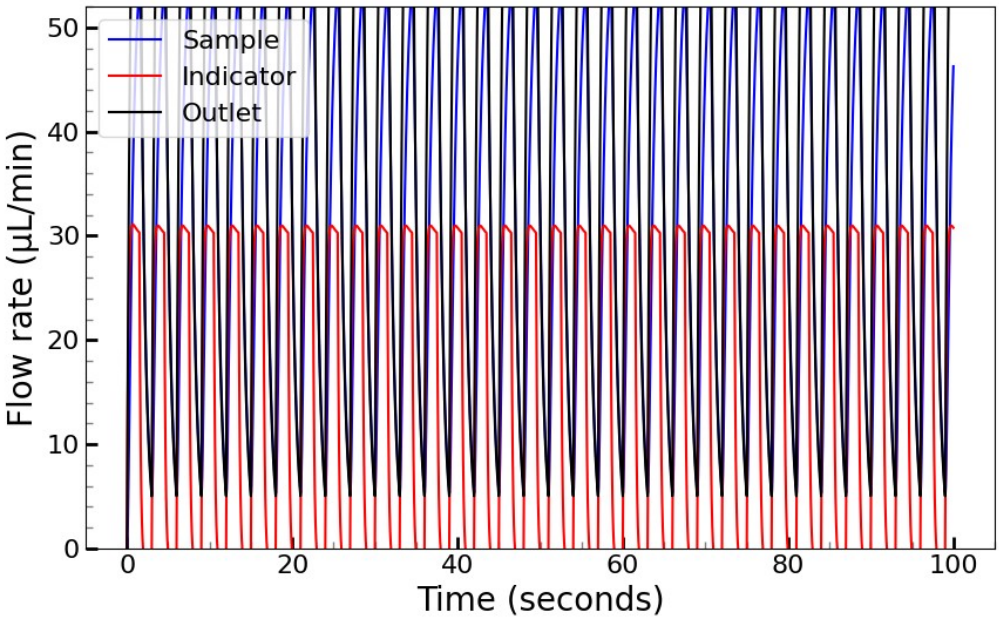

Figure 4.7. Flow oscillations at inlet boundary with low flow rate of 15 µL/min without damping effect of syringe.

Furthermore, the stability of this setup without damping elements is closely tied to the positioning of the syringe pump, due to the variability in syringe capacitance as it correlates with the syringe's fill level. This dynamic change in capacitance directly influences the damping of flow oscillations within the system. Notably, one syringe reaches its mechanical limit, resulting in significantly higher capacitance, while the other maintains minimal capacitance since it is fully empty. Therefore, it becomes evident that maintaining extended tubing lengths or integrating additional damping elements into the system may be beneficial. However, it is essential to bear in mind that augmenting tubing resistance as part of these modifications may have the unintended

consequence of slowing down the transient response. Therefore, achieving a balance point between damping and responsiveness is a key consideration in optimizing the overall system performance.

In Figure 4.8, taking into account the effect of the silicone o-ring as a damping component, particularly when the inlet tubing measures 4 cm in length, there is a clear alignment and reinforcement between the captured experimental image and simulation results. There are noteworthy fluctuations occurring at the inlet boundary. However, Figure 4.9, which adopts a longer tubing configuration of 20 cm for both the inlet and outlet, results a better scenario. Here, a side-by-side visual and simulation representation (with the image on the left and simulation on the right) reveals only minimal fluctuations at the inlet boundary. Therefore, the syringe was identified as the primary contributor to mechanical flexibility in syringe pump configurations [109].

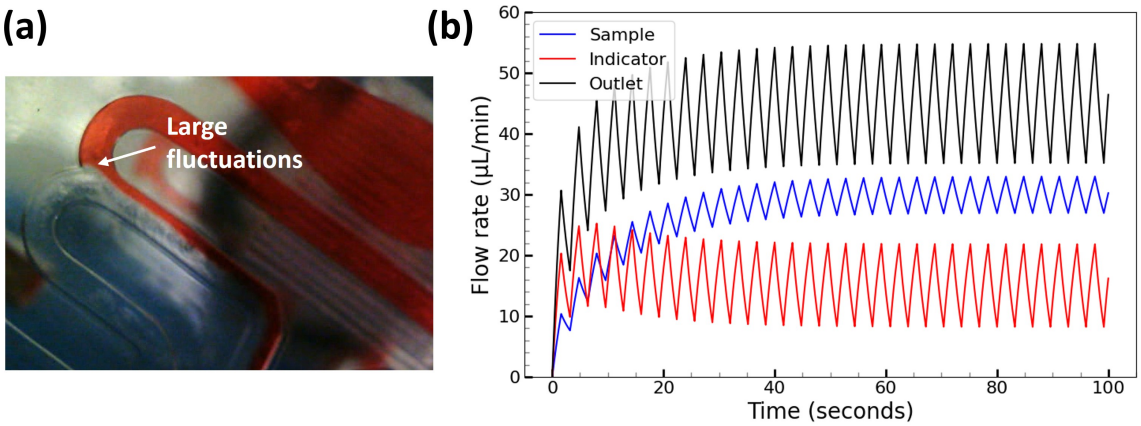

Figure 4.8. Large fluctuations at the inlet boundary with (a) image capture and (b) simulated results using 4-cm long inlet and 20-cm long outlet tubing.

This phenomenon mirrors the principles of an RC filter in electrical circuits. Longer tubing in the microfluidic system introduces greater hydrodynamic resistance and fluid volume, which together function like the resistor and capacitor in an RC filter. This arrangement dampens flow oscillations, analogous to how an RC filter smooths electrical signal fluctuations, resulting in reduced intensity of fluctuations with increased tubing length [105].

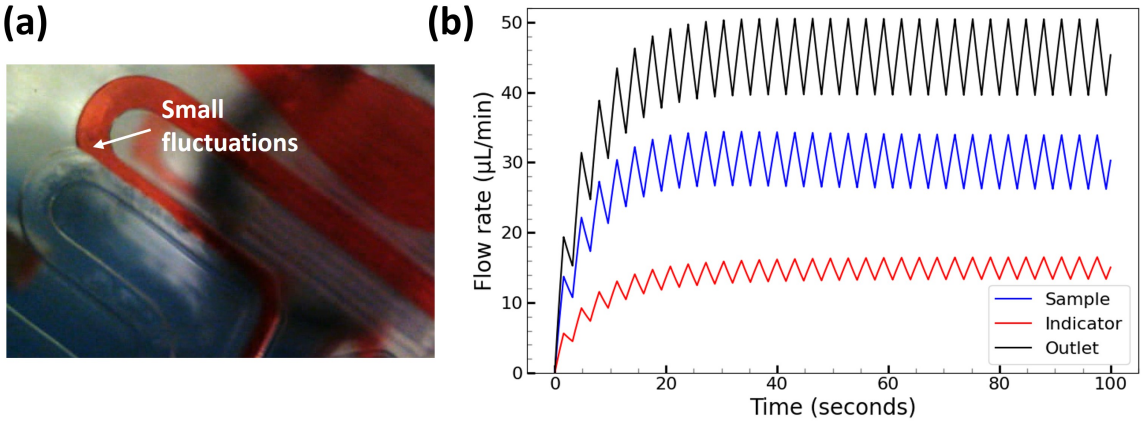

Figure 4.9. Smaller fluctuations at the inlet boundary with (a) image capture and (b) simulated results using both 20-cm long inlet and outlet tubing.

4.3.3. Improvement of Injection Setup

In microfluidic applications demanding high precision, the resolution of the syringe pump's displacement is a critical factor for accurate modeling and functionality. Stepper motors, with their intrinsic nature, execute relatively large steps based on the duty cycle of the controller unit. This process involves continuous repetition at a specific frequency, a characteristic that may not meet the stringent precision requirements. This periodic motion introduces dynamic fluctuations in the flow rates within the microfluidic channel, necessitating thorough investigation. To address this challenge, integrating a gearbox into the stepper motor becomes advantageous. This gearbox effectively reduces the step size. This allows for finer control and precision in applications where the standard step size is too large for the desired accuracy.

Specifically, a gearbox with a 100:1 ratio, as depicted in Figure 4.10, is incorporated to meet these precision demands. For the same flow rate and syringe setup, this integration allows the step motor to advance at a rate of 236 steps/min. This is a significant improvement in step frequency compared to the previous setup, while maintaining the same flow rate and syringe configuration. Correspondingly, this advancement rate equates to a PWM period of nearly 0.25 seconds, enhancing the precision of the motor's movements.

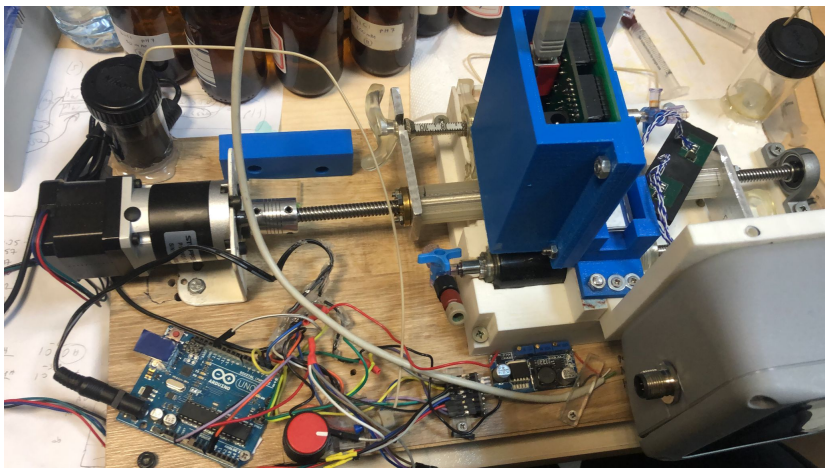

Figure 4.10. Integration of a gearbox with a 100:1 ratio.

Figure 4.11 showcases the effect of integrating a gearbox with a 100:1 ratio into the step motor. Both the captured image in Figure 4.11(a) and the simulation results Figure 4.11(b), displayed side by side, indicate an absence of fluctuations at the inlet boundary under these conditions. This observation is pivotal in highlighting the stabilizing effect of the gearbox on the flow dynamics, as it significantly reduces or eliminates fluctuations that were previously observed in shorter tubing setups or without the gearbox integration.

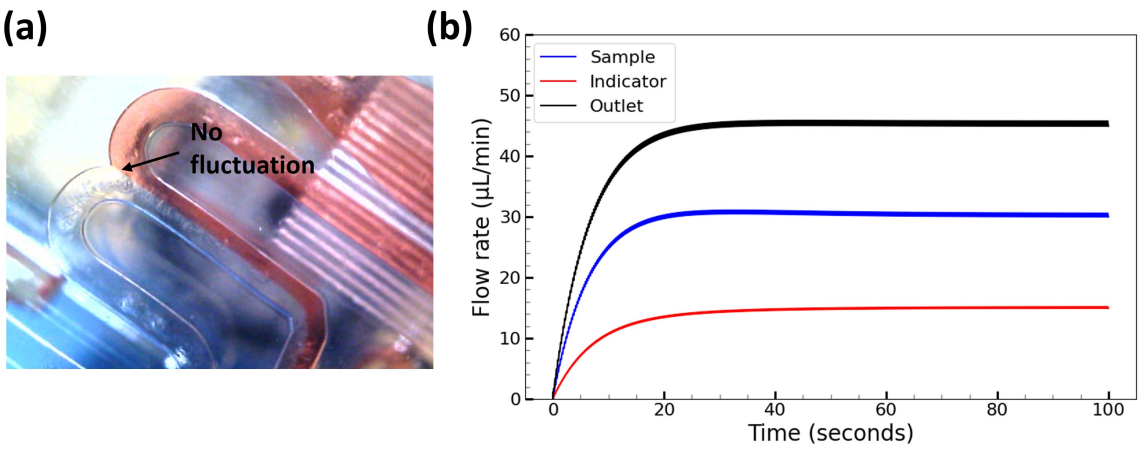

Figure 4.11. Fluctuation-free flow at the inlet boundary with after integrating gearbox (a) image capture and (b) simulated results using both 20-cm long inlet and outlet tubing.

5. DIFFERENTIAL COLORIMETRIC pH MEASUREMENT

5.1. Proposed Setup

The detailed schematic in Figure 5.1 illustrates the setup for colorimetric pH measurement using a microfluidic chip and the novel sampling injection method. The experimental setup for optical pH measurement is designed to analyze the response of sample solutions after being mixed with pH indicators. This analysis utilizes the absorbance properties of the mixed solutions by spectral color sensors.

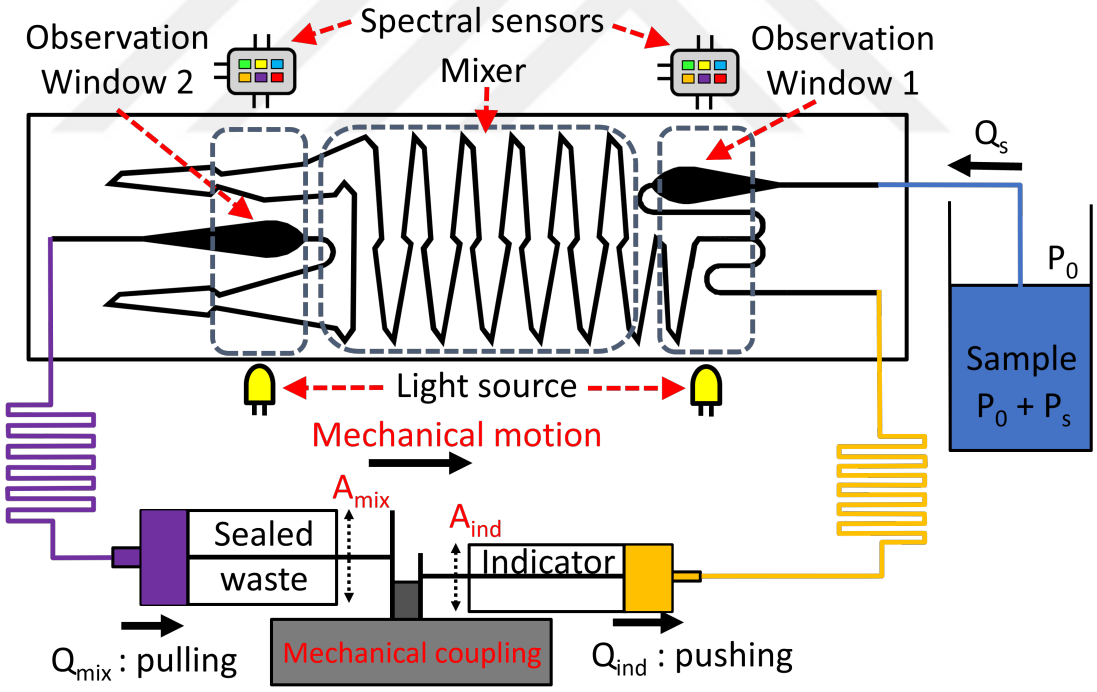

Figure 5.1. Schematic for differential colorimetric pH measurement setup.

The adaptability of the proposed sensor is further examined in scenarios where sample transparency is compromised by specific coloration and absorbance characteristics. This challenge is surmounted through the application of differential colorimetric pH measurement. This technique incorporates an additional color sensor into the

sample inlet channel. It measures the spectral response of the sample and enables differential color measurements to counteract the impact of colored samples, thus refining the accuracy of pH measurements.

In the next section of the thesis, prior to delving into the experimental presentation of the proposed sensor design, a theoretical background on optical pH measurement is presented.

5.2. Theoretical Background

The first definition of pH was introduced by Sørensen in 1909. It is based on the negative logarithm of hydrogen ion concentration and expressed as

$$\mathrm{pH} = -\log[H^+], \tag{5.1}$$

where $[H^+]$ represents the concentration of hydrogen ions in moles per liter.

Then, a more precise definition, which considers the hydrogen ion activity, is defined by

$$\mathrm{pH} = -\log a_{H^+} = -\log \gamma[H^+], \tag{5.2}$$

where a_{H^+} denotes the activity of hydrogen ions, accounting for ion interactions in solutions and γ is the activity coefficient. This representation provides a more accurate understanding of pH in complex chemical environments. As solutions become more dilute, the discrepancy between their effective and actual concentrations diminishes. This change is due to the progressively reduced significance of ionic interactions in these less concentrated solutions [110].

In an optical setup, the absorbance (A) is dimensionless and defined as the incident intensity (I_0) of light from a light source and the transmitted intensity (I_t) collected by a detector

$$A = \log_{10}\left(\frac{I_0}{I_t}\right). \tag{5.3}$$

The Beer-Lambert law states that the absorbance of a single solute is directly proportional to the concentration by

$$A = \varepsilon bc, \tag{5.4}$$

where ε is molar absorptivity, b is the path length, and c is concentration.

pH indicators are typically weak acids or bases that exhibit different colors in their protonated (H^+) and deprotonated (OH^-) forms. A general form of a pH indicator dissolved in an aqueous solution is as follows

$$\mathrm{HIn} \rightleftharpoons H^+ + \mathrm{In}^-, \tag{5.5}$$

where the indicator is in the HIn form when the solution is strongly acidic and it is in the In^- form when the solution is strongly basic. Its spectral response can be visualized as shown in Figure 5.2. Maximum absorbance values of acidic and basic forms of the indicator are at the related wavelengths of λ_1 and λ_2, respectively. Therefore, highly acidic and basic environment results to a specific color. During transition from acidic to basic, absorbance values change and spectral responses of them are added causing to mixed color.

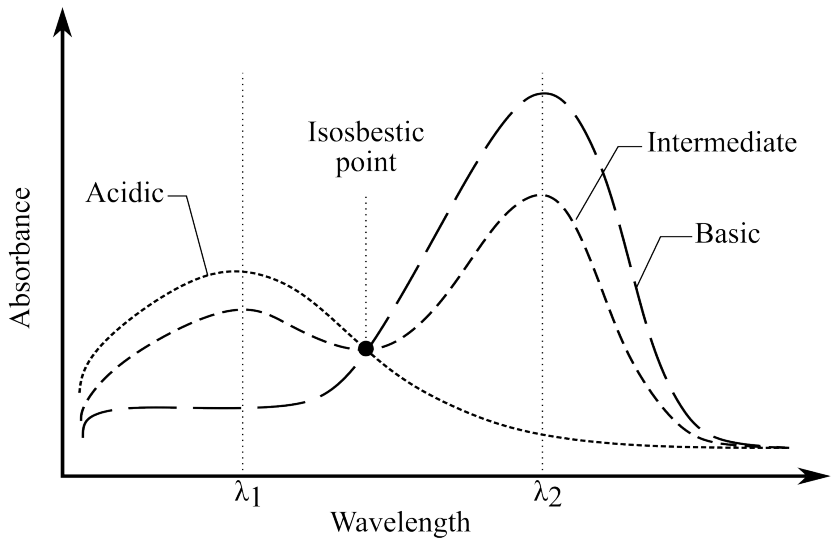

Figure 5.2. Typical spectral response of a pH indicator under pH environments of acidic, intermediate, and basic.

The acid dissociation constant, denoted as K_a, is a quantitative measure of the strength of an acid in solution. It is the equilibrium constant for the dissociation of an acid HIn into hydronium ion H^+ and its conjugate base (In^-). The K_a is defined by

$$K_a = \frac{[H^+][In^-]}{[HIn]}, \tag{5.6}$$

where the square brackets represent the molar concentration of each species at equilibrium, measured in moles per liter. Lower K_a value signifies a weaker acid, which dissociates partially whereas higher K_a value indicates a stronger acid, which dissociates completely in solution. Taking the negative logarithm of Equation (5.6)

$$-\log_{10} K_a = -\log_{10}[H^+] - \log_{10}\left(\frac{[In^-]}{[HIn]}\right), \tag{5.7}$$

and using the definition of pH, it can be rearranged, known as the Henderson-Hasselbalch equation

$$pH = pK_a + \log_{10}\left(\frac{[In^-]}{[HIn]}\right), \tag{5.8}$$

where pK_a is negative logarithm of acid dissociation constant.

The total concentration (C_T) of the indicator's both forms remains constant and equals the sum of the individual concentrations

$$C_T = [HIn] + [In^-]. \tag{5.9}$$

Assuming adherence to Beer's law, the absorbance at λ_1 is given by

$$A_{\lambda_1} = \epsilon_{HIn} b [HIn], \tag{5.10}$$

and similarly at λ_2 it is defined as

$$A_{\lambda_2} = \epsilon_{In^-} b [In^-], \tag{5.11}$$

where ϵ_{HIn} and ϵ_{In^-} is the molar absorptivity of HIn and In^-, respectively. One important assumption in these calculations is that the acidic and basic forms of the indicator do not significantly absorb light at the specific wavelength that is characteristic of the other form. This means that at λ_1, primarily the acidic form HIn absorbs light, with negligible absorption from the basic form In^-, and vice versa at λ_2.

In acidic solutions, the indicator predominantly exists in the acidic form. Thus, in such environments, $C_T = [HIn]$, and consequently

$$A_{\lambda_1,acidic} = \epsilon_{HIn} b C_T. \tag{5.12}$$

In basic solutions, the indicator is primarily in the basic form, which means $C_T = [In^-]$, and leading to

$$A_{\lambda_2,basic} = \epsilon_{In^-} b C_T. \tag{5.13}$$

Comparing the ratios of Equation (5.10) to Equation (5.12)

$$\frac{A_{\lambda_1}}{A_{\lambda_1,acidic}} = \frac{[HIn]}{C_T}, \tag{5.14}$$

and similarly dividing Equation (5.11) to Equation (5.13)

$$\frac{A_{\lambda_2}}{A_{\lambda_2,basic}} = \frac{[In^-]}{C_T}, \tag{5.15}$$

then dividing Equation (5.15) to Equation (5.14)

$$\frac{[In^-]}{[HIn]} = \frac{A_{\lambda_2} A_{\lambda_1,acidic}}{A_{\lambda_1} A_{\lambda_2,basic}}. \tag{5.16}$$

Therefore, it is feasible to find the ratio of $\left[In^-\right] / [HIn]$ for constructing a graph from colorimetric data, which are obtained at two distinct wavelengths. Taking the logarithm of Equation (5.16)

$$\log_{10} \frac{[In^-]}{[HIn]} = \log_{10} \frac{A_{\lambda_2}}{A_{\lambda_1}} + \log_{10} \frac{A_{\lambda_1,acidic}}{A_{\lambda_2,basic}}, \tag{5.17}$$

and by means of Equation (5.8)

$$pH \propto \log_{10} \frac{A_{\lambda_2}}{A_{\lambda_1}}, \tag{5.18}$$

since the second term in Equation (5.17) is constant for a specific setup.

This last equation facilitates the determination of pH from absorbance measurements, provided that the absorbance values are adjusted for background contributions. Similarly, acid dissociation constant of pH indicator may be determined using absorbance spectrum data [111, 112]. The useful pH range for significant color change in pH indicators can be obtained by considering the acid dissociation constant and extending it by plus or minus 1.5 pH units.

This adjustment compensates for the absorbance by other species in the solution at λ_1 and λ_2. When a solution comprises multiple solutes without nonlinear effects or strong bonds or interactions between them, the absorbance of each solute can be independently calculated. The total absorbance is then determined as the sum of the absorbances of all solute types. When the mixing ratio (α) is defined as the sample concentration to the mixed solution concentration for each solute and the optical path remains the same, the total absorbance at each wavelength can be found as

$$A_{\text{total}} = \sum_{i=1}^{k} A_i = \sum_{i=1}^{k} A_i^0 \alpha_i, \tag{5.19}$$

where A_i is the absorbance of each solute and A_i^0 is the absorbance of each solute before mixing them. Therefore, Equation (5.18) can be modified for this application

$$pH \propto \log_{10} \left(\frac{A_{\text{total}}(\lambda_2) - \sum_{i=1}^{k} A_i^0(\lambda_2)\alpha_i}{A_{\text{total}}(\lambda_1) - \sum_{i=1}^{k} A_i^0(\lambda_1)\alpha_i} \right), \tag{5.20}$$

where $A_{total}(\lambda_1)$ and $A_{total}(\lambda_2)$ are absorbance values of acidic and basic forms of the indicator at the related wavelengths of λ_1 and λ_2, respectively.

5.3. Experimental Methodology

Reagents like buffer solutions of varying pH values, chloroform, and ethanol were sourced from Sigma-Aldrich. Phenol red and universal indicator used as pH indicators were procured from ChemBio Laboratory. To ensure purity, all aqueous solutions were prepared using deionized water from a TKA GenPure ultrapure water system.

For off-chip experiments, an Ocean Optics USB2000 spectrometer was employed to validate the absorbance spectrum of pH indicators and food dye solutions. Measurements were conducted in 10 mm cuvettes, with OceanView 2.0 software. It provides data acquisition and controlling of experimental parameters. A Mikropack DT-MINI-2-GS served as the light source.

A range of sample pH solutions was prepared and loaded into the sample reservoir. The accuracy of these solutions was confirmed using a HI-1131B glass body pH

electrode and a HI-5522 research-grade pH bench meter from Hanna Instruments. Calibration was performed using pH 4, 7, and 10 buffer solutions. The pH indicator was administered using a 10 mL pushing syringe, while extraction was performed with a 20 mL syringe that is mechanically linked. Inlet and outlet tubes were horizontally inserted into the microfluidic chip through the 1.6 mm deep grooves etched along the chip's edge and sealed with epoxy, ensuring smooth integration and fluid flow.

As the light source in the setup of on-chip experiments, white LEDs from Wurth Electronics were chosen for their 6000K correlated color temperature (CCT) and a color rendering index (CRI) of 85. Light detection was conducted using the AS7262 spectral sensor by ams-OSRAM AG, chosen for their six-channel multispectral sensing capabilities within the visible region. Each channel of the AS7262 sensor is characterized by a Gaussian filter with a full width at half maximum spectral bandwidth of 40 nm. To fully leverage the 16-bit resolution of analog-to-digital converters in the spectral sensors, gain and integration time settings were calibrated to ensure optimal channel readings when filled with DI water [15]. Spectral sensor readings were carefully characterized for temperature changes to ensure accurate compensation. Before measurements, LEDs were allowed to warm for at least 30 minutes to stabilize light intensity.

The measurement system was built around the STM32H743VIT6 microprocessor from STMicroelectronics. It comprises three distinct printed circuit boards (PCBs) as depicted in Figure 5.3: the mainboard, the LCD board, and a board dedicated to color sensors. The mainboard houses power and control circuits, the LCD board drives the display, and the third board interfaces with the color sensors. All PCBs were designed using the Proteus Design Suite by Labcenter.

Configuration of the microprocessor's peripherals and pin assignments were done by the STM32CubeMX tool. It aids in setting up complex software elements like the microprocessor and thin-film transistor (TFT) LCD driver, as well as coordinating peripheral units.

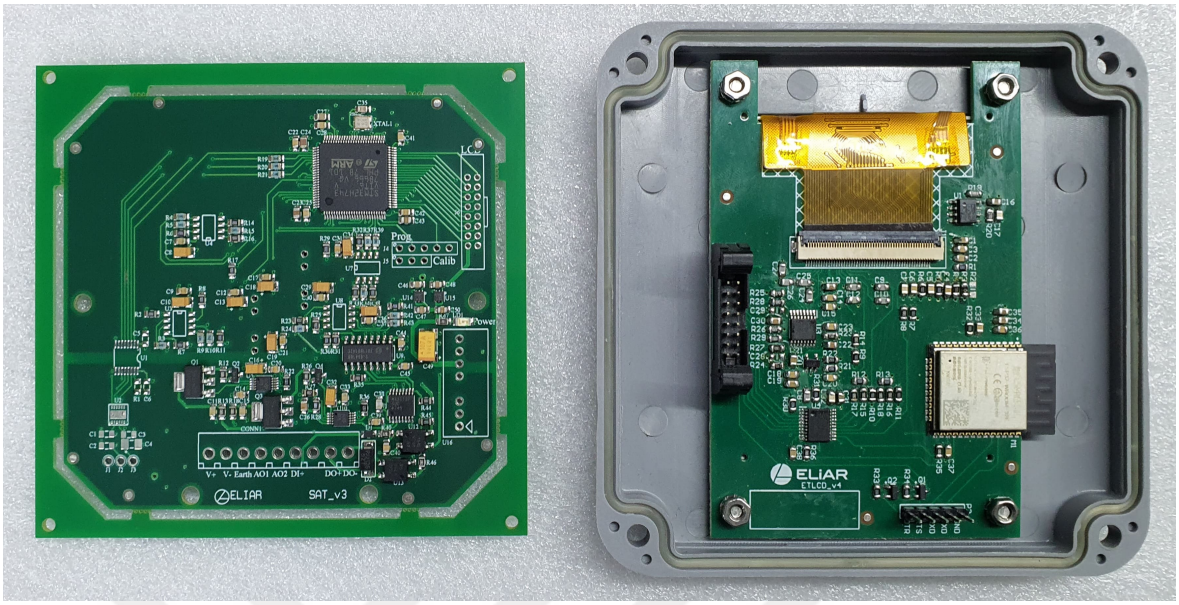

Figure 5.3. Electronic boards designed and used in data acquisition.

In the development of the system's software infrastructure, a real-time operating system (RTOS), specifically FreeRTOS, was implemented for efficient management and organization. Software development was completed using STM32CubeIDE, which allowed for adjustments like protocol and clock settings, and automatically generated startup code.

A central part of the software operational flow was the measurement task. It is responsible for communicating with color sensors via the universal asynchronous receiver-transmitter (UART) protocol. To enhance measurement precision, the gain and integration time parameters of the sensors were fine-tuned through an automatic calibration procedure using DI water as a reference. This expanded the measurement range of the sensors to capture a wide spectrum of data.

Data presentation and analysis were provided via a graphical user interface (GUI). It was designed using the graphic software framework TouchGFX. Communication with TFT-LCD display was achieved via the serial peripheral interface (SPI). The GUI, as shown in Figure 5.4, was designed for real-time observation and analysis of the experimental data.

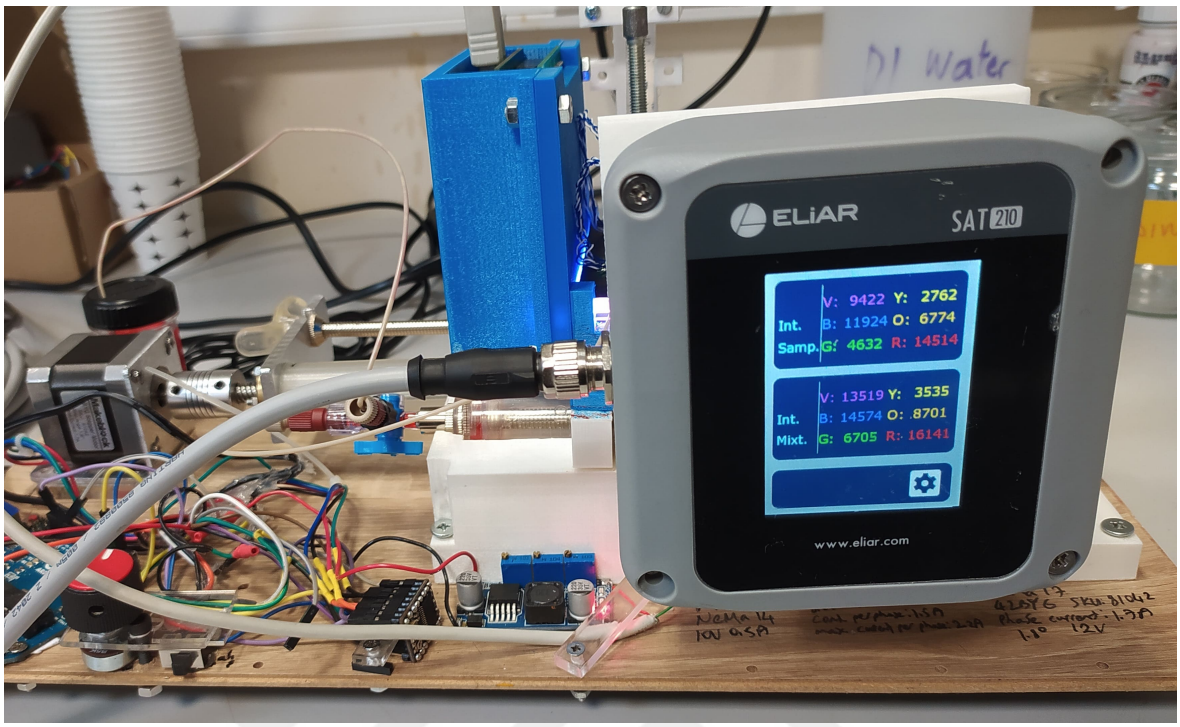

Figure 5.4. Graphical user interface designed for observing actual data.

5.4. Preliminary Off-chip Experiments

Preliminary off-chip experiments were conducted to validate the feasibility of this setup, employing a spectrophotometer and a standard light source. Measurements were taken in 10 mm cuvettes, capturing the absorbance spectrum of the samples. As a pH indicator, phenol red was selected. Phenol red shows peak responses at 433 nm and 557 nm and is sensitive to pH levels ranging from 6 to 8.5 [34]. The change in color signifies the shift in pH levels: under acidic conditions, phenol red appears yellow, and as the environment becomes increasingly alkaline, it transitions to red and eventually to magenta.

The investigation started with the spectral response of buffer solutions containing phenol red between pH 6 and 8, exploring the optimal sample-to-indicator mixture ratio. At higher concentrations of the indicator, the color transition becomes less distinct because the absorption curves of the two indicator colors overlap more significantly, leading to a reduced sensitivity in the color change as given in Figure 5.5.

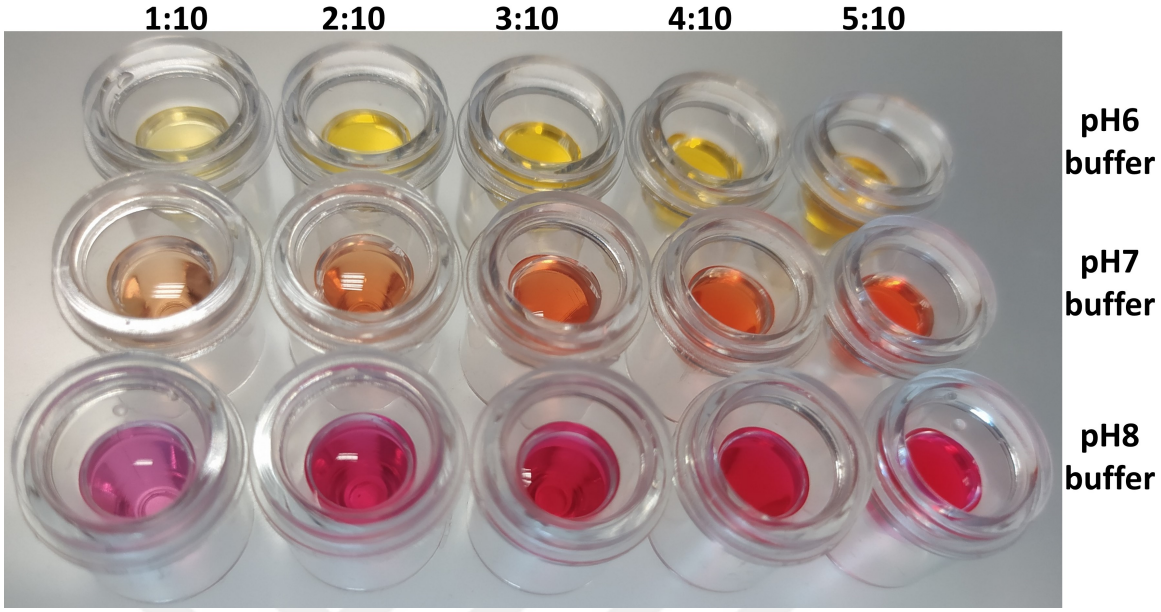

Figure 5.5. Samples prepared at varying mixing ratios, ranging from 1:10 to 5:10 (indicator to overall volume), within a pH range of 6 to 8.

Through experimental investigations, it was concluded that an overall volume-to-indicator ratio of 40:1 yielded the most effective results. Higher absorbance values (greater than 1) were observed to degrade the linearity of Beer's Lambert law. Conversely, a lower concentration of the pH indicator reduces sensitivity due to minimal absorbance change with variations in pH. In other words, a decrease in the concentration of the indicator resulted in a less pronounced response to changes in pH levels. This optimized ratio of of 40:1 resulted to reliable data within a pH range of 6 to 8, as presented in Figure 5.6.

Focusing on the pronounced absorbance shift at 560 nm with increasing pH levels, Figure 5.7 was generated. This graph, plotting absorbance against pH at 560 nm, enables pH estimation of unknown samples, assuming consistent path length, using a fourth-order polynomial given by

$$y = 0.02612x^4 - 0.6069x^3 + 5.345x^2 - 21.07x + 31.27, \tag{5.21}$$

where y is the absorbance, and x is the pH value. With blind samples, estimated pH error is limited to ± 0.1 pH units.

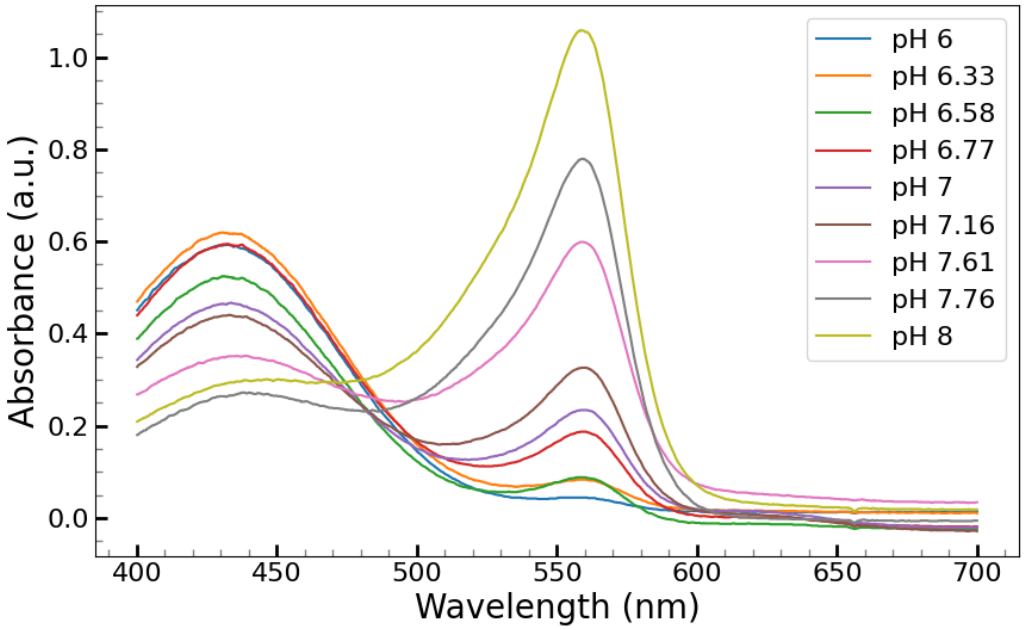

Figure 5.6. Spectral response of buffer solutions with phenol red at a 40:1 mixing ratio for pH 6 and pH 8, conducted in 10 mm cuvettes.

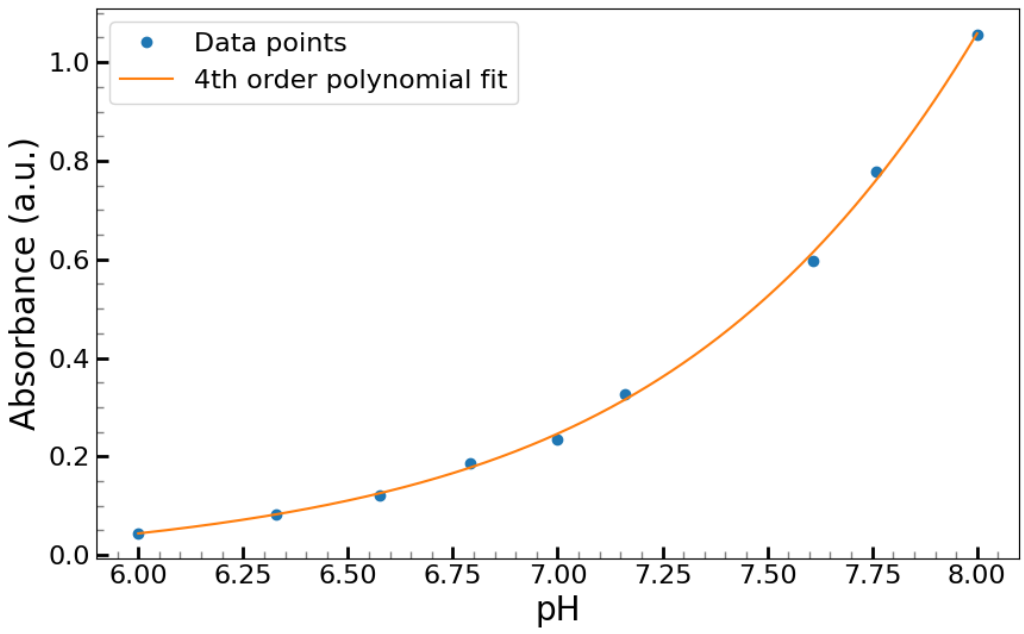

Figure 5.7. Absorbance measurements of buffer solutions at 560 nm with phenol red at a 40:1 mixing ratio for pH 6 and pH 8, conducted in 10 mm cuvettes.

Subsequent testing involved colored samples prepared with food dyes. The pH was confirmed before and after dye addition, revealing no significant change attributable to the dye itself. Upon introducing the phenol red indicator and recording the absorbance values, the absorbance change resulted from the pH indicator response was calculated. The data exhibited that, despite the influence of color from the dyes, the pH could be estimated with reasonable accuracy using the polynomial relationship.

Table 5.1 encapsulates the experimental outcomes, including the minimal errors between predicted and actual pH values for samples with red, green, blue and orange food dyes, maintaining an error margin within ±0.09 pH units.

Table 5.1. Off-chip optical pH measurement of colored liquids for various food dyes.

Food Dye	**Sample pH**	**Sample Abs.**	**Mixed Abs.**	**Difference Abs.**	**Estimated pH**	**Error pH**
Red	6.61	0.159	0.260	0.101	6.52	-0.09
Red	7.02	0.560	0.823	0.263	7.07	0.05
Red	7.65	0.204	0.890	0.686	7.70	0.05
Red	7.88	0.156	0.995	0.839	7.84	-0.04
Blue	7.11	0.160	0.410	0.250	7.04	-0.07
Blue	7.34	0.137	0.595	0.458	7.43	0.09
Blue	7.51	0.095	0.690	0.595	7.60	0.09
Green	6.75	0.060	0.216	0.156	6.76	0.01
Green	6.87	0.080	0.282	0.202	6.91	0.04
Green	7.24	0.084	0.464	0.380	7.31	0.07
Green	7.38	0.088	0.568	0.480	7.46	0.08
Orange	7.70	0.044	0.755	0.711	7.72	0.02
Orange	6.61	0.071	0.190	0.119	6.61	0
Orange	7.38	0.073	0.529	0.456	7.43	0.05
Orange	6.46	0.033	0.122	0.089	6.45	-0.01

Understanding the interaction between light and colored samples is needed for interpreting the effects on absorbance measurements within the context of sensor performance. The absorption of specific wavelengths by a colored object, under white light illumination, results in the perceived color being the complementary to the absorbed wavelengths. This optical principle is applied when assessing the impact of food dyes on absorbance readings. For example, the presence of red food dye has a pronounced effect on the absorbance at 560 nm due to its high absorption of light in this region. It causes a large change in the measured values.

As demonstrated by the experimental data, despite the potential effects of variations of samples on its absorbance, the proposed differential colorimetric pH measurement approach has been effective in compensating for them. These preliminary findings pave the way for the next stage of research. Implementing this technique in a microfluidic system with automated sampling is expected to improve both the practicality and accuracy of pH measurements in complex, real-world applications.

5.5. Development and Validation of the Microfluidic Mixer

5.5.1. Design and Simulation

The critical aspect of ensuring effective mixing in microfluidic systems is a fundamental requirement for the accurate and repeatable measurement of pH. One inherent challenge in microfluidic mixers arises from the laminar flow profile within small-sized channels. These channels are characterized by low Reynolds numbers, a condition that prevents turbulence, thereby resulting in molecular diffusion being the primary mode of mixing. However, this form of diffusion is inherently slow on such a scale by necessitating the adoption of methods to augment mixing efficiency.

Active micromixing techniques, employing external forces through devices like alternating magnetic fields, surface acoustic waves, thermal actuation, and electroosmotic flow, have been explored for their ability to enhance mixing [113–116]. Despite

their effectiveness, these methods have the disadvantages of complex fabrication processes, power dissipation and reagent compatibility requirement [117].

Given these challenges, passive mixers emerge as the preferred choice. These devices, known for their simplicity, low power requirements, and ease of integration into microfluidic systems, present an efficient and practical solution to the mixing problem. They can be categorized based on their specially designed structures, such as serpentine or gear-shaped configurations, as well as obstacle-based structures [118].

The chaotic advection-based staggered herringbone mixer introduces grooves on channel walls to create counter-rotating vortices by enhancing mixing through chaotic flow patterns [119–121]. Lamination-type mixers improve interfacial area by altering channel cross-sections, utilizing splitting and recombining of flows to increase contact surfaces between streams [122]. The Tesla structure uses looped channels to facilitate flow separation and recombination for effective mixing [123]. Convergent-divergent mixers employ alternating channel sections to create variations in flow velocity, leading to improved mixing through fluid compression and expansion [124].

With the objective of simplifying microfluidic chip fabrication, a specialized passive mixer design has been developed and validated. Complete microfluidic chip for optical pH measurement is designed as shown in Figure 5.8. It is composed of a Y-channel with two inlet ports to introduce the sample and the pH indicator, a passive micro-mixer within an elongated folded microfluidic channel, an observation window for the LED light to pass through and collected by the six-wavelength color sensor and an outlet port.

For clarity in subsequent simulations and experimental analyses, the micromixer is depicted with clearly numbered passages and elbows, providing a detailed view of its layout. Additionally, specific cutline coordinates are marked for reference. Cutline 1 is positioned in Passage 3, while Cutline 2 is located just before the observation window of the mixture.

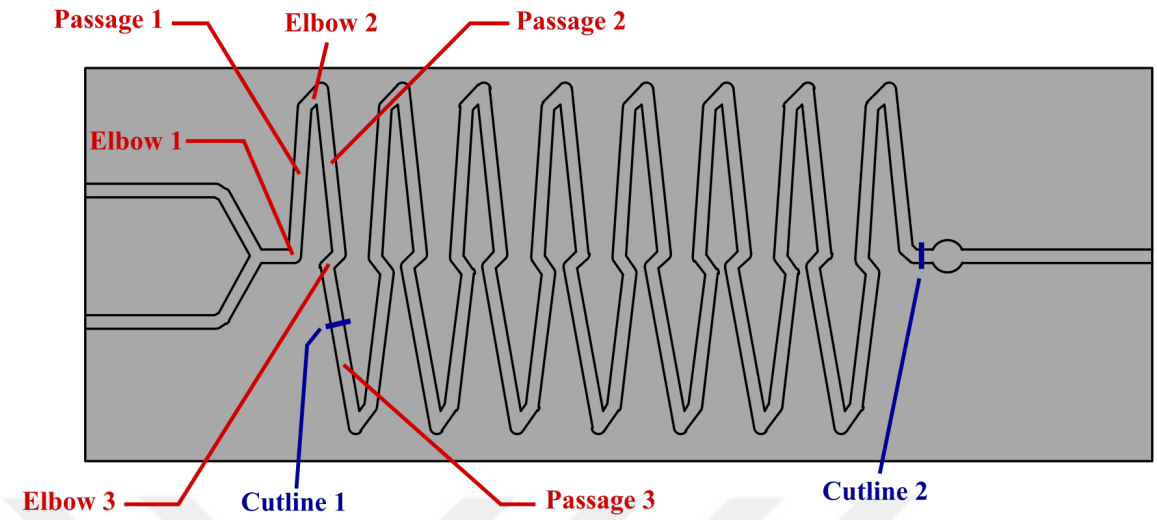

Figure 5.8. Design of the microfluidic chip featuring a micro-mixer with numbered passages and elbows, alongside the cutlines indicated for simulation purposes.

The effectiveness of the micromixer design was evaluated through CFD simulations performed in COMSOL Multiphysics (version 5.5). The 3D design of the chip was transferred to the COMSOL interface as device geometry. Utilizing the Microfluidics Module and Fluid Flow interface, simulations employed the Laminar flow and Transport of Diluted Species physics interfaces.

In these simulations, inlet streams, modeled with pure water, were varied in flow rates from 1 mL/h to 20 mL/h, with fluid properties set to match water at 20 °C (density of 1000 kg/m^3 and viscosity of 1 mPa s). The diffusion coefficient was set to 1×10^{-9} m^2/s.

Given the micro-milling technique constraints, the channel width was fixed at 800 µm. Initially, the effect of channel height was explored, ranging from 100 µm to 500 µm. Figure 5.9 and Figure 5.10 illustrates the concentration distribution throughout the channel width in Cutline 1 and Cutline 2, respectively. Notably, a channel height of 100 µm did not yield complete mixing, even in Cutline 2. As a precautionary measure, a final channel height of 300 µm was chosen to ensure thorough mixing throughout the channel.

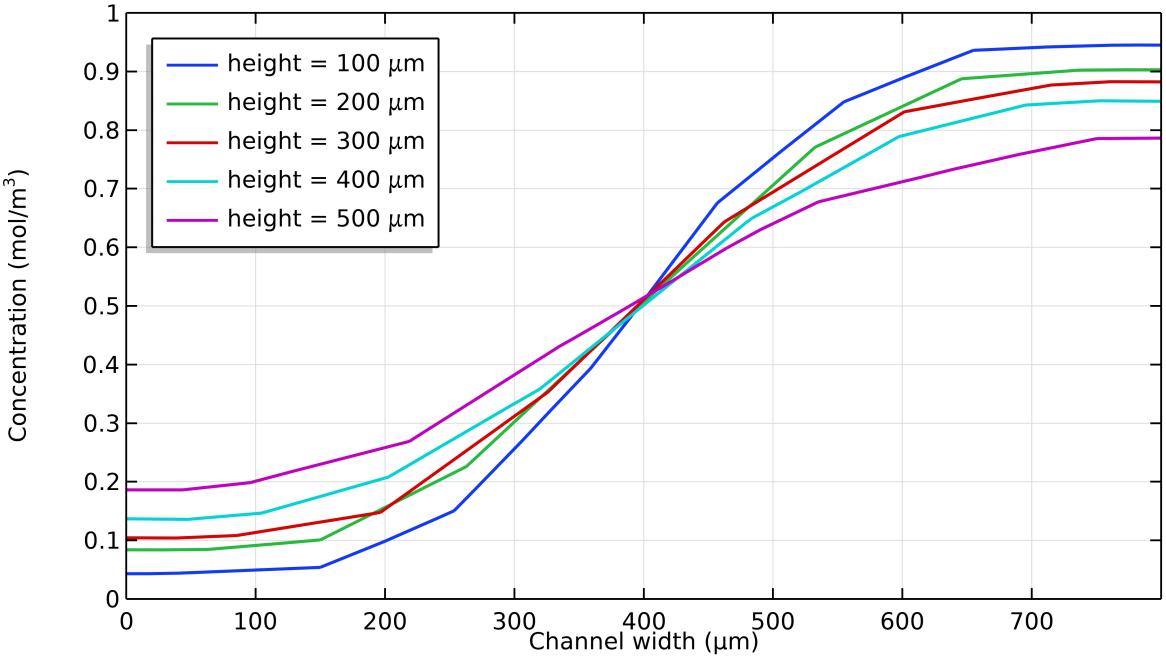

Figure 5.9. Concentration distribution in microfluidic mixer at Cutline 1, illustrating the effects of varying channel depth for inlet flow rate of 1 mL/h.

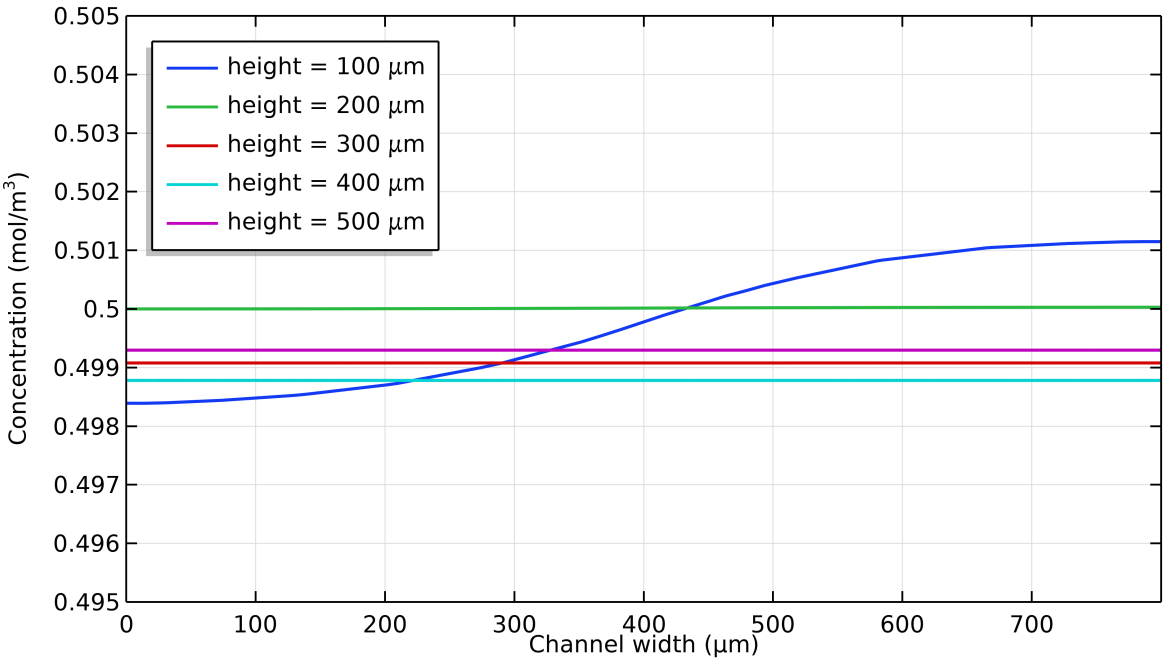

Figure 5.10. Concentration distribution in microfluidic mixer at Cutline 2, illustrating the effects of varying channel depth for inlet flow rate of 1 mL/h.

After determining the channel height, the impact of different flow rates was analyzed. This allowed for the examination of dye concentration profiles at various sections of the device. Figure 5.11 displays the concentration map inside the microfluidic mixer for an inlet flow rate of 1 mL/h, and Figure 5.12 for an inlet flow rate of 20 mL/h.

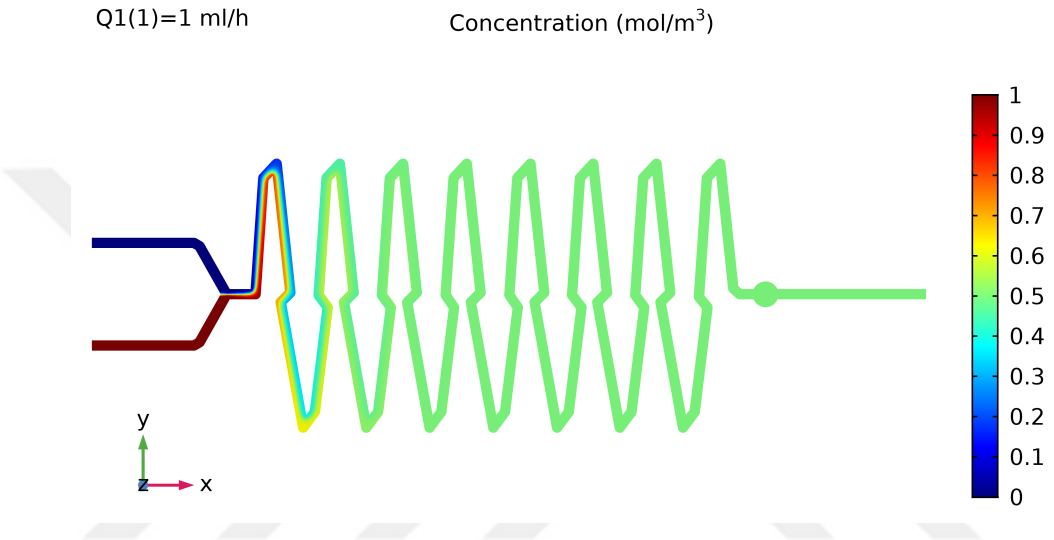

Figure 5.11. Concentration map inside the microfluidic mixer for the inlet flow rate of 1 mL/h.

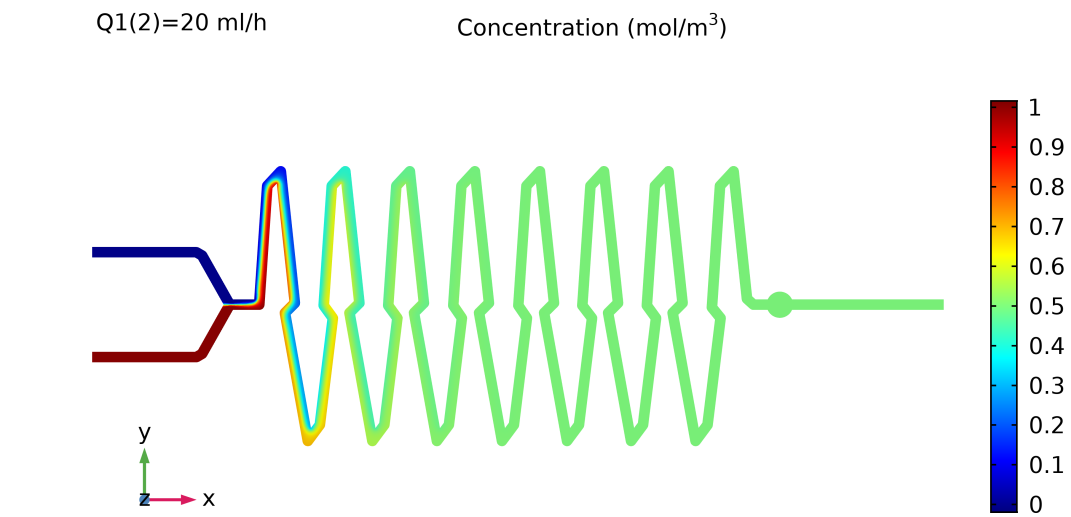

Figure 5.12. Concentration map inside the microfluidic mixer for the inlet flow rate of 20 mL/h.

Upon comparing the simulation results, a clear trend emerges. As the flow rate increases, the point of complete mixing shifts further downstream. Specifically, a thorough examination before reaching the observation window reveals that even at higher flow rates, mixing is comprehensively completed.

For a more profound understanding, Figure 5.13 and Figure 5.14 provide a visual representation of the concentration gradient across the channel width at Cutline 1 and Cutline 2 for two distinct flow rates, respectively. Significantly, at a low flow rate, mixing exhibits a higher degree at Cutline 1. It is primarily influenced by the dominance of diffusion. However, at both high and low flow rates, complete mixing is clearly attained at Cutline 2, attributable to the centrifugal forces generated at the elbows. These simulations prove the microfluidic mixer's mixing efficacy by demonstrating its applicability across various flow rates, while the distinct behaviors at Cutline 1 and Cutline 2 offer insights into dynamic processes affecting concentration gradients in diverse flow conditions.

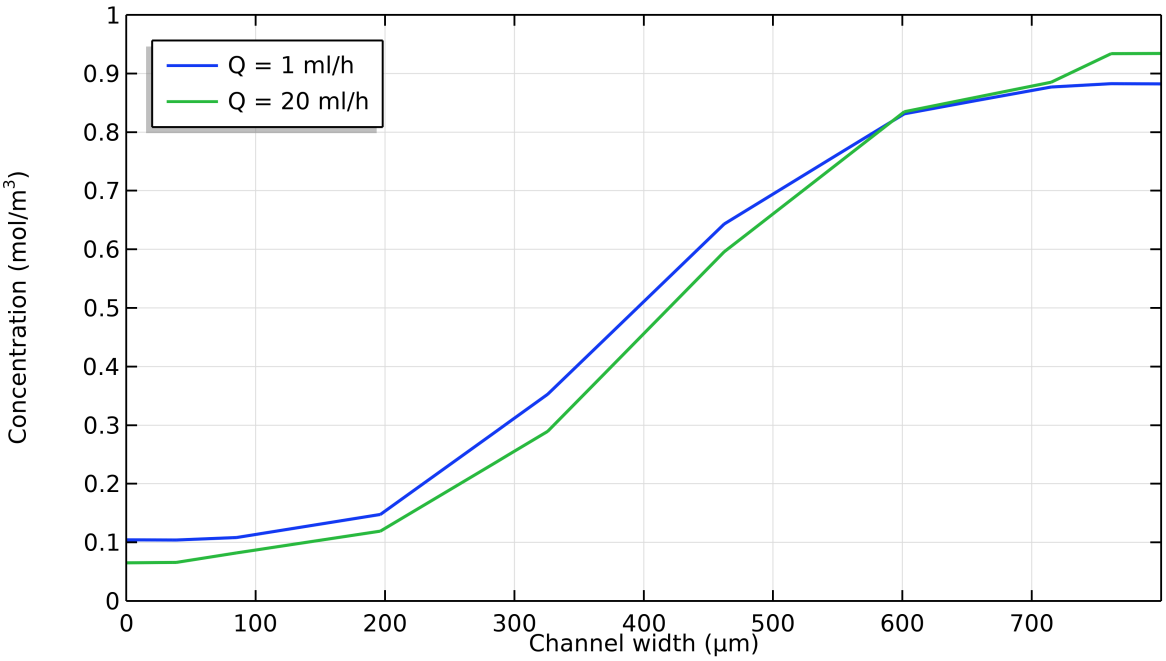

Figure 5.13. Concentration distribution in microfluidic mixer at Cutline 1 that illustrates the effects of varying inlet flow rates at 1 mL/h and 20 mL/h.

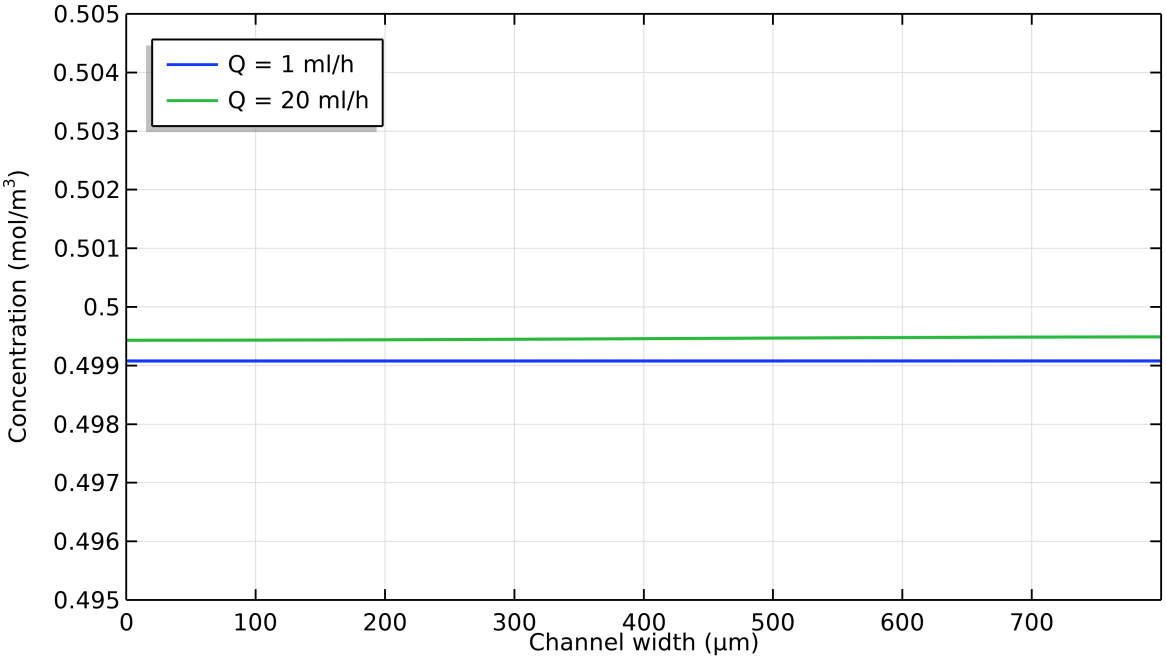

Figure 5.14. Concentration distribution in microfluidic mixer at Cutline 2, illustrating complete mixing despite varying inlet flow rates at 1 mL/h and 20 mL/h.

5.5.2. Experimental Verification

The microfluidic chip was fabricated using the micro-milling method, as detailed in Section 2.3.2. The primary goal was to assess the chip's mixing performance, comparing it with the outcomes of simulations. To achieve this, blue and red dyed liquids were introduced into the chip at varying flow rates using the proposed injection method. The focus was on observing whether these liquids achieve full mixing under these conditions.

There is a strong correlation between flow rate and mixing efficiency as demonstrated by our experimental data as given by Figure 5.15. At a lower flow rate of 1 mL/h, efficient mixing was achieved near the end of Passage 3, just before the fourth elbow. This enhanced mixing at reduced speeds can be attributed to the increased interaction time and diffusion effects predominant in laminar flow regimes. Increasing the flow rate to 5 mL/h shifted the point of complete mixing towards the middle of Passage 6, suggesting a slight reduction in mixing efficiency likely due to shorter

diffusion times and more streamlined flow. Significantly, at a higher flow rate of 10 mL/h, the mixing point was further delayed to the beginning of Passage 8. This trend highlights the influence of stronger laminar flow characteristics, which tend to maintain fluid layers and impede mixing. The most marked effect was observed at the highest flow rate of 20 mL/h, where the mixing point was located in the middle of Passage 11, indicating a substantial decrease in mixing efficiency. This observation underscores the critical influence of flow rate in passive microfluidic systems, revealing that higher flow rates, while beneficial for throughput, can adversely impact mixing efficiency by reinforcing laminar flow patterns.

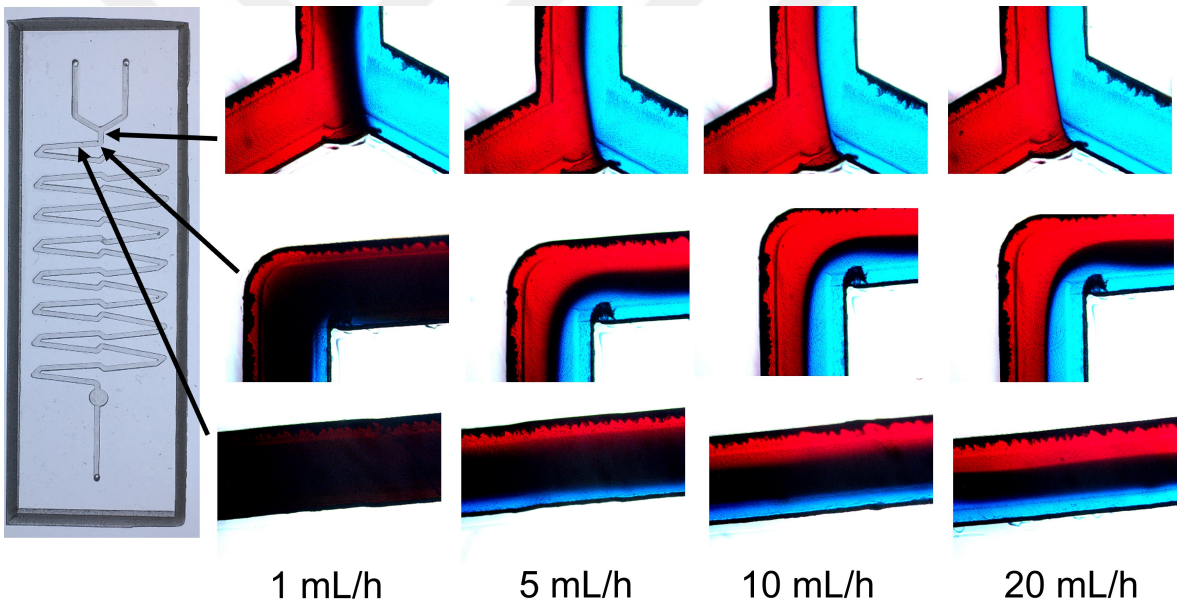

Figure 5.15. Mixing efficiency for varying inlet flow rates.

5.6. pH Measurement of Transparent Liquids

The injection-withdrawal method simplifies the mixing of liquids in precise, sustained volumetric ratios, unaffected by inlet pressure, using a single pump action. Next, it was effectively applied for continuous colorimetric pH measurements within a microfluidic chip. The entire setup for optical pH measurement includes a white LED and a spectral sensor positioned across the observation window of the microfluidic

chip, as illustrated in Figure 5.16(a). Figure 5.16(b) demonstrates a closer look at the microfluidic chip.

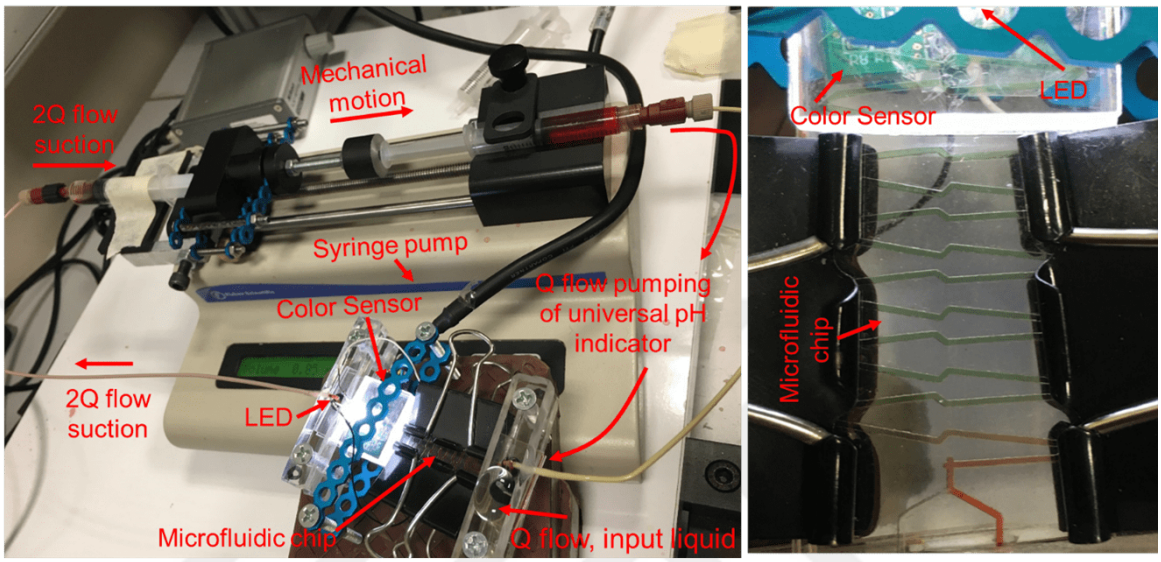

Figure 5.16. Optical pH measurement using a microfluidic channel with a modified syringe pump (a) whole experimental setup (b) microfluidic chip.

5.6.1. Phenol Red

The results from the color sensor, as displayed in Figure 5.17, confirm the efficacy of the setup in measuring pH values. These results were smoothed using quadratic interpolation across discrete data points at wavelengths of 450, 500, 550, 570, 600, and 650 nm. In the figure, the isosbestic point of the pH indicator is clearly remarkable, corresponding to pH changes from 6 to 8. This setup's successful measurement of pH values in samples supports the reliability and precision of the employed method. Plotting the logarithm of the absorbance ratios at 550 and 450 nm, as presented in Figure 5.18, establishes a direct correlation between the calculated results and the pH value. The graph exhibits a clear linear response, although the results tend to deviate from linearity at extreme pH values.

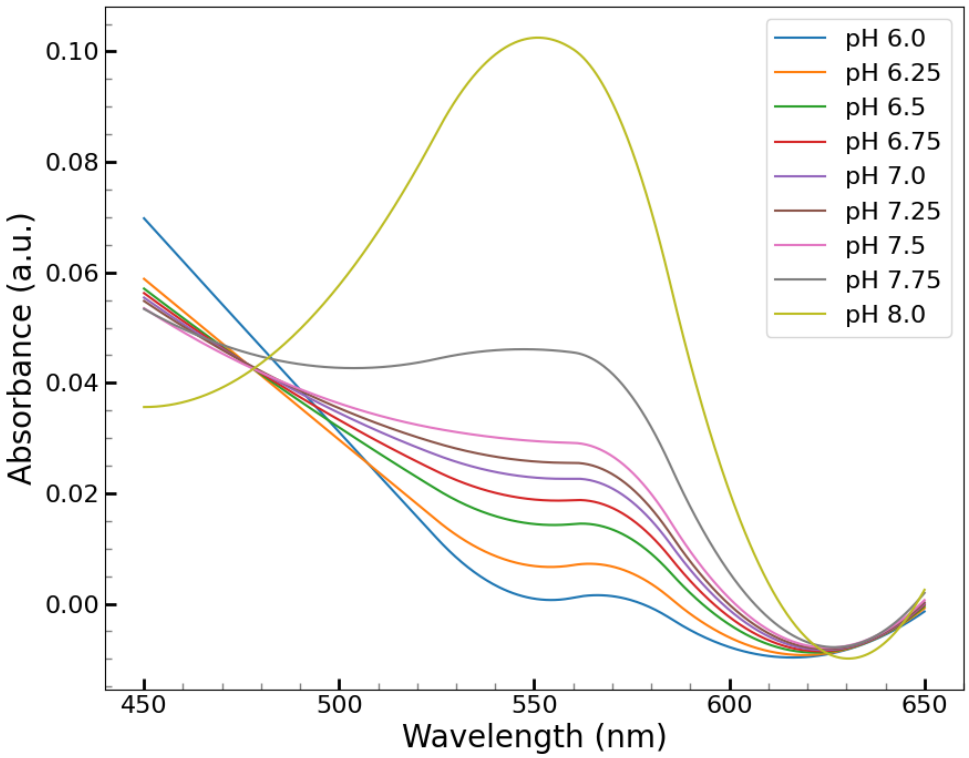

Figure 5.17. Absorbance measurements of the phenol red pH indicator between pH 6 and pH 8 in steps of 0.25.

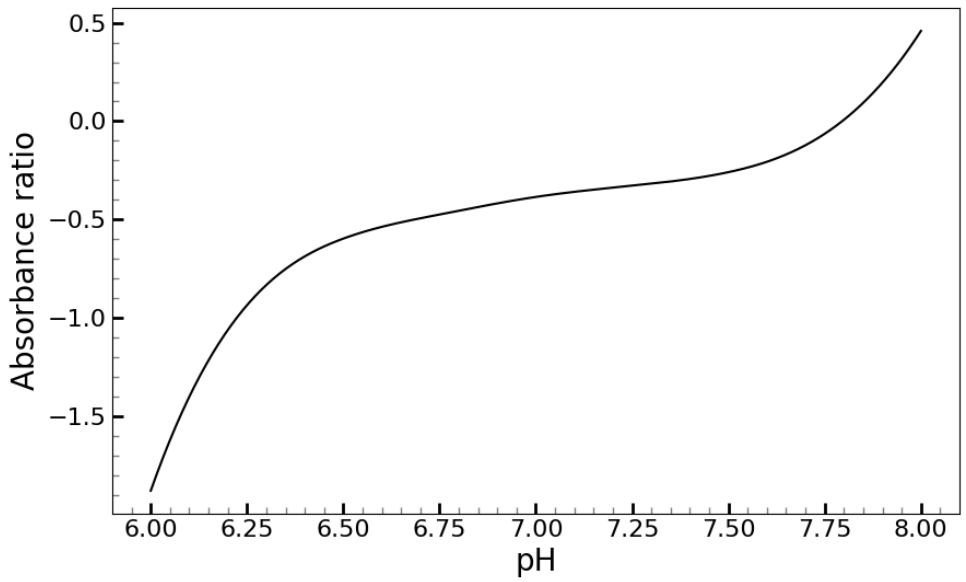

Figure 5.18. Logarithm of the absorbance ratios at wavelengths of 550 and 450 nm versus input pH values.

5.6.2. Universal Indicator

Given the limited pH measurement range of phenol red, the scope can be expanded through the incorporation of different indicators. A universal pH indicator solution comprises thymol blue, methyl red, bromothymol blue, and phenolphthalein. It facilitates covering a broad pH spectrum from 1 to 14. Specifically, thymol blue indicates pH changes between 1.2 and 2.8, methyl red transitions around pH 4.4 to 6.2, bromothymol blue operates within the 6.0 to 7.6 range, and phenolphthalein is effective from pH 8 to 10 [33].

In the concluding experiment, this universal indicator was evaluated over the entire pH range. The outcomes, depicted in Figure 5.19, successfully demonstrate how each individual indicator responds to varying pH levels, with these responses clearly annotated on the graph.

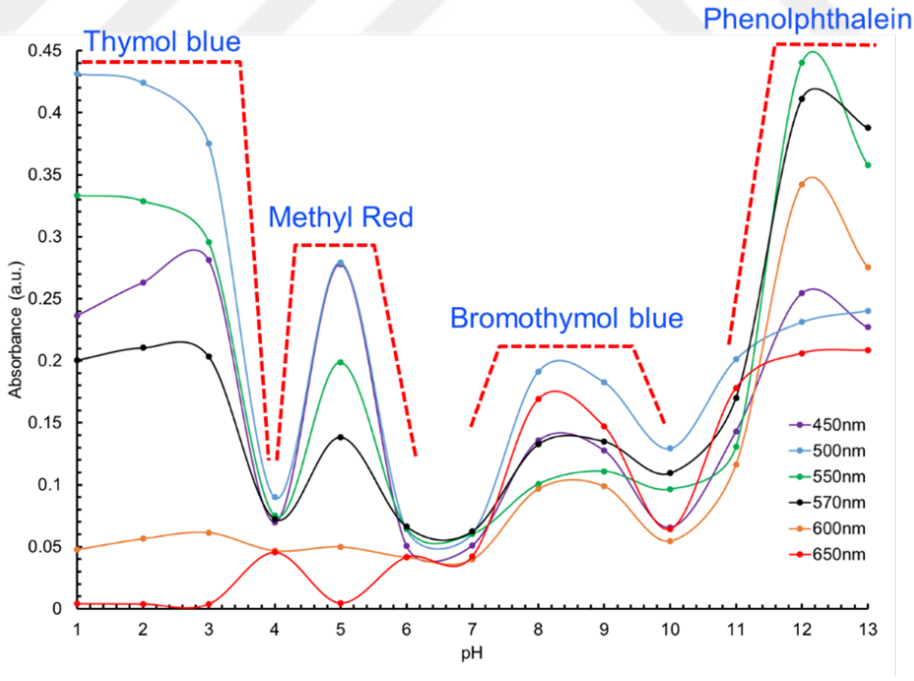

Figure 5.19. Experimental results of the optical pH measurement with universal indicator consisting of thymol blue, methyl red, bromothymol blue and phenolphthalein.

5.7. Fabrication of the Automated Platform

5.7.1. Optical Sensing Setup

The optical setup for differential colorimetric pH measurement is depicted in Figure 5.20. These LEDs are powered by a constant-current source and positioned on the thinner edge of the microfluidic chip. This arrangement allows for the internal reflection of light rays within the chip. These light rays are directed to escape through engraved grid lines that are precisely aligned with the observation windows and spectral sensors. This figure illustrates the comprehensive optical arrangement used for the differential colorimetric analysis of pH levels, including the positioning of LED light source, observation windows and multiple color sensors along with the path of light transmission, within the microfluidic system.

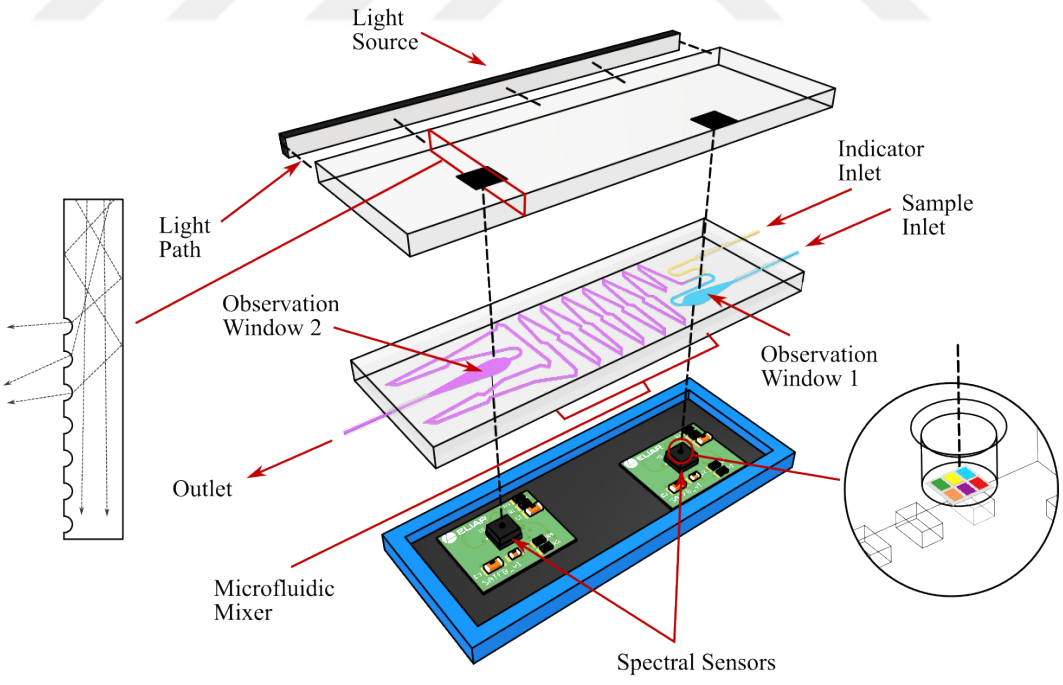

Figure 5.20. Exploded view of optical measurement setup in detail.

Light guiding plate and white LEDs are coupled through the horizontal edge of the chip, as shown in Figure 5.21.

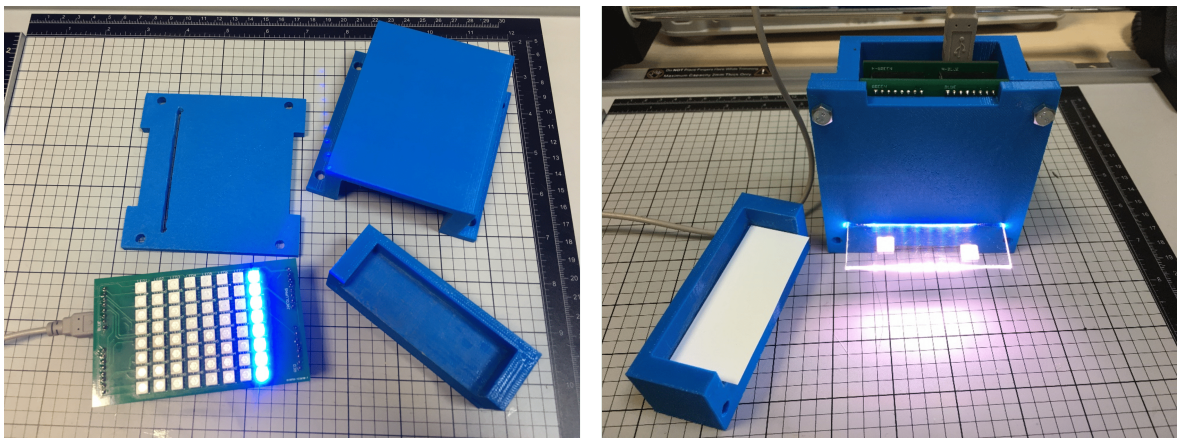

Figure 5.21. White LEDs coupled across the observation windows of the chip.

5.7.2. Revision of Syringe Pump Design for Push-Pull Operation

The syringe pump was adapted into a push-pull configuration to consolidate the entire setup within a compact body. The pH indicator is delivered using a 10 mL pushing syringe, while the extraction is carried out with a mechanically linked 20 mL syringe. Both syringes are mounted as illustrated in Figure 5.22.

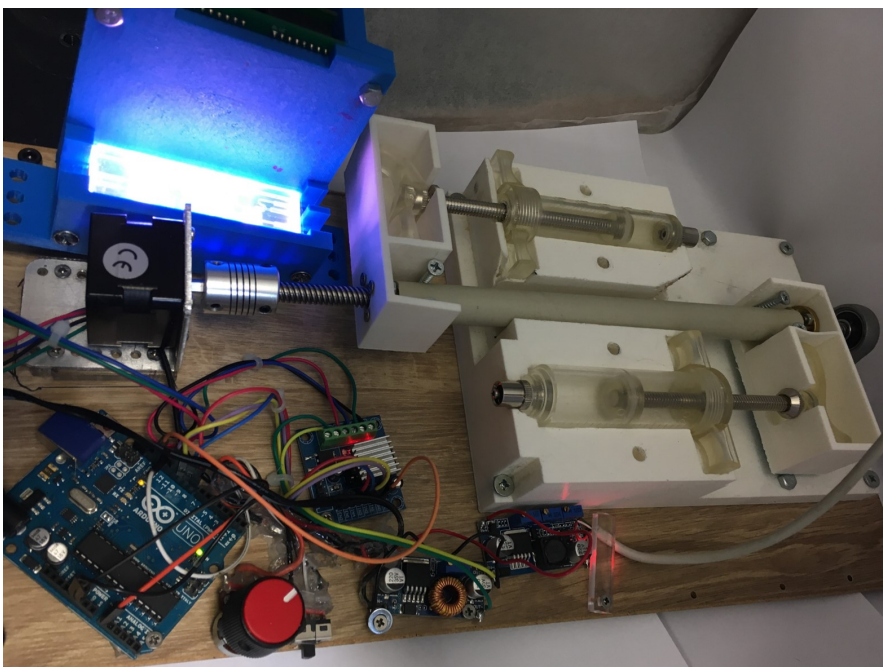

Figure 5.22. Custom-designed syringe pump and syringe assembly.

5.7.3. Modification of Microfluidic Mixer Chip

The subsequent step focuses on evaluating the novel injections method's to consistently mix liquids in precise ratios. A microfluidic chip specifically for differential colorimetric pH measurement, is designed and constructed as illustrated in Figure 5.23. This chip features an additional sample observation window with same dimensions. Mixer length is longer than previous one. Observation windows are smoothed out to prevent air bubble trapping. Inlet and outlet reservoirs have a volume of 6 µL.

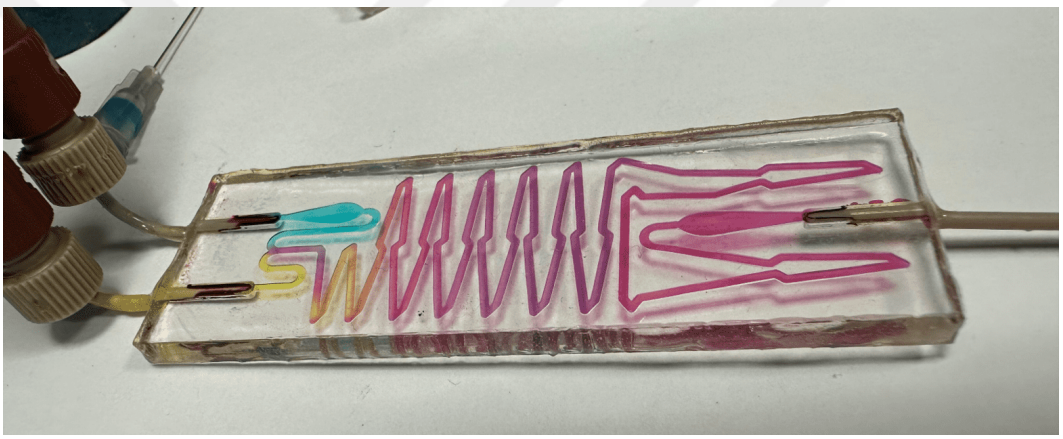

Figure 5.23. The microfluidic chip fabricated for optical pH measurements in colored liquids.

COMSOL simulations were repeated to assess mixing efficiency, as depicted in Figure 5.24, and the results validated the absence of changes in mixer efficiency for the inlet flow rate of 1 mL/h.

5.7.4. Optical Analysis of Mixer Performance

The complete optical system, as previously described, along with their corresponding electronic power and control circuit boards and the microfluidic chip, were assembled over the pumping assembly. The tubing connections are shown in Figure 5.25. Lastly, optical sensors were precisely aligned with the chip's measurement windows, depicted in Figure 5.26.

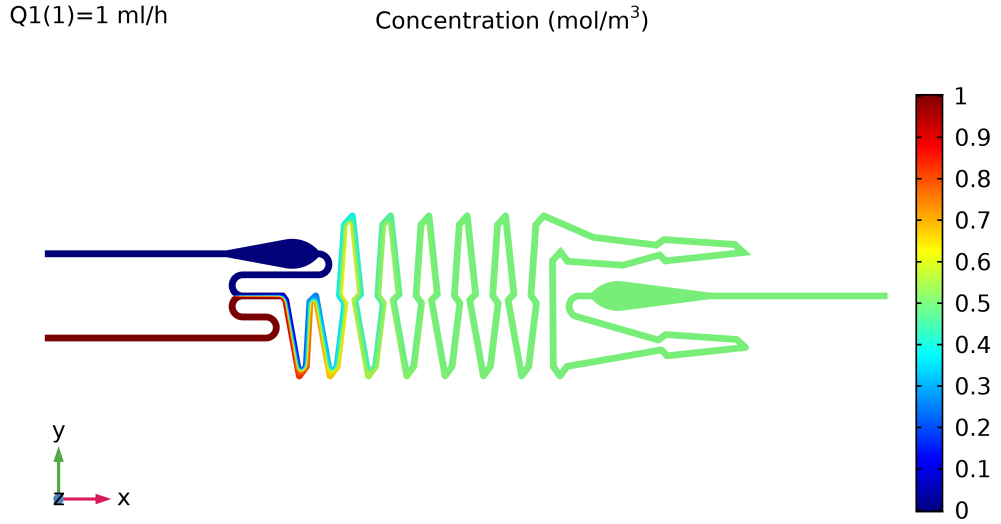

Figure 5.24. Concentration map inside the microfluidic mixer for the inlet flow rate of 1 mL/h.

To facilitate the loading of the syringe with the indicator and the drainage of outlet syringes during experiments, two-way valves have been integrated into the inlet and outlet tubing systems. This addition enhances the control of fluid handling in the experimental setup.

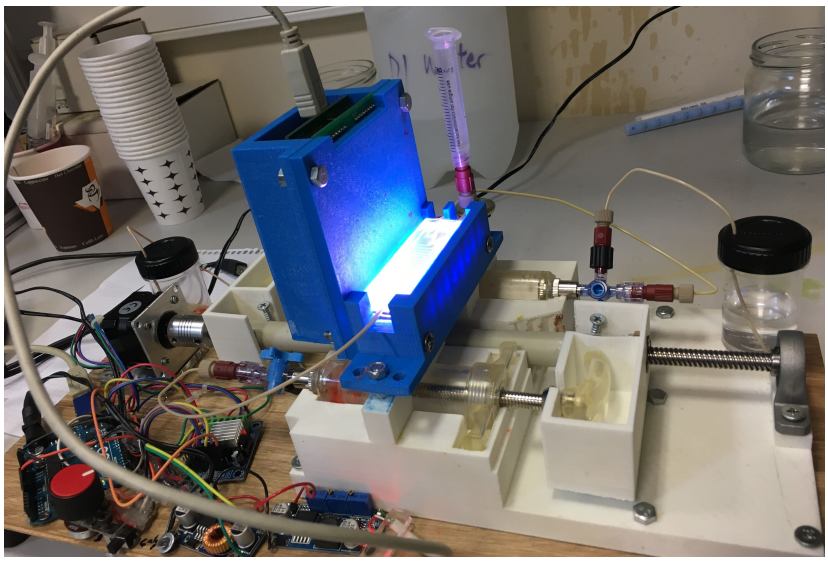

Figure 5.25. Experimental setup for differential colorimetric pH measurement using a microfluidic channel.

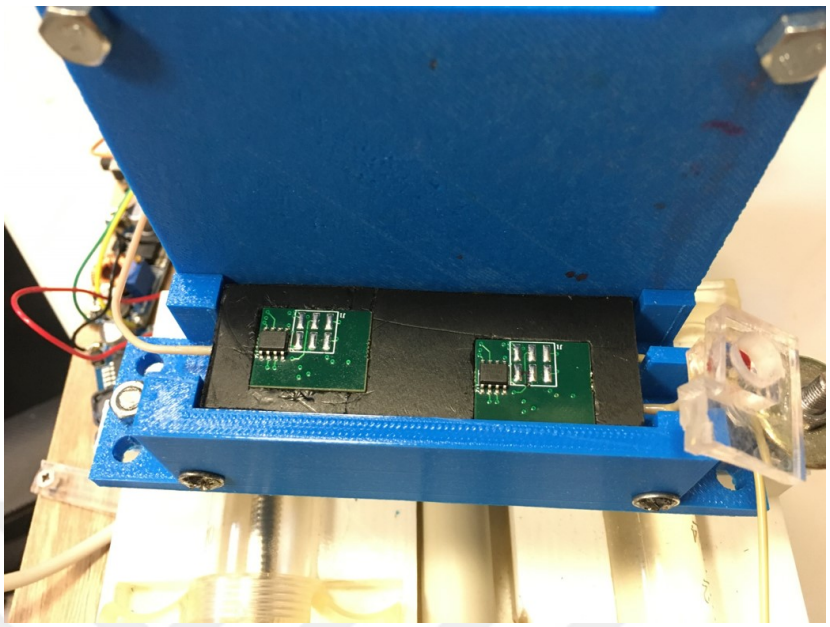

Figure 5.26. Optical sensors aligned with the chip's measurement windows.

Beer-Lambert law allows for the evaluation of mixing efficiency based on absorbance measurements. The experiment involves measuring the absorbance of a red dye solution and its mixture with DI water, specifically at a wavelength of 450 nm. DI water was introduced at a flow rate of 15 µL/min through the pH indicator port of the microfluidic chip. Concurrently, red food color dye at various concentrations 150 to 450 µL/L was introduced at the sample port. They were carefully diluted from a master sample. The color sensor readings were recorded for both the undiluted sample and the resulting mixture.

To ensure proper and thorough mixing, the time for sample and pH indicator solutions to reach the observation window passing through the mixer should be longer than the time needed for diffusive mixing. Also, it is important to disregard the transient flow effect that occurs when the sample is initially introduced into the system. Given that the total volume of the mixture is 104 µL and the indicator flow rate is set at 15 µL/min, in each experiment involving a change of sample, data recording was initiated only after the system has been operational for 5 minutes. This ensures steady-state flow, critical for reliable and repeatable data on mixing efficiency. Between each sample change, the chip was thoroughly flushed with DI water to guarantee the

complete removal of any residual substances by maintaining the reliability of subsequent experiments.

The optical image presented in Figure 5.27(a) validates the transition from a laminar flow state to a homogeneously mixed solution. Focusing on the Y-channel and the outlet observation window of the mixing microchannel illustrates the achievement of the complete mixing process. Figure 5.27(b) displays the absorbance measurements both before and after the mixing procedure, which are derived from the recorded sensor values.

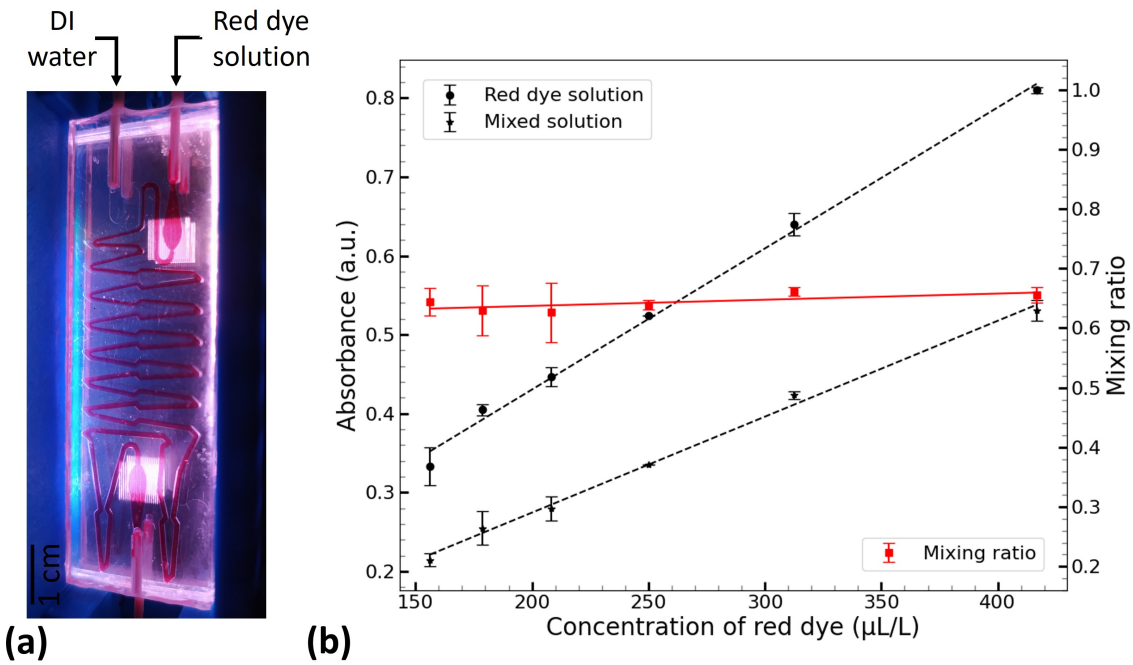

Figure 5.27. Evaluation of mixing efficiency using (a) captured image (b) absorbance readings of red dye solution and its mixture with DI water at 450 nm.

The data obtained revealed a consistent mixing ratio of 2:1, pertaining to the red dye and DI water, respectively. Mixing ratio was determined by comparing the absorbance values measured pre-mixing with those post-mixing, demonstrating the effectiveness and consistency of the mixing process within the microchannel under study.

5.8. pH Measurement of Colored Liquids

As verified in Section 5.4, comparing the absorbance of a solution before and after the introduction of a pH indicator solution allows for the estimation of the solution's pH. There is a linear relationship of pH and measured absorbance values. For verification of differential colorimetric pH measurement on the same setup, phenol red was used as a pH indicator.

The samples were continuously introduced into the microfluidic channel, where they were mixed with the indicator solution, and the absorption responses of the mixed solution were recorded at 450 and 550 nm. Blue food coloring dye in 3 different concentrations of dye to buffer solution (600:1, 600:4 and 600:8) was used in the experiments where maximum absorbance is in the red region (650 nm). For experiments involving blue food coloring dye, the absorbance at 650 nm was used to calculate the actual mixing ratio. Furtherly, the actual mixing ratio can be calculated from the absorbance ratio of 650 nm since it is directly related to the blue dye concentration, not to the pH indicator effect.

Figure 5.28(a) depicts an image that captures the transition from blue dye to its mixture with phenol red, illustrating the beginning and end of the mixing process in microchannels. In Figure 5.28(b), the logarithm of absorbance ratios at 550 and 450 nm is plotted to graphically represent the relationship between pH values and the absorbance readings.

This analysis distinguishes between 'uncompensated data', which doesn't consider the blue dye's spectral response, and 'compensated data', which does, alongside the actual mixing ratio. The results clearly indicate that the relationship between absorbance and pH is not discernible without accounting for the sample color's effect. As the concentration of the blue color increases, the deviation from the compensated measurements becomes more pronounced, highlighting the influence of sample color on absorbance and pH relation.

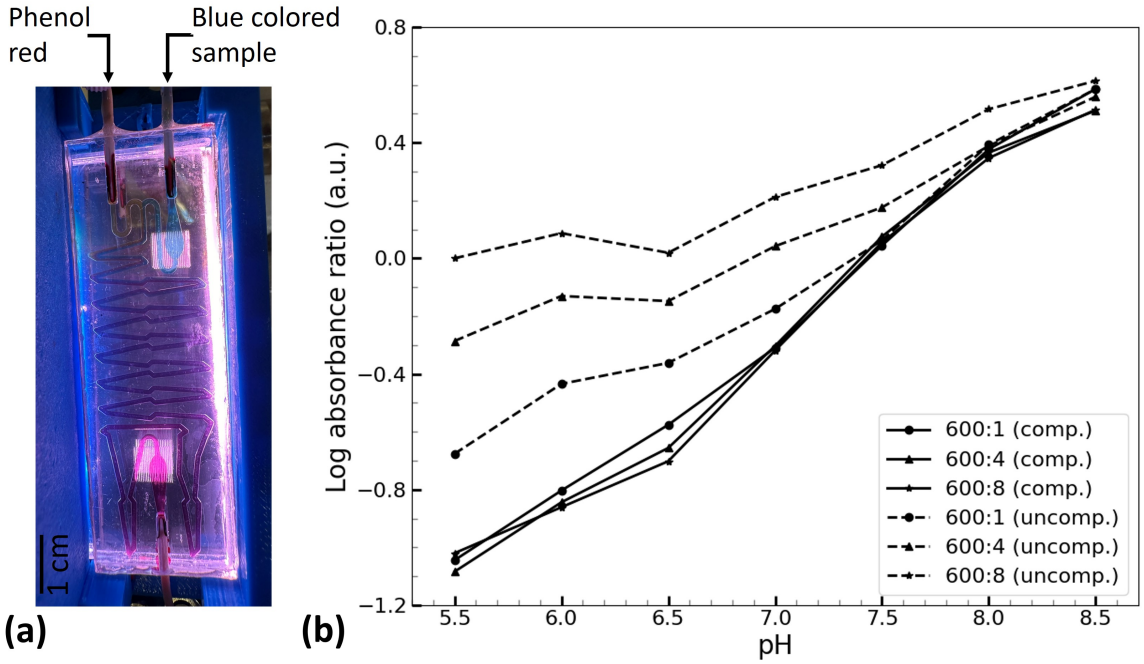

Figure 5.28. Evaluation of differential colorimetric method for pH measurement using (a) captured image (b) ratio of absorbance values at 450 nm and 550 nm.

Closer looking at the compensated data as given in Figure 5.29, the linear regression analysis of this relationship yields a model $y = 0.5615x - 4.1993$ with a standard error of 0.0147, indicating a linear response within the experimented range. The slope of the regression line suggests that for each unit increase in pH, the absorbance increases by approximately 0.5615 units.

The established linear relationship proves the reliability of the proposed method within the experimental conditions. Nevertheless, it is important to acknowledge that colorimetric measurement of pH may diverge from theoretical predictions due to a range of factors. The Beer-Lambert law's linearity can be degraded at high and low concentrations. Instrumental factors, like stray light, can introduce errors. Chemical interference between sample and indicator, shifts in pKa, and sample conditions may also impact results. Although Henderson-Hasselbalch equation offers a theoretical foundation, considering all these factors is critical for improving the accuracy of spectrophotometric measurements.

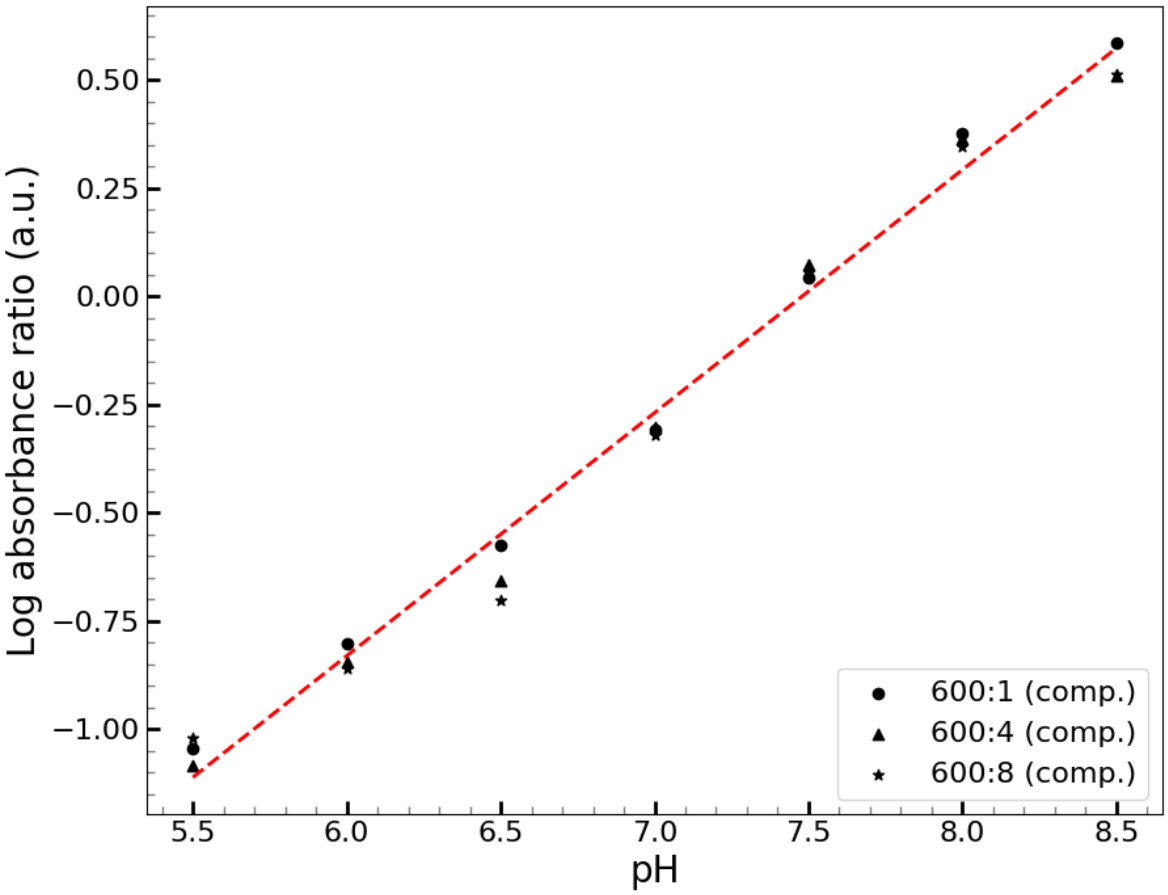

Figure 5.29. Compensated absorbance ratio for three different blue dye concentrations.

6. CONCLUSION AND FUTURE WORK

This thesis represents a significant advancement in the field of microfluidic technology. It addresses existing challenges and introduces practical solutions across various aspects. The study began by exploring the design and fabrication of an automated injection system using syringe pumps. It delved into microfluidic chip fabrication methods like laser ablation and micromilling for the development of the automated microfluidic platform.

The research then progressed to droplet microfluidics, focusing on the generation and manipulation of droplets. This was achieved by controlling the flow rates of different dyes, demonstrating the system's performance in both commercially available and custom-fabricated chips.

A novel sampling injection method was also introduced, along with an analysis of the electrical analogy for eliminating flow fluctuations and optimizing the system's performance. This electrical analogy encompassed the microfluidic chip, injection system, and tubing connections to provide insights into performance optimization by preventing flow inconsistencies. Notably, this method extends beyond the proposed design. It contributes to the field of microfluidics since it is generally applicable in a wider range of microfluidic systems.

The final part of this research was the introduction of a new sensor design for automated sampling and simple injection, based on absorption-based pH measurement. This innovative design used a microfluidic chip with an integrated passive micromixer to guarantee effective mixing of the sample solution with a pH indicator. The efficiency of the mixer was validated through 3D CFD simulations and experimental work. It finally leaded to the implementation of differential colorimetric pH measurement using this microfluidic chip.

In conclusion, this thesis not only validates a breakthrough in automated liquid analysis using microfluidic technology but also opens up possibilities for future research and diverse applications. The integration of low-cost spectral sensors and novel pH measurement methods marks a significant step forward, addressing existing challenges and enhancing precision in both scientific and industrial applications.

6.1. Future Work

Future advancements in pH measurement technology should consider extending the pH measurement range by utilizing different indicators or combinations thereof. This approach would allow for customization depending on the specific colored liquids used by optimizing both the pH range and the indicator wavelength to maintain accuracy and reliability. Addressing bubble formation in microfluidic chips is crucial, as it directly impacts light intensity and absorbance readings. The integration of bubble traps into the chip design is a promising solution to mitigate this issue.

A significant enhancement would be the incorporation of a feedback mechanism, such as a beam splitter, for continuous monitoring and adjustment of LED light intensity degradation. This improvement would facilitate real-time monitoring and calibration for consistent and reliable data over extended periods.

The proposed sampling injection method is versatile and suitable for a wide range of applications from industrial processes to natural aquatic systems and pH monitoring in living organisms. Its adaptability to various sensing methods, including electrochemical, piezoelectric, and optical sensors, further enhances its applicability across multiple fields, making it a broadly useful tool in diverse environments.

REFERENCES

1. Tabeling, P., *Introduction to Microfluidics*, Oxford University Press, New York, 2005.

2. Whitesides, G. M., "The Origins and the Future of Microfluidics", *Nature*, Vol. 442, pp. 368–373, 2006.

3. Chiu, D. T., A. J. Demello, D. Di Carlo, P. S. Doyle, C. Hansen, R. M. Maceiczyk and R. C. Wootton, "Small but Perfectly Formed? Successes, Challenges, and Opportunities for Microfluidics in the Chemical and Biological Sciences", *Chem*, Vol. 2, pp. 201–223, 2017.

4. Gencturk, E., K. O. Ulgen and S. Mutlu, "Thermoplastic Microfluidic Bioreactors with Integrated Electrodes to Study Tumor Treating Fields on Yeast Cells", *Biomicrofluidics*, Vol. 14, No. 3, 2020.

5. Odabasi, I. E., E. Gencturk, S. Puza, S. Mutlu and K. O. Ulgen, "A Low Cost PS Based Microfluidic Platform to Investigate Cell Cycle Towards Developing a Therapeutic Strategy for Cancer", *Biomedical Microdevices*, Vol. 20, pp. 1–13, 2018.

6. Gencturk, E., E. Yurdakul, A. Y. Celik, S. Mutlu and K. O. Ulgen, "Cell Trapping Microfluidic Chip Made of Cyclo Olefin Polymer Enabling Two Concurrent Cell Biology Experiments with Long Term Durability", *Biomedical Microdevices*, Vol. 22, pp. 1–12, 2020.

7. Nielsen, J. B., R. L. Hanson, H. M. Almughamsi, C. Pang, T. R. Fish and A. T. Woolley, "Microfluidics: Innovations in Materials and Their Fabrication and Functionalization", *Analytical Chemistry*, Vol. 92, pp. 150–168, 2019.

8. Coulter, B., A. Biosciences, B. Nanosciences, P. Elmer and B. D. Biosciences,

"Microfluidics in Commercial Applications; an Industry Perspective", *Lab Chip*, Vol. 6, pp. 1118–1121, 2006.

9. Battat, S., D. A. Weitz and G. M. Whitesides, "An Outlook on Microfluidics: The Promise and the Challenge", *Lab on a Chip*, Vol. 22, No. 3, pp. 530–536, 2022.

10. Nguyen, N.-T., S. T. Wereley and S. A. Mousavi Shaegh, *Fundamentals and Applications of Microfluidics*, Third Edition, Artech House, Massachusetts, 2019.

11. Kant, R., "Textile Dyeing Industry an Environmental Hazard", *Natural Science*, Vol. 4, No. 1, pp. 22–26, 2012.

12. Chequer, F. D., G. R. De Oliveira, E. A. Ferraz, J. C. Cardoso, M. B. Zanoni and D. P. De Oliveira, "Textile Dyes: Dyeing Process and Environmental Impact", *Eco-friendly Textile Dyeing and Finishing*, Vol. 6, No. 6, pp. 151–176, 2013.

13. Khatri, A., M. H. Peerzada, M. Mohsin and M. White, "A Review on Developments in Dyeing Cotton Fabrics with Reactive Dyes for Reducing Effluent Pollution", *Journal of Cleaner Production*, Vol. 87, pp. 50–57, 2015.

14. Pezzella, C., S. Giacobbe, V. G. Giacobelli, L. Guarino, S. Kylic, M. Sener, G. Sannia and A. Piscitelli, "Green Routes Towards Industrial Textile Dyeing: A Laccase Based Approach", *Journal of Molecular Catalysis B: Enzymatic*, Vol. 134, pp. 274–279, 2016.

15. Terkesli, I., C. Demircan, I. Demirci, S. Yavuz and M. Taygun, "Industrial Spectrophotometric Smart Sensor Towards Real-time Optimization of Textile Dyeing Process", *2019 IEEE Sensors Applications Symposium (SAS)*, pp. 1–5, 2019.

16. Park, J., "Dyeing Laboratory Developments", *Review of Progress in Coloration*, Vol. 34, pp. 86–94, 2004.

17. Ingamells, W., *Colour for Textiles*, Society of Dyers and Colourists, Bradford, 1993.

18. Johnson, A., *The Theory of Coloration of Textiles*, Second Edition, Society of Dyers and Colourists, Bradford, 1989.

19. Kishida, N., J. H. Kim, M. Chen, H. Sasaki and R. Sudo, "Effectiveness of Oxidation-reduction Potential and pH as Monitoring and Control Parameters for Nitrogen Removal in Swine Wastewater Treatment by Sequencing Batch Reactors", *Journal of Bioscience and Bioengineering*, Vol. 96, No. 3, pp. 285–290, 2003.

20. Liu, Y., Y. Chen and Q. Zhou, "Effect of Initial pH Control on Enhanced Biological Phosphorus Removal from Wastewater Containing Acetic and Propionic Acids", *Chemosphere*, Vol. 66, No. 1, pp. 123–129, 2007.

21. Sun, M., F. Chen, J. Qu, H. Liu and R. Liu, "Optimization and Control of Electro-Fenton Process by pH Inflection Points: A Case of Treating Acrylic Fiber Manufacturing Wastewater", *Chemical Engineering Journal*, Vol. 269, pp. 399–407, 2015.

22. Ratzke, C. and J. Gore, "Modifying and Reacting to the Environmental pH can Drive Bacterial Interactions", *PLoS Biology*, Vol. 16, No. 3, p. e2004248, 2018.

23. Penn, C. J. and J. J. Camberato, "A Critical Review on Soil Chemical Processes that Control How Soil pH Affects Phosphorus Availability to Plants", *Agriculture*, Vol. 9, No. 6, p. 120, 2019.

24. Malik, A. A., J. Puissant, K. M. Buckeridge, T. Goodall, N. Jehmlich, S. Chowdhury and Others, "Land Use Driven Change in Soil pH Affects Microbial Carbon Cycling Processes", *Nature Communications*, Vol. 9, No. 1, p. 3591, 2018.

25. Talbot-Walsh, G., D. Kannar and C. Selomulya, "pH Effect on the Physico-

chemical, Microstructural and Sensorial Properties of Processed Cheese Manufactured with Various Starches", *LWT*, Vol. 111, pp. 414–422, 2019.

26. Webster, J. G. and H. Eren (Editors), *Measurement, Instrumentation, and Sensors Handbook: Two-Volume Set*, Second Edition, CRC Press, Florida, 2018.

27. Sinha, S. and T. Pal, "A Comprehensive Review of FET-based pH Sensors: Materials, Fabrication Technologies, and Modeling", *Electrochemical Science Advances*, Vol. 2, No. 5, p. e2100147, 2022.

28. Vivaldi, F., P. Salvo, N. Poma, A. Bonini, D. Biagini, L. Del Noce and Others, "Recent Advances in Optical, Electrochemical, and Field Effect pH Sensors", *Chemosensors*, Vol. 9, No. 2, p. 33, 2021.

29. Welch, D. and J. B. Christen, "Real-time Feedback Control of pH within Microfluidics Using Integrated Sensing and Actuation", *Lab on a Chip*, Vol. 14, No. 6, pp. 1191–1197, 2014.

30. Wencel, D., T. Abel and C. McDonagh, "Optical Chemical pH Sensors", *Analytical Chemistry*, Vol. 86, No. 1, pp. 15–29, 2014.

31. Hanson, M. A., X. Ge, Y. Kostov, K. A. Brorson, A. R. Moreira and G. Rao, "Comparisons of Optical pH and Dissolved Oxygen Sensors with Traditional Electrochemical Probes During Mammalian Cell Culture", *Biotechnology and Bioengineering*, Vol. 97, No. 4, pp. 833–841, 2007.

32. Steinegger, A., O. S. Wolfbeis and S. M. Borisov, "Optical Sensing and Imaging of pH Values: Spectroscopies, Materials, and Applications", *Chemical Reviews*, Vol. 120, pp. 12357–12489, 2020.

33. Sabnis, R. W., *Handbook of Acid-base Indicators*, CRC Press, Florida, 2007.

34. Bishop, E., *Indicators: International Series of Monographs in Analytical Chem-*

istry, Elsevier Science, Braunschweig, 2013.

35. Shamsipur, M., A. Barati and Z. Nematifar, "Fluorescent pH Nanosensors: Design Strategies and Applications", *Journal of Photochemistry and Photobiology C: Photochemistry Reviews*, Vol. 39, pp. 76–141, 2019.

36. Singh, S. and B. D. Gupta, "Fabrication and Characterization of a Highly Sensitive Surface Plasmon Resonance Based Fiber Optic pH Sensor Utilizing High Index Layer and Smart Hydrogel", *Sensors and Actuators B: Chemical*, Vol. 173, pp. 268–273, 2012.

37. Paynter, S. and D. A. Russell, "Surface Plasmon Resonance Measurement of pH-induced Responses of Immobilized Biomolecules: Conformational Change or Electrostatic Interaction Effects?", *Analytical Biochemistry*, Vol. 309, No. 1, pp. 85–95, 2002.

38. Rivero, P. J., J. Goicoechea, M. Hernaez, A. B. Socorro, I. R. Matias and F. J. Arregui, "Optical Fiber Resonance-based pH Sensors Using Gold Nanoparticles into Polymeric Layer-by-layer Coatings", *Microsystem Technologies*, Vol. 22, pp. 1821–1829, 2016.

39. Lian, Y., W. Zhang, L. Ding, X. Zhang, Y. Zhang and X. D. Wang, "Nanomaterials for Intracellular pH Sensing and Imaging", *Novel Nanomaterials for Biomedical, Environmental and Energy Applications*, pp. 241–273, Elsevier, Amsterdam, 2019.

40. Jin, T., A. Sasaki, M. Kinjo and J. Miyazaki, "A Quantum Dot-Based Ratiometric pH Sensor", *Chemical Communications*, Vol. 46, No. 14, pp. 2408–2410, 2010.

41. Ast, S., P. J. Rutledge and M. H. Todd, "pH-Responsive Quantum Dots (RQDs) that Combine a Fluorescent Nanoparticle with a pH-sensitive Dye", *Physical Chemistry Chemical Physics*, Vol. 16, No. 46, pp. 25255–25257, 2014.

42. Wang, H., B. Liu, Z. Li and L. Yang, "Multi-wavelength Spectrophotometric Determination of pH Using Phenol Red–doped Sol–gel Film Sensors", *Spectroscopy Letters*, Vol. 50, No. 6, pp. 307–315, 2017.

43. Choudhary, S., B. Joshi, G. Pandey and A. Joshi, "Application of Single and Dual Fluorophore-based pH Sensors for Determination of Milk Quality and Shelf Life using a Fibre Optic Spectrophotometer", *Sensors and Actuators B: Chemical*, Vol. 298, p. 126925, 2019.

44. Ehgartner, J., H. Wiltsche, S. M. Borisov and T. Mayr, "Low Cost Referenced Luminescent Imaging of Oxygen and pH with a 2-CCD Colour Near Infrared Camera", *Analyst*, Vol. 139, No. 19, pp. 4924–4933, 2014.

45. Li, Z., L. Xia, G. Li and Y. Hu, "Raman Spectroscopic Imaging of pH Values in Cancerous Tissue by Using Polyaniline@ Gold Nanoparticles", *Microchimica Acta*, Vol. 186, pp. 1–8, 2019.

46. Meier, R. J., L. H. Fischer, O. S. Wolfbeis and M. Schäferling, "Referenced Luminescent Sensing and Imaging with Digital Color Cameras: A Comparative Study", *Sensors and Actuators B: Chemical*, Vol. 177, pp. 500–506, 2013.

47. Cao, L., D. Qi, Q. Li, B. Yang, Y. Zhang, S. Zhang, S. Qi, Y. Zhang and Y. Liu, "Spectrophotometric Loop Flow Analyzer for High-precision Measurement of Seawater pH", *Talanta*, Vol. 224, p. 121775, 2021.

48. Kim, S. D., Y. Koo and Y. Yun, "A Smartphone-based Automatic Measurement Method for Colorimetric pH Detection Using a Color Adaptation Algorithm", *Sensors*, Vol. 17, No. 7, p. 1604, 2017.

49. Lu, Y., Q. Feng, R. Zhang, H. Lu, J. Su, Y. Cui and L. Zhu, "An Online pH Detection System based on a Microfluidic Chip", *Analytica Chimica Acta*, Vol. 1106, pp. 71–78, 2020.

50. Li, D.-Y., H. Zhang, Z. Li, L.-W. Zhou, M.-D. Zhang, X.-Y. Pu, Y.-Z. Sun, H. Liu and Y.-X. Zhang, "High Sensitivity pH Sensing by Using a Ring Resonator Laser Integrated into a Microfluidic Chip", *Optics Express*, Vol. 30, No. 3, pp. 4106–4116, 2022.

51. Gao, J., Y. Wang, Y. Han, Y. Gao, C. Wang, L. Han and Y. Zhang, "Graphene-based Field-effect Transistors Integrated with Microfluidic Chip for Real-time pH Monitoring of Seawater", *Journal of Materials Science: Materials in Electronics*, Vol. 31, pp. 15372–15380, 2020.

52. Moghaddam, M. S., H. Latifi, E. Abedini, M. Ghazanfar, E. Behroodi and M. S. Sadeghi, "Label-Free Optical pH Measurement Based on Chitosan-TEOS-PDMS Hydrogel Layer for Microfluidic Applications", *IEEE Sensors Journal*, Vol. 23, No. 1, pp. 97–103, 2022.

53. Tovar, M., L. Mahler, S. Buchheim, M. Roth and M. A. Rosenbaum, "Monitoring and External Control of pH in Microfluidic Droplets During Microbial Culturing", *Microbial Cell Factories*, Vol. 19, No. 1, pp. 1–9, 2020.

54. Escobedo, P., C. E. Ramos-Lorente, A. Martínez-Olmos, M. A. Carvajal, M. Ortega-Muñoz, I. de Orbe-Payá, F. Hernández-Mateo, F. Santoyo-González, L. F. Capitán-Vallvey, A. J. Palma *et al.*, "Wireless Wearable Wristband for Continuous Sweat pH Monitoring", *Sensors and Actuators B: Chemical*, Vol. 327, p. 128948, 2021.

55. Kumar, R., H. Nguyen, B. Rente, C. Tan, T. Sun and K. T. Grattan, "A Portable 'plug-and-play' Fibre Optic Sensor for In-situ Measurements of pH Values for Microfluidic Applications", *Micromachines*, Vol. 13, No. 8, p. 1224, 2022.

56. Rérolle, V. M., C. F. Floquet, A. J. Harris, M. C. Mowlem, R. R. Bellerby and E. P. Achterberg, "Development of a Colorimetric Microfluidic pH Sensor for Autonomous Seawater Measurements", *Analytica Chimica Acta*, Vol. 786, pp.

124–131, 2013.

57. de Vargas Sansalvador, I. M. P., C. D. Fay, J. Cleary, A. M. Nightingale, M. C. Mowlem and D. Diamond, "Autonomous Reagent-based Microfluidic pH Sensor Platform", *Sensors and Actuators B: Chemical*, Vol. 225, pp. 369–376, 2016.

58. Pinto, V., C. Araújo, P. Sousa and L. Goncalves, "A Low-cost Lab-on-a-chip Device for Marine pH Quantification by Colorimetry", *Sensors and Actuators B: Chemical*, Vol. 290, pp. 285–292, 2019.

59. Elmas, S., A. Pospisilova, A. A. Sekulska, V. Vasilev, T. Nann, S. Thornton and C. Priest, "Photometric Sensing of Active Chlorine, Total Chlorine, and pH on a Microfluidic Chip for Online Swimming Pool Monitoring", *Sensors*, Vol. 20, p. 3099, 2020.

60. Longwell, S. A. and P. M. Fordyce, "micrIO: An Open-source Autosampler and Fraction Collector for Automated Microfluidic Input–Output", *Lab on a Chip*, Vol. 20, No. 1, pp. 93–106, 2020.

61. Lake, J. R., K. C. Heyde and W. C. Ruder, "Low-cost Feedback-controlled Syringe Pressure Pumps for Microfluidics Applications", *PLoS One*, Vol. 12, No. 4, p. e0175089, 2017.

62. Kim, H., D. Cheon, J. Lim and K. Nam, "Robust Flow Control of a Syringe Pump Based on Dual-Loop Disturbance Observers", *IEEE Access*, Vol. 7, pp. 135427–135438, 2019.

63. Allen, J. W. and S. N. Bhatia, "Formation of Steady-state Oxygen Gradients in Vitro: Application to Liver Zonation", *Biotechnology and Bioengineering*, Vol. 82, No. 3, pp. 253–262, 2003.

64. Li, P., X. Tang, Y. Lin, M. Kojima, Q. Huang and T. Arai, "Microfluidic Device for Analyzing Self-adaption of Cancer Cell During Squeezing in Channel", *2018*

IEEE International Conference on Cyborg and Bionic Systems, pp. 88–92, IEEE, 2018.

65. Narayanamurthy, V., Z. Jeroish, K. Bhuvaneshwari, P. Bayat, R. Premkumar, F. Samsuri and M. M. Yusoff, "Advances in Passively Driven Microfluidics and Lab-on-chip Devices: a Comprehensive Literature Review and Patent Analysis", *RSC Advances*, Vol. 10, No. 20, pp. 11652–11680, 2020.

66. Atay, A., A. Topuz, B. Sarıarslan, E. Yıldırım, J. Charmet, K. Couling and B. Çetin, "Flow Rate-controlled Pipetting for Microfluidics: Second-generation Flexible Hydraulic Reservoir (FHRv2)", *Microfluidics and Nanofluidics*, Vol. 25, pp. 1–10, 2021.

67. Esser, F., T. Masselter and T. Speck, "Silent Pumpers: A Comparative Topical Overview of the Peristaltic Pumping Principle in Living Nature, Engineering, and Biomimetics", *Advanced Intelligent Systems*, Vol. 1, No. 2, p. 1900009, 2019.

68. Biviano, M. D., M. V. Paludan, A. H. Christensen, E. V. Østergaard and K. H. Jensen, "Smoothing Oscillatory Peristaltic Pump Flow with Bioinspired Passive Components", *Physical Review Applied*, Vol. 18, No. 6, p. 064013, 2022.

69. Niculescu, A. G., C. Chircov, A. C. Bîrcă and A. M. Grumezescu, "Fabrication and Applications of Microfluidic Devices: A review", *International Journal of Molecular Sciences*, Vol. 22, No. 4, p. 2011, 2021.

70. Gale, B. K., A. R. Jafek, C. J. Lambert, B. L. Goenner, H. Moghimifam, U. C. Nze and S. K. Kamarapu, "A Review of Current Methods in Microfluidic Device Fabrication and Future Commercialization Prospects", *Inventions*, Vol. 3, No. 3, p. 60, 2018.

71. Gyimah, N., O. Scheler, T. Rang and T. Pardy, "Can 3D Printing Bring Droplet Microfluidics to Every Lab? A Systematic Review", *Micromachines*, Vol. 12,

No. 3, p. 339, 2021.

72. Ho, C. M. B., S. H. Ng, K. H. H. Li and Y. J. Yoon, "3D Printed Microfluidics for Biological Applications", *Lab on a Chip*, Vol. 15, No. 18, pp. 3627–3637, 2015.

73. Matellan, C. and A. E. del Río Hernández, "Cost-effective Rapid Prototyping and Assembly of Poly (methyl methacrylate) Microfluidic Devices", *Scientific Reports*, Vol. 8, No. 1, p. 6971, 2018.

74. Klank, H., J. P. Kutter and O. Geschke, "CO2-laser Micromachining and Back-end Processing for Rapid Production of PMMA-based Microfluidic Systems", *Lab on a Chip*, Vol. 2, No. 4, pp. 242–246, 2002.

75. Cheng, J. Y., C. W. Wei, K. H. Hsu and T. H. Young, "Direct-write Laser Micromachining and Universal Surface Modification of PMMA for Device Development", *Sensors and Actuators B: Chemical*, Vol. 99, No. 1, pp. 186–196, 2004.

76. Hong, T. F., W. J. Ju, M. C. Wu, C. H. Tai, C. H. Tsai and L. M. Fu, "Rapid Prototyping of PMMA Microfluidic Chips Utilizing a CO2 Laser", *Microfluidics and Nanofluidics*, Vol. 9, pp. 1125–1133, 2010.

77. Chung, C. K., Y. C. Lin and G. R. Huang, "Bulge Formation and Improvement of the Polymer in CO2 Laser Micromachining", *Journal of Micromechanics and Microengineering*, Vol. 15, No. 10, p. 1878, 2005.

78. Scott, S. M. and Z. Ali, "Fabrication Methods for Microfluidic Devices: An Overview", *Micromachines*, Vol. 12, No. 3, p. 319, 2021.

79. Chen, P. C., C. W. Pan, W. C. Lee and K. M. Li, "An Experimental Study of Micromilling Parameters to Manufacture Microchannels on a PMMA Substrate", *The International Journal of Advanced Manufacturing Technology*, Vol. 71, pp. 1623–1630, 2014.

80. Yan, Y., P. Zhou, H. Wang and Y. Mao, "Thermal Effect on Poly (methyl methacrylate) (PMMA) Material Removal in the Micromilling Process", *Polymers*, Vol. 12, No. 9, p. 2122, 2020.

81. Gu, W., X. Zhu, N. Futai, B. S. Cho and S. Takayama, "Computerized Microfluidic Cell Culture Using Elastomeric Channels and Braille Displays", *Proceedings of the National Academy of Sciences of the United States of America*, Vol. 101, No. 45, pp. 15861–15866, 2004.

82. Simon, M. G. and A. P. Lee, "Microfluidic Droplet Manipulations and Their Applications", *Microdroplet Technology*, pp. 23–50, Springer, New York, 2012.

83. Schlichting, H. and K. Gersten, *Boundary-Layer Theory*, Ninth Edition, Springer, Heidelberg, 2016.

84. Falkovich, G., *Fluid Mechanics*, Second Edition, Cambridge University Press, Cambridge, 2018.

85. Sassa, F., J. Fukuda and H. Suzuki, "Microprocessing of Liquid Plugs for Bio/chemical Analyses", *Analytical Chemistry*, Vol. 80, No. 16, pp. 6206–6213, 2008.

86. Shang, L., Y. Cheng and Y. Zhao, "Emerging Droplet Microfluidics", *Chemical Reviews*, Vol. 117, No. 12, pp. 7964–8040, 2017.

87. Bezinge, L., R. M. Maceiczyk, I. Lignos, M. V. Kovalenko and A. J. deMello, "Pick a Color MARIA: Adaptive Sampling Enables the Rapid Identification of Complex Perovskite Nanocrystal Compositions with Defined Emission Characteristics", *ACS Applied Materials and Interfaces*, Vol. 10, No. 22, pp. 18869–18878, 2018.

88. Teh, S.-Y., R. Lin, L.-H. Hung and A. P. Lee, "Droplet Microfluidics", *Lab on a Chip*, Vol. 8, No. 2, pp. 198–220, 2008.

89. Christopher, G. F. and S. L. Anna, "Microfluidic Methods for Generating Continuous Droplet Streams", *Journal of Physics D: Applied Physics*, Vol. 40, No. 19, pp. 319–336, 2007.

90. Baccouche, A., S. Okumura, R. Sieskind, E. Henry, N. Aubert-Kato, N. Bredeche, J.-F. Bartolo, V. Taly, Y. Rondelez, T. Fujii *et al.*, "Massively Parallel and Multiparameter Titration of Biochemical Assays with Droplet Microfluidics", *Nature Protocols*, Vol. 12, No. 9, pp. 1912–1932, 2017.

91. Elvira, K. S., F. Gielen, S. S. Tsai and A. M. Nightingale, "Materials and Methods for Droplet Microfluidic Device Fabrication", *Lab on a Chip*, Vol. 22, No. 5, pp. 859–875, 2022.

92. Slaney, T. R., J. Nie, N. D. Hershey, P. K. Thwar, J. Linderman, M. A. Burns and R. T. Kennedy, "Push–pull Perfusion Sampling with Segmented Flow for High Temporal and Spatial Resolution in Vivo Chemical Monitoring", *Analytical Chemistry*, Vol. 83, No. 13, pp. 5207–5213, 2011.

93. Radisic, M., M. Euloth, L. Yang, R. Langer, L. E. Freed and G. Vunjak-Novakovic, "High-density Seeding of Myocyte Cells for Cardiac Tissue Engineering", *Biotechnology and Bioengineering*, Vol. 82, No. 4, pp. 403–414, 2003.

94. Wu, Z., H. Jensen, J. Gamby, X. Bai and H. H. Girault, "A Flexible Sample Introduction Method for Polymer Microfluidic Chips Using a Push/pull Pressure Pump", *Lab on a Chip*, Vol. 4, No. 5, pp. 512–515, 2004.

95. Xu, G., D. Y. S. Lee, H. Xie, D. Chiew, T.-M. Hsieh, E. M. Ali, X. Lun Looi, M.-H. Li and J. Y. Ying, "A Self-Contained Polymeric Cartridge for Automated Biological Sample Preparation", *Biomicrofluidics*, Vol. 5, No. 034107, 2011.

96. Lee, G. B., C. C. Chang, S. B. Huang and R. J. Yang, "The Hydrodynamic Focusing Effect Inside Rectangular Microchannels", *Journal of Micromechanics*

and Microengineering, Vol. 16, No. 5, p. 1024, 2006.

97. Liu, M., Y. Chen, Q. Guo, R. Li, X. Sun and J. Yang, "Controllable Positioning and Alignment of Silver Nanowires by Tunable Hydrodynamic Focusing", *Nanotechnology*, Vol. 22, No. 12, p. 125302, 2011.

98. Perdigones, F. A., A. Luque and J. M. Quero, "Correspondence between Electronics and Fluids in MEMS: Designing Microfluidic Systems Using Electronics", *IEEE Industrial Electronics Magazine*, Vol. 8, No. 4, pp. 6–17, 2014.

99. Li, S. S. and C. M. Cheng, "Analogy among Microfluidics, Micromechanics, and Microelectronics", *Lab on a Chip*, Vol. 13, No. 19, pp. 3782–3788, 2013.

100. Lee, K., C. Kim, B. Ahn, R. Panchapakesan, A. R. Full, L. Nordee, J. Y. Kang and K. W. Oh, "Generalized Serial Dilution Module for Monotonic and Arbitrary Microfluidic Gradient Generators", *Lab on a Chip*, Vol. 9, No. 5, pp. 709–717, 2009.

101. Oh, K. W., K. Lee, B. Ahn and E. P. Furlani, "Design of Pressure-driven Microfluidic Networks Using Electric Circuit Analogy", *Lab on a Chip*, Vol. 12, No. 3, pp. 515–545, 2012.

102. Kim, C., K. S. Lee, J. H. Bang, Y. E. Kim, M.-C. Kim, K. W. Oh, S. H. Lee and J. Y. Kang, "3-Dimensional Cell Culture for On-chip Differentiation of Stem Cells in Embryoid Body", *Lab on a Chip*, Vol. 11, No. 5, pp. 874–882, 2011.

103. Kim, C., K. Lee, J. H. Kim, K. S. Shin, K. J. Lee, T. S. Kim and J. Y. Kang, "A Serial Dilution Microfluidic Device Using a Ladder Network Generating Logarithmic or Linear Concentrations", *Lab on a Chip*, Vol. 8, No. 3, pp. 473–479, 2008.

104. Li, Z., C. Liu and J. Sun, "Hydraulic–Electric Analogy for Design and Operation of Microfluidic Systems", *Lab on a Chip*, Vol. 23, No. 15, pp. 3311–3327, 2023.

105. Kalantarifard, A., E. A. Haghighi and C. Elbuken, "Damping Hydrodynamic Fluctuations in Microfluidic Systems", *Chemical Engineering Science*, Vol. 178, pp. 238–247, 2018.

106. Cartas Ayala, M. A., *Hydrodynamic Resistance and Sorting of Deformable Particles in Microfluidic Circuits*, Ph.D. Thesis, Massachusetts Institute of Technology, 2013.

107. Weiss, M., M. I. Hug, T. Neff and J. Fischer, "Syringe Size and Flow Rate Affect Drug Delivery from Syringe Pumps", *Canadian Journal of Anesthesia*, Vol. 47, No. 10, pp. 1031–1035, 2000.

108. Bruus, H., *Theoretical Microfluidics*, Oxford University Press, New York, 2007.

109. Snijder, R. A., M. K. Konings, P. Lucas, T. C. Egberts and A. D. Timmerman, "Flow Variability and its Physical Causes in Infusion Technology: A Systematic Review of In Vitro Measurement and Modeling Studies", *Biomedical Engineering/Biomedizinische Technik*, Vol. 60, No. 4, pp. 277–300, 2015.

110. Westcott, C., *pH Measurements*, Academic Press, New York, 1978.

111. Salgado, L. V. and C. Vargas-Hernández, "Spectrophotometric Determination of the pKa, Isosbestic Point and Equation of Absorbance vs. pH for a Universal pH Indicator", *American Journal of Analytical Chemistry*, Vol. 5, No. 17, p. 1290, 2014.

112. De Meyer, T., K. Hemelsoet, V. Van Speybroeck and K. De Clerck, "Substituent Effects on Absorption Spectra of pH Indicators: An Experimental and Computational Study of Sulfonphthaleine Dyes", *Dyes and Pigments*, Vol. 102, pp. 241–250, 2014.

113. Cao, Q., X. Han and L. Li, "An Active Microfluidic Mixer Utilizing a Hybrid Gradient Magnetic Field", *International Journal of Applied Electromagnetics and*

Mechanics, Vol. 47, No. 3, pp. 583–592, 2015.

114. Frommelt, T., M. Kostur, M. Wenzel-Schäfer, P. Talkner, P. Hänggi and A. Wixforth, "Microfluidic Mixing via Acoustically Driven Chaotic Advection", *Physical Review Letters*, Vol. 100, No. 3, p. 034502, 2008.

115. Kim, S. J., F. Wang, M. A. Burns and K. Kurabayashi, "Temperature-programmed Natural Convection for Micromixing and Biochemical Reaction in a Single Microfluidic Chamber", *Analytical Chemistry*, Vol. 81, No. 11, pp. 4510–4516, 2009.

116. Sasaki, N., T. Kitamori and H. B. Kim, "AC Electroosmotic Micromixer for Chemical Processing in a Microchannel", *Lab on a Chip*, Vol. 6, No. 4, pp. 550–554, 2006.

117. Ward, K. and Z. H. Fan, "Mixing in Microfluidic Devices and Enhancement Methods", *Journal of Micromechanics and Microengineering*, Vol. 25, No. 9, p. 094001, 2015.

118. Li, Z., B. Zhang, D. Dang, X. Yang, W. Yang and W. Liang, "A Review of Microfluidic-based Mixing Methods", *Sensors and Actuators A: Physical*, p. 113757, 2022.

119. Stroock, A. D., S. K. Dertinger, A. Ajdari, I. Mezic, H. A. Stone and G. M. Whitesides, "Chaotic Mixer for Microchannels", *Science*, Vol. 295, No. 5555, pp. 647–651, 2002.

120. Kee, S. P. and A. Gavriilidis, "Design and Characterisation of the Staggered Herringbone Mixer", *Chemical Engineering Journal*, Vol. 142, No. 1, pp. 109–121, 2008.

121. Williams, M. S., K. J. Longmuir and P. Yager, "A Practical Guide to the Staggered Herringbone Mixer", *Lab on a Chip*, Vol. 8, No. 7, pp. 1121–1129, 2008.

122. Tofteberg, T., M. Skolimowski, E. Andreassen and O. Geschke, "A Novel Passive Micromixer: Lamination in a Planar Channel System", *Microfluidics and Nanofluidics*, Vol. 8, pp. 209–215, 2010.

123. Hong, C. C., J. W. Choi and C. H. Ahn, "A Novel In-plane Passive Microfluidic Mixer with Modified Tesla Structures", *Lab on a Chip*, Vol. 4, No. 2, pp. 109–113, 2004.

124. Parsa, M. K., F. Hormozi and D. Jafari, "Mixing Enhancement in a Passive Micromixer with Convergent–divergent Sinusoidal Microchannels and Different Ratio of Amplitude to Wave Length", *Computers and Fluids*, Vol. 105, pp. 82–90, 2014.

APPENDIX A: PERMISSIONS

A.1. Papers

Formation of Steady-state Oxygen Gradients in Vitro: Application to Liver Zonation [63]

JOHN WILEY AND SONS LICENSE
TERMS AND CONDITIONS

Feb 02, 2024

This Agreement between Boğaziçi University -- İsmail Terkeşli ("You") and John Wiley and Sons ("John Wiley and Sons") consists of your license details and the terms and conditions provided by John Wiley and Sons and Copyright Clearance Center.

License Number	5720940711148
License date	Feb 02, 2024
Licensed Content Publisher	John Wiley and Sons
Licensed Content Publication	Biotechnology & Bioengineering
Licensed Content Title	Formation of steady-state oxygen gradients in vitro: Application to liver zonation
Licensed Content Author	Sangeeta N. Bhatia, Jared W. Allen
Licensed Content Date	Feb 21, 2003
Licensed Content Volume	82
Licensed Content Issue	3
Licensed Content Pages	10
Type of use	Dissertation/Thesis
Requestor type	University/Academic
Format	Electronic
Portion	Figure/table
Number of figures/tables	1
Will you be translating?	No
Title of new work	Automated Microfluidic Platform with Syringe Pumps
Institution name	Boğaziçi University
Expected presentation date	Feb 2024
Order reference number	terkesli1
Portions	Figure 2
Requestor Location	Istanbul Levazim Mah. Aktas Sitesi B Blok No:9 Istanbul, 34340 Turkey Attn: İsmail Terkeşli
Publisher Tax ID	EU826007151
Total	0.00 USD

Figure A.1. Permission letter [63].

Microfluidic Device for Analyzing Self-adaption of Cancer Cell During Squeezing in Channel [64]

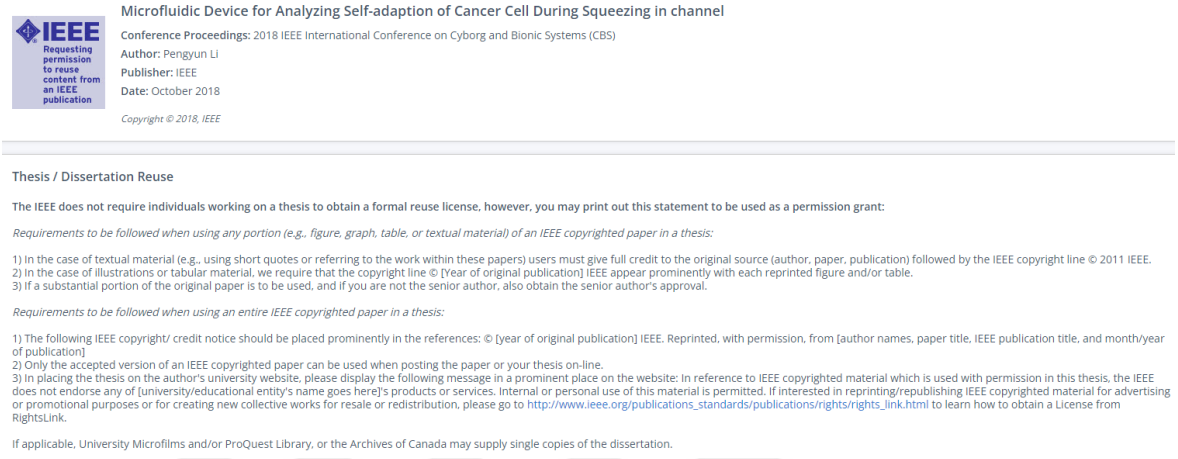

Microfluidic Device for Analyzing Self-adaption of Cancer Cell During Squeezing in channel

Conference Proceedings: 2018 IEEE International Conference on Cyborg and Bionic Systems (CBS)
Author: Pengyun Li
Publisher: IEEE
Date: October 2018

Copyright © 2018, IEEE

Thesis / Dissertation Reuse

The IEEE does not require individuals working on a thesis to obtain a formal reuse license, however, you may print out this statement to be used as a permission grant:

Requirements to be followed when using any portion (e.g., figure, graph, table, or textual material) of an IEEE copyrighted paper in a thesis:

1) In the case of textual material (e.g., using short quotes or referring to the work within these papers) users must give full credit to the original source (author, paper, publication) followed by the IEEE copyright line © 2011 IEEE.
2) In the case of illustrations or tabular material, we require that the copyright line © [Year of original publication] IEEE appear prominently with each reprinted figure and/or table.
3) If a substantial portion of the original paper is to be used, and if you are not the senior author, also obtain the senior author's approval.

Requirements to be followed when using an entire IEEE copyrighted paper in a thesis:

1) The following IEEE copyright/ credit notice should be placed prominently in the references: © [year of original publication] IEEE. Reprinted, with permission, from [author names, paper title, IEEE publication title, and month/year of publication]
2) Only the accepted version of an IEEE copyrighted paper can be used when posting the paper or your thesis on-line.
3) In placing the thesis on the author's university website, please display the following message in a prominent place on the website: In reference to IEEE copyrighted material which is used with permission in this thesis, the IEEE does not endorse any of [university/educational entity's name goes here]'s products or services. Internal or personal use of this material is permitted. If interested in reprinting/republishing IEEE copyrighted material for advertising or promotional purposes or for creating new collective works for resale or redistribution, please go to http://www.ieee.org/publications_standards/publications/rights/rights_link.html to learn how to obtain a License from RightsLink.

If applicable, University Microfilms and/or ProQuest Library, or the Archives of Canada may supply single copies of the dissertation.

Figure A.2. Permission letter [64].

Microfluidic Methods for Generating Continuous Droplet Streams [89]

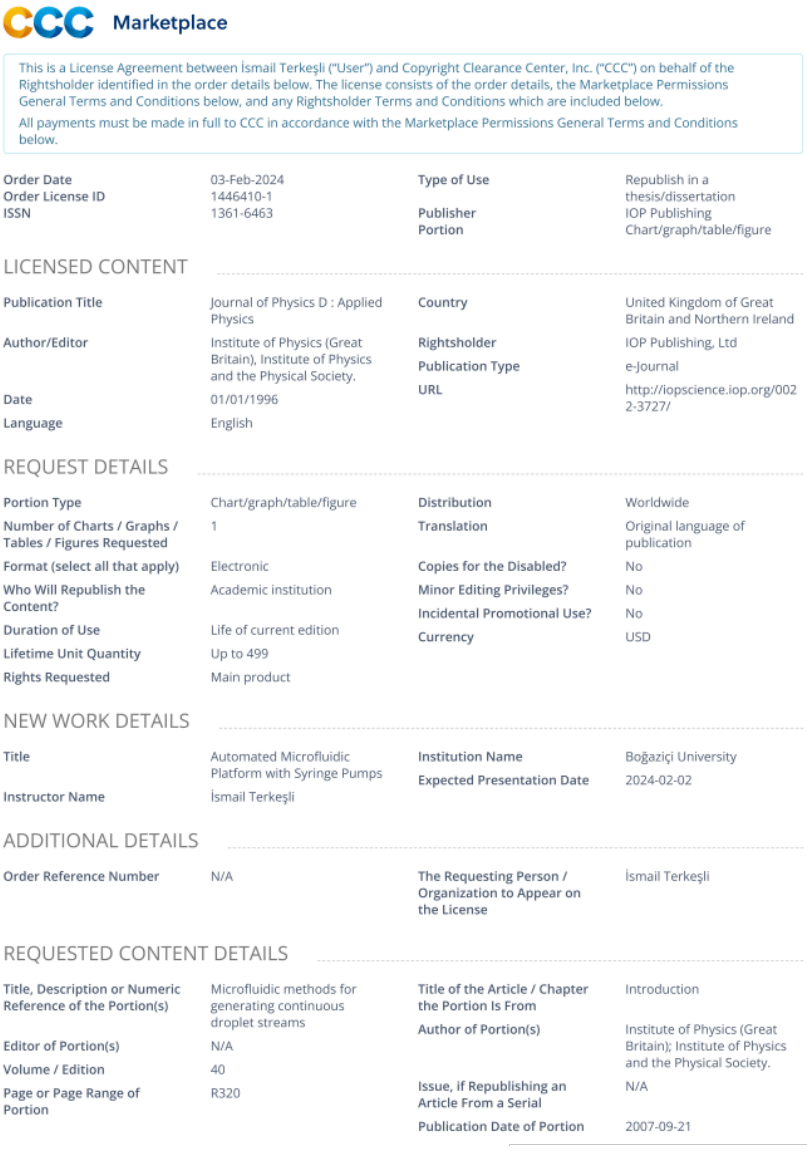

CCC Marketplace

This is a License Agreement between İsmail Terkeşli ("User") and Copyright Clearance Center, Inc. ("CCC") on behalf of the Rightsholder identified in the order details below. The license consists of the order details, the Marketplace Permissions General Terms and Conditions below, and any Rightsholder Terms and Conditions which are included below.

All payments must be made in full to CCC in accordance with the Marketplace Permissions General Terms and Conditions below.

Order Date	03-Feb-2024	Type of Use	Republish in a thesis/dissertation
Order License ID	1446410-1		
ISSN	1361-6463	Publisher	IOP Publishing
		Portion	Chart/graph/table/figure

LICENSED CONTENT

Publication Title	Journal of Physics D : Applied Physics	Country	United Kingdom of Great Britain and Northern Ireland
Author/Editor	Institute of Physics (Great Britain), Institute of Physics and the Physical Society.	Rightsholder	IOP Publishing, Ltd
		Publication Type	e-Journal
Date	01/01/1996	URL	http://iopscience.iop.org/0022-3727/
Language	English		

REQUEST DETAILS

Portion Type	Chart/graph/table/figure	Distribution	Worldwide
Number of Charts / Graphs / Tables / Figures Requested	1	Translation	Original language of publication
Format (select all that apply)	Electronic	Copies for the Disabled?	No
Who Will Republish the Content?	Academic institution	Minor Editing Privileges?	No
		Incidental Promotional Use?	No
Duration of Use	Life of current edition	Currency	USD
Lifetime Unit Quantity	Up to 499		
Rights Requested	Main product		

NEW WORK DETAILS

Title	Automated Microfluidic Platform with Syringe Pumps	Institution Name	Boğaziçi University
		Expected Presentation Date	2024-02-02
Instructor Name	İsmail Terkeşli		

ADDITIONAL DETAILS

Order Reference Number	N/A	The Requesting Person / Organization to Appear on the License	İsmail Terkeşli

REQUESTED CONTENT DETAILS

Title, Description or Numeric Reference of the Portion(s)	Microfluidic methods for generating continuous droplet streams	Title of the Article / Chapter the Portion Is From	Introduction
		Author of Portion(s)	Institute of Physics (Great Britain); Institute of Physics and the Physical Society.
Editor of Portion(s)	N/A		
Volume / Edition	40	Issue, if Republishing an Article From a Serial	N/A
Page or Page Range of Portion	R320	Publication Date of Portion	2007-09-21

Figure A.3. Permission letter [89].